

Storage and propagation of Rydberg polaritons in a cold atomic medium

Dissertation

Von der Fakultät Mathematik und Physik der Universität Stuttgart
zur Erlangung der Würde eines Doktors der Naturwissenschaften
(Dr. rer. nat) genehmigte Abhandlung

vorgelegt von

Ivan Mirgorodskiy
aus Dubna, Russland

Hauptberichter: Prof. Dr. Sebastian Hofferberth
Mitberichter: Prof. Dr. Peter Michler
Prüfungsvorsitzender: Prof. Dr. Hans Peter Büchler

Tag der mündlichen Prüfung: 06.10.2017

Universität Stuttgart
5. Physikalisches Institut
2017

Declaration of Authorship

I, Ivan Mirgorodskiy, declare that this thesis titled, “Storage and propagation of Rydberg polaritons in a cold atomic medium” and the work presented in it are my own. I confirm that:

- This work was done wholly or mainly while in candidature for a research degree at this University.
- Where any part of this thesis has previously been submitted for a degree or any other qualification at this University or any other institution, this has been clearly stated.
- Where I have consulted the published work of others, this is always clearly attributed.
- Where I have quoted from the work of others, the source is always given. With the exception of such quotations, this thesis is entirely my own work.
- I have acknowledged all main sources of help.
- Where the thesis is based on work done by myself jointly with others, I have made clear exactly what was done by others and what I have contributed myself.

Signed:

Date:

“The mind perishes where there is no change or there is no need for a change.”

Vitaly Sundakov

Abstract

Storage and propagation of Rydberg polaritons in a cold atomic medium

by Ivan Mirgorodskiy

Rapid development in the information technologies brings to life new research ideas that can significantly push the progress forward. Rydberg quantum optics is a young field which has great advantages for applications in quantum information processing, but also it is an unbelievable tool for understanding of the nature. A lot of open questions and interesting directions exist here, and the aim of this work is to gain a bit more understanding of the Rydberg physics.

This thesis reports the work on the Rydberg polariton physics in two different regimes. In the first experiment we study the impact of Rydberg molecule formation on the storage and retrieval of Rydberg polaritons in an ultracold atomic medium. We observe coherent revivals appearing in the storage and retrieval efficiency of stored photons that originate from simultaneous excitation of Rydberg atoms and Rydberg molecules in the system with subsequent interference between the possible storage paths. We show that over a large range of principal quantum numbers the observed results can be described by a two-state model including only the atomic Rydberg state and the Rydberg dimer molecule state. At higher principal quantum numbers the influence of polyatomic molecules becomes relevant and the dynamics of the system undergoes a transition from coherent evolution of a few-state system to an effective dephasing into a continuum of molecular states.

In the second part of the work we investigate quantum many-body dynamics of photons propagating under condition of electromagnetically induced transparency through dissipative Rydberg medium at large input photon rates. In a joint experimental and theoretical analysis, this regime allows us to observe the possible signatures of a photon crystal in our data. In addition, we discover and investigate the Rydberg pollution effect, which manifests itself in the anomalously high number of detected Rydberg atoms in our experiment that exhibit a nonlinear growth with the input photon rate. We test and discuss probable origin mechanisms underlying appearance of pollutant Rydberg atoms. This effect is important for the future development of Rydberg quantum optics because it might put additional limitations on many relevant experiments.

Publications

The following publications were written in the course of this thesis:

- C.R. Murray, I. Mirgorodskiy, C. Tresp, A.V. Gorshkov, S. Hofferberth, and T. Pohl
Photon subtraction via induced many-body decoherence; in progress
- I. Mirgorodskiy, F. Christaller, C. Braun, A. Paris-Mandoki, C. Tresp, and S. Hofferberth
Electromagnetically induced transparency of ultra-long-range Rydberg molecules; Phys. Rev. A **96**, 011402(R)
- A. Paris-Mandoki, C. Braun, J. Kumlin, C. Tresp, I. Mirgorodskiy, F. Christaller, H.P. Büchler, and S. Hofferberth
Free-Space Quantum Electrodynamics with a single Rydberg superatom; submitted to Phys. Rev. X
- C. Tresp, C. Zimmer, I. Mirgorodskiy, H. Gorniaczyk, A. Paris-Mandoki, and S. Hofferberth
Single-Photon Absorber Based on Strongly Interacting Rydberg Atoms; Phys. Rev. Lett. **117**, 223001 (2016)
- A. Paris-Mandoki, H. Gorniaczyk, C. Tresp, I. Mirgorodskiy, and S. Hofferberth
Tailoring Rydberg interactions via Förster resonances: state combinations, hopping and angular dependence; J. Phys. B: At. Mol. Opt. Phys. **49** 164001 (2016)
- H. Gorniaczyk, C. Tresp, P. Bienias, A. Paris-Mandoki, W. Li, I. Mirgorodskiy, H. P. Büchler, I. Lesanovsky, and S. Hofferberth
Enhancement of Rydberg-mediated single-photon nonlinearities by electrically tuned Förster resonances; Nature Communications **7**, 12480 (2016)
- C. Tresp, P. Bienias, S. Weber, H. Gorniaczyk, I. Mirgorodskiy, H. P. Büchler, and S. Hofferberth
Dipolar dephasing of Rydberg D-state polaritons; Phys. Rev. Lett, **115**, 083602 (2015)

Acknowledgements

I would like to thank the people without whom this thesis would not have been possible.

First of all, it is my supervisor Prof. Dr. Sebastian Hofferberth who provided me an opportunity to work in his excellent research team. I really appreciate his responsiveness to answer any scientific question or help with any experimental technique. He has cultivated really stimulating working environment where everyone knew that his work is of high value. I wish him everything good in his scientific career!

I am deeply grateful to Prof. Dr. Tilman Pfau for the unbelievable atmosphere of kindness and intelligence in his institute, I was lucky to be a part of. And also for all organized group excursions, sport events and Christmas parties.

I have enjoyed a lot working with the classical RQO team. The easy-going attitude to life of Hannes Gorniaczyk had a strong influence on me and taught me to stress less and enjoy more. Dedication and hard work of Christoph Tresp was a non-stop source of motivation to become better. I do not wish for better colleagues in the beginning of my way.

Our post-doc Asaf Paris-Mandoki has a special place in my way. As founders of our international group, we have shared million lunches together and had even more philosophical discussions meanwhile. His out of the box thinking forced me to reconsider a lot of life concepts. Due to his kindness and permanent desire to help in combination with deep understanding of physics, I had a great opportunity to learn, which I hope I could fully realize. Thank you Asaf for everything and I hope you become a big professor soon!

I am thankful to my other colleagues - our master students: Christian Zimmer for our nice discussion on difference between nuts and seeds, Christoph Braun for his unbelievable enthusiasm for everything and Florian Christaller for his healthy perfectionism; and all of them together for their contribution to the experiment. I would like to specially mention bachelor student Marian Rockenhäuser, who was a great student, and who has introduced me to the magical world of climbing!

I am grateful to all the members of our international group, who made my life in the institute much more rich. Dr. Yi-Hsin Chen and Dr. Yanli Zhou gave me a great insight into Taiwanese and Chinese culture and asian food. My friend Miaoqing Chen was an excellent contender in our table tennis sessions and a perfect companion during our eternal conversations about life. Woojin Kwon always had a great married life advice. Thank you guys for all the time spent together!

Another special gratitude goes to Karin Otter, with whom I shared lots of talks about everything from arts to hiking long distance trails. Also her help in passing through all the German bureaucracy is priceless. I hope that one day someone dances his/her PhD thesis for Karin!

I would like to thank our office workers Astrid Buck, Anne-Katrin Kriesch and Britta Lenz for their excellent work. And I thank all the members of the institute for their support.

Our experimental work have been strongly supported by the unique theoretical expertise of Dr. Przemek Bienias, Dr. James Douglas, Dr. Michael

Gullans, Dr. Emil Zeuthen, Prof. Dr. Alexey Gorshkov and Prof. Dr. Darrik Chang; Callum R. Murray and Prof. Dr. Thomas Pohl. Their analytical understanding of our experiments is invaluable.

Finally, I want to say my special thanks to my family and friends. My parents and my grandparents, my uncle and my aunt always support and encourage me. My brother Max and best friend Boris help me to keep a positive view on life and sharp thinking. Above all, I would like to thank my beloved wife Mona-Marie for her infinite love and kindness. She is an inexhaustible source of inspiration for me and I have to admit that without her I would have never come to Germany.

Contents

Declaration of Authorship	iii
Abstract	vii
Acknowledgements	xi
0 Zusammenfassung	1
1 Introduction	7
2 Theoretical background	13
2.1 Rydberg atoms	13
2.1.1 General Properties	13
2.1.2 Rydberg Electron Wave Function	14
2.1.3 Rydberg Atoms in Electric Field	16
2.1.4 Interaction of Rydberg Atoms	18
2.2 Interaction of Light with Atomic Medium	21
2.2.1 Electromagnetically Induced Transparency	22
2.2.2 Slow light	25
2.2.3 Dark-state polaritons	27
2.2.4 Storage of light	28
2.2.5 Rydberg blockade on EIT	30
2.3 Ultralong-range Rydberg molecules	31
3 Experimental Setup	35
3.1 Preparation of ultracold atomic sample	35
3.1.1 Magneto-optical trap	35
3.1.2 Trapping into an optical dipole trap	37
3.1.3 Raman sideband cooling	38
3.1.4 Optical pumping	40
3.1.5 Electric field control	42
3.2 The laser system for EIT experiments	44
3.3 Single Photon Imaging with EMCCD Camera	46
3.3.1 Motivation for a single photon imaging with Rydberg atoms	46
3.3.2 EMCCD camera Andor iXon Ultra 897	48
3.3.3 A brief theory of an EMCCD operation	51
3.3.4 Single photon imaging	55
3.3.5 Outlook	58

4	Electromagnetically induced transparency of ultralong-range Rydberg molecules	61
4.1	Introduction	61
4.2	Experimental scheme	62
4.3	Observation of coherent revival in storage and retrieval efficiency	63
4.4	The model of two species EIT	65
4.5	Discussion	66
4.6	Density dependence of the observed coherent revival	68
4.7	Transition from coherent dynamics to an effective dephasing . .	68
4.8	Conclusion	70
5	Photon propagation and pollution in a dissipative Rydberg medium at large input rates	73
5.1	Introduction	73
5.2	Experimental realization	75
5.3	Results and discussion	76
5.4	Comparison with the theory	80
5.5	State selective ionization	83
5.6	A hypothesis on Rydberg pollution	86
5.7	An experimental test of the hypothesis on Rydberg pollutants formation	93
5.8	Outlook and conclusion	93
6	The final notes	97
	General outlook for the discussed work	97
	Photon subtraction via induced many-body decoherence	98
A	Dephasing of a spin wave induced by atomic random motion	101
	Bibliography	103

Dedicated to my grandfather.

Chapter 0

Zusammenfassung

Es ist heutzutage sehr gut bekannt, dass Photonen, die fundamentalen Quanten des Lichts, im Vakuum extrem schwach miteinander interagieren. Seit dem 19. Jahrhundert haben Physiker wie Faraday und Kerr entdeckt, dass die Eigenschaften des Lichts, bei der Propagation durch ein Medium manipuliert werden können. Während der Laserrevolution im 20. Jahrhundert wurde erkannt, dass die optischen Eigenschaften eines Mediums durch ein angelegtes elektrisches Feld kontrolliert werden können. Dies führte zur Entwicklung eines neuen Feldes der Physik, der nichtlinearen Optik. Hierbei werden konventionelle nichtlineare Medien verwendet, um mit deren Hilfe eine Wechselwirkung zwischen Photonen zu realisieren. Die Nichtlinearität in jenen Medien erweist sich jedoch als enorm schwach und erst bei sehr hohen optischen Intensitäten sind signifikante Effekte zu erzielen [1].

Die schnelle Entwicklung von Technologien im 20. Jahrhundert brachte Physiker auf die Idee, dass Photonen, Arbeitstiere in der Massenelektronik, aufgrund ihrer einzigartigen Eigenschaften potenziell großartige Kandidaten sind, um Elektronen zu ersetzen. Die intrinsisch hohe Ausbreitungsgeschwindigkeit des Lichts und die Möglichkeit, Wellenpakete mit Femtosekundenlänge zu formen, können die Geschwindigkeit der Datenverarbeitung und die Informationstransportraten erhöhen.

Darüber hinaus brachten die Träume über die Quantenberechnung, welche die Quantenlogik ausnutzt, um rechnerische Aufgaben effizienter zu machen, Wissenschaftler dazu ein Photon auf Grund seiner schwachen Wechselwirkungen mit der Umwelt und mit sich selbst als idealen Kandidaten zu Verwendung als Qubit [2], einem Träger von Quanteninformationen, in Erwägung zu ziehen. Daher wurden Photonen verwendet, um Verschränkung zu demonstrieren [3, 4] und es wurde festgestellt, dass sie die meisten Kriterien für die Quantenberechnung erfüllen [5]. Die Realisierung von zwei Qubits Quantengattern, der Schlüsselkomponente für die Quantenberechnung, erfordert jedoch eine stark kontrollierbare Interaktion zwischen einzelnen Qubits und die Möglichkeit, sie in einer robusten Weise zu initialisieren und schließlich auszulesen. Die Manipulation und Detektion von Photonen auf dem Level einzelner Photonen ist bereits gut etabliert, auf der anderen Seite aber sind die Erzeugung einzelner Photonen auf Knopfdruck [6, 7, 8] sowie die Interaktion auf einzel Photonlevel [9, 10] langjährige Ziele der Quantenoptikforschung. Um die Wechselwirkung zwischen einem Paar von Photonen zu vermitteln ist das extremste nichtlineare Medium erforderlich, dieses muss auf die Propagation von zwei Photonen

gänzlich anders reagiert als wenn ein einzelnes Photon im Medium propagiert. Dieses Regime wird nichtlineare Quantenoptik genannt [11].

Das einfachste System, welches in das Regime der nichtlinearen Quantenoptik vorstößt, ist die Wechselwirkung eines einzelnen Photons mit einem einzigen Atom. Der Mechanismus erfolgt in zwei Schritten: Ein Photon muss mit dem Atom interagieren, um den Zustand des Atoms zu ändern; und der neue Zustand des Atoms muss alle anderen Photonen beeinflussen. Leider ist die Atom-Photon-Wechselwirkungswahrscheinlichkeit auf Resonanz winzig, daher ist es nicht möglich, eine derart starke Nichtlinearität im freien Raum zu realisieren.

Es ist ein logischer Schritt, ein Photon zu zwingen, das Atom wiederholt zu durchlaufen, was die Wahrscheinlichkeit der Atom-Photon-Wechselwirkung signifikant erhöhen kann. Dies kann erreicht werden, indem man ein Atom in einen optischen Resonator platziert [12, 13, 14, 15] und dieses Forschungsgebiet beschäftigt sich mit der Resonator Quantenelektrodynamik (cQED). Die Verstärkung der Wechselwirkungswahrscheinlichkeit wird durch die Finesse des Resonators F eingestellt, die im wesentlichen die Anzahl der Umrundungen definiert, die das Photon innerhalb des Resonators bildet bevor es diesen verlässt. Der cQED-Ansatz wurde um die Verwendung einzelner Atome dahingehend erweitert, dass auch künstliche Atome, wie z. B. Halbleiter-Quantenpunkten [16, 17] oder Stickstoff-Fehlstellen-Zentren in Diamanten [18, 19], untersucht werden können. Die Möglichkeit, ein starkes Kopplungsregime zwischen einem Atom und einem optischen Resonator aufzubauen, führte zur Implementierung eines nichtzerstörenden Photonendetektors [20], eines Quantenphasenschalters zwischen einem einzelnen Atom und einem einzelnen Photon [21] und einem Quantengatter zwischen einem Atom und einem Photon [22, 23].

Ein alternativer Ansatz um in das Regime der nichtlinearen Quantenoptik einzutreten, ist die Erzeugung des Drei-Zustands-Systems mittels eines schwachen Probefeldes, das das anfängliche Zwei-Zustands-System antreibt und eine starke Kontrollfeldkopplung an einen dritten metastabilen Zustand. Dies ändert ein Medium durch die elektromagnetisch induzierte Transparenz (EIT) dahingehend, dass es in einem engen Spektralbereich transparent ist, andernfalls jedoch sämtliches Licht absorbiert. Diesen Resonanzbedingungen breitet sich der schwache Lichtpuls durch das Medium in Form einer gekoppelten Anregung, als Polariton, aus. Dieses breitet sich im Medium mit einer drastisch reduzierten Gruppengeschwindigkeit aus, die es ermöglicht, es sehr effizient zu manipulieren [24, 25]. Die Kopplung des metastabilen dritten Niveaus des Systems auf das zusätzliche vierte Niveau mit einem weiteren resonanten Licht ermöglicht es, die EIT-Kondition ein- und auszuschalten, was die Übertragung der Photonen kontrolliert. Dies führt zu einer starken nichtlinearen Antwort, die es ermöglicht, einen optischen Transistor zu implementieren, der nur durch ein gespeichertes Photon gesteuert wird [26].

Der nächste vielversprechende Ansatz nutzt eine starke langreichweitige Dipol-Dipol-Wechselwirkung zwischen Rydberg Zuständen. Wenn ein Rydberg Zustand als metastabiler Zustand im EIT-Schema verwendet wird, wird die Wechselwirkung zwischen verschiedenen Rydberg Atomen auf die Photonen abgebildet. Die einfachste Realisierung ist die resonante Rydberg-EIT,

wenn die starke Wechselwirkung zwischen Rydberg Atomen den Zwei-Photonen-Übergang aus Resonanz bringen, führt dies zur Zerstörung der Transparenzbedingung und der Streuung von zwei oder mehr Photonen [27]. Dieser Mechanismus wird Rydberg Blockade genannt und manifestiert sich in der Existenz eines Volumens um ein Rydberg Atom, in welchem die Resonanz der EIT unterdrückt wird. Innerhalb dieses Volumens ist die Anregung eines zweiten Rydbergatoms nicht möglich. Daher wirken Atome innerhalb der Blockadekugel wie zweistufige Absorber, was zu einer starken optischen Nichtlinearität auf der Einzelphotonenebene führt.

Die erste experimentelle Realisierung der nichtlinearen Quantenoptik mit einem Rydberg-EIT Medium erfolgte durch die bahnbrechende Arbeit der Arbeitsgruppe um Charles Adams [28], in welcher die Autoren ein dissipatives nichtlineares optisches Medium kreierten, das nur ein Photon überträgt, aber zwei Photonen streut. Nach diesem wichtigen Ergebnis fingen viele Gruppen an, für die Quanteninformationsverarbeitung die Rydberg Blockade einzusetzen. Die Realisierung effizienter Einzelphotonenquellen [29, 30], Schaffung von Verschränkung zwischen Licht- und angeregten Atomen [31], die Demonstration von Einzelphotonen-Alloptikschaltern [32] und Transistoren [33, 34, 35], Einzelphotonenabsorber [36] und interaktionsinduzierte Photonenphasenverschiebungen [37, 38, 39] sind hervorragende Beispiele für die Möglichkeiten, die die Rydberg-Quantenoptik bringt. Das Arbeiten in einem Regime mit dispersiven Nichtlinearitäten, indem der Brechungsindex von dem Abstand zwischen den Photonen abhängt, erlaubt einen gebundenen Zustand von zwei Photonen zu erreichen [40].

Photon-Photon-Wechselwirkungen, die durch Rydberg Atome induziert werden, eröffnen auch die Möglichkeit, die Vielteilchenphysik von stark interagierenden Photonen zu erforschen. So wurden photonische Zustände, die sowohl kristallklare Korrelationen sowohl im dispersiven Regime [41, 42] als auch im dissipativen Regime [43, 44] oder der Dreikörper-Wechselwirkung zwischen Photonen [45, 46] zeigten, vorhergesagt. Ein Weg, um das Regime des Vielteilchensystems von stark interagierenden Polaritonen zu betreten, besteht darin, das System so vorzubereiten, dass es viele Polaritonen unterstützen kann. Technisch kann dies durch die Erweiterung der Polaritonausbreitung auf die dreidimensionale Geometrie erreicht werden.

Diese Doktorarbeit

Die wissenschaftliche Geschichte unserer Gruppe beginnt im Jahr 2014, als die erste Version des Apparates, der die Realisierung einer riesigen optischen Nichtlinearität mit Rydberg Atomen ermöglichte, beendet war. Die erste große Arbeit, die erfolgreich auf der neuen Maschine durchgeführt wurde, wurde zur Implementierung eines einzelnen Photonentransistors [33]. Die Idee des Experiments ist, dass die Übertragung von Source-Photonen durch ein Medium von ultra-kalten Rubidium Atomen nur durch ein einziges Gate Photon aufgrund des Mechanismus der Rydberg-Blockade gesteuert werden kann. Die Demonstration eines Einzelphotonentransistors wurde auf dem Gebiet der Quanteninformationsverarbeitung mit Rydberg Atomen ein großer Erfolg. Eine weitere

starke Errungenschaft war die Untersuchung des Dephasierungsmechanismus der Rydberg D-State Polaritonen in die stationären Rydberg Atome, die aus der Zustandsmischungswechselwirkung entstanden sind, welche für den Rydberg D-Zustand intrinsischen sind [47]. Die Möglichkeit, die Winkelabhängigkeit von Rydberg Wechselwirkungen als Einstellknopf in Rydberg Experimenten zu nutzen, macht diese Arbeit zu einer von hoher Relevanz für den Bereich der Rydberg Physik [48, 49].

Obwohl sie im Besitzes einer großartigen Maschine waren, brachte der Wunsch, die experimentellen Möglichkeiten auf die nächste Stufe zu bringen, die Gruppe dazu über die Verbesserungsmöglichkeiten der bestehenden Version des Apparates nachzudenken. Dies führte dazu, dass ein paar neue Konzepte, welche die Leistung erheblich steigern konnten, entstanden. So wurde im Rahmen dieser Arbeit die erste Version des Versuchsapparates aktualisiert. Der erste Schritt in dieser Arbeit war, die Vakuumkammer zu öffnen und den bereits hergestellten elektrischen Feldregler in das System zu integrieren. Die Kontrolle über das elektrische Feld ist eine große Verbesserung, weil sie erlaubt, elektrische Streufelder in der Kammer zu kompensieren und somit die Driften von Atomlinien zu stabilisieren. Auf der anderen Seite wurde es ein mächtiges Werkzeug für die Einstellung von Rydberg Zuständen in starke Förster-Resonanzen, welche die Leistung eines einzelnen Photonentransistors drastisch erhöht haben [35]. Der Austausch der alten Glaszelle aus Pyrex durch eine neue Glaszelle aus Quarz wurde eine zweite Verbesserung. Dies ermöglichte es, die allgemeine elektrische Streufeldstabilität zu verbessern und einen starken Selbstfokussierungseffekt zu verhindern, der unter hoher Intensität unseres Dipolfallenstrahls in einem Pyrex Glas auftritt. Um die allgemeine Stabilität zu verstärken, haben wir verbesserte optische und elektronische Systeme. Eine weitere große Verbesserung war die Einführung zusätzlicher Kühlstufen, nämlich die Raman-Seitenbandkühlung. Es erlaubte eine Atomwolke zu niedrigeren Temperaturen ohne Reduktion der Atomdichte zu kühlen, wie es bei der Verdampfungskühlung geschieht, was hilft, den Betrieb mit einer höheren optischen Tiefe aufrechtzuerhalten. Dies wurde ein entscheidender Faktor für die in dieser Dissertation dargestellten Experimente.

Eine beträchtliche Zeitspanne innerhalb des Zeitraums in dem diese Doktorarbeit entstand wurde mit der Untersuchung einer möglichen Anwendung einer EMCCD-Kamera für eine Einzelphoton Bildgebung verbracht. Die Motivation für diese Aufgabe wurde durch das Interesse am Eintreten in das Feld der Vielteilchenphysik mit stark wechselwirkenden Photonen vorangetrieben. Hier bietet eine EMCCD Kamera mehrere Möglichkeiten. Die erste Möglichkeit ist einen Einfluss der Polariton Wechselwirkung auf eine transversale Mode der propagierende Polaritonen zu untersuchen, die sich zum Beispiel bei der Bildung von räumlichen Solitonen manifestieren könnten [50]. Eine weitere Möglichkeit besteht darin, jedes Pixel in einer EMCCD Kamera als einzigartigen Einzelphotonenzähler zu verwenden. Ein solcher Ansatz könnte es ermöglichen, alle Ordnungen von Photonenkorrelationen im Vielteilchensystem von Photonen zu messen. Daher wurde als Testlauf ein Photon nach dem anderen Photon als Bildaufzeichnung eines Gaußschen Strahls gezeigt. Dies erschafft schöne Perspektiven für die zukünftigen Experimente auf dem Gebiet der Rydberg

Quantenoptik.

Im Hauptteil dieser Doktorarbeit haben wir die Polaritonenphysik in zwei verschiedenen Regimen untersucht. Das erste Experiment realisiert ein klassisches EIT Schema mit einem Rydberg Medium, in dem sich Licht durch das Medium in Form von Rydberg Polaritonen propagiert [51]. In diesem Schema ist es möglich, das Licht im Inneren des Mediums vollständig zu stoppen, indem die elektromagnetische Komponente des Polaritons vollständig auf die Atomkomponente übertragen wird [30]. In unserer Arbeit untersuchen wir die Speicherung und die Rückgewinnung von Rydberg Polaritonen unter der Bedingung der Rydberg Molekülbildung [52], die bei der Atomdichte um 10^{12} cm^{-3} beginnt. Dieses Regime ist insbesondere interessant, weil die Bildung von Rydberg Molekülen als begrenzender Faktor für die Kohärenz von langsamen und gespeicherten Rydberg Polaritonen angesehen wurde. Aus der Position der Rydberg Quantenoptik ergibt sich, dass kohärente Photonengattern auf der Basis von Rydberg vermittelten Photon-Photon-Wechselwirkung bei höheren Dichten betrieben werden können, was ihre Genauigkeit im Vergleich zu aktuellen Realisierungen erhöht [53, 54].

Das zweite Experiment tritt in das Regime vieler wechselwirkender Photonen ein. Unser Ziel ist es, einen hochkorrelierten Lichtzustand, nämlich Photonenkristall, in einem dissipativen Rydberg-EIT Medium zu erzeugen [43, 44]. Basierend auf den theoretischen Vorschlägen ist es notwendig, eine eindimensionale Ausbreitungsbedingung für Polaritonen aufrechtzuerhalten und gleichzeitig die optische Tiefe (OD) pro Blockade so hoch wie möglich zu halten. In diesem Fall sollte das Pumpen des Atommediums bei hohen Eingangsphtonenraten zu einer Bildung der Polaritonfolge im Inneren des Mediums und demzufolge einer Photonenfolge auf dem Output des Mediums führen. Versuchen wir, diese Bedingungen zu erfüllen, erhalten wir Merkmale, welche die Bildung eines Photonenkristalls anzeigen. Zusätzlich zeigen wir einen unbekannt Mechanismus, den wir Rydberg Verschmutzung nennen, der durch die anomal hohen Anzahl von detektierten Rydberg-Atomen in unserem Experiment auftritt, die ein nichtlineares Wachstum mit der eingegebenen Photonenrate aufweist. Dieser Effekt kann die vielen relevanten Experimente auf dem Gebiet der Rydberg Quantenoptik zusätzlich einschränken.

Chapter 1

Introduction

Nowadays, it is well known that photons, the fundamental quanta of light, interact extremely weakly with each other in vacuum. Since the XIX century physicists like Faraday and Kerr discovered that the properties of light can be manipulated during propagation through the medium. Throughout the laser revolution in the XX century it was realized that the optical properties of the medium can be controlled by applied electrical field. This resulted in development of a new field of physics, called nonlinear optics, where conventional nonlinear media were used to make photons interact. Unfortunately, the conventional type of nonlinearities is tremendously weak and it is necessary to apply high optical intensities to achieve a significant effect [1].

Fast development of technologies in the XX century brought physicists to the fact that photons are potentially great candidates to become a replacement of electrons, workhorses in moder electronics, due to their unique properties. Intrinsically high traveling speed of light and the possibility to shape wave packets with femtosecond length can boost the speed of data processing and the information transfer rates.

Even more, the dreams about quantum computation, which exploits quantum logic to perform computational tasks more efficient, made scientists consider a photon as an ideal candidate to be used as a qubit [2], a carrier of quantum information, due to photons weak interactions with environment and each other. Thus, photons were used to demonstrate entanglement [3, 4], and were found to satisfy most of criteria for quantum computation [5]. However, realization of two qubits quantum gates, the key component for quantum computation, requires strong controllable interaction between individual qubits, and the possibility to initialize and read them out in a robust manner. As for photons, the techniques to detect and manipulate the light on a single photon level are well established. But on the other hand, generation of single photons [6, 7, 8] and interaction on a single photon level [9, 10] have been long standing goals in quantum-optics research. To mediate the interaction between a pair of photons, the extremely nonlinear medium is required, which would respond to propagation of two photons substantially different than that for one photon. This regime is called quantum nonlinear optics [11].

The simplest system realizing the regime of quantum nonlinear optics is an interaction of a single photon with a single atom. The mechanism would follow two steps: the photon has to interact with the atom to change the state of the atom; and the new state of the atom has to affect all other photons. Unfortunately, the atom-photon interaction probability on resonance is much

smaller than unity, what does not allow to realize strong nonlinearity in free space.

A logical step to make is to force a photon to pass through an atom repeatedly, which can significantly enhance the probability of atom-photon interaction. This can be achieved by placing an atom into an optical cavity [12, 13, 14, 15] and is denoted as cavity quantum electrodynamics (cQED). The enhancement of interaction probability is set by the finesse of the cavity F , which, essentially, defines the number of round-trips the photon makes inside of the cavity before it leaves. The cQED approach was extended from using real atoms to artificial atoms, such as semiconductor quantum dots [16, 17] or nitrogen–vacancy centers in diamond [18, 19]. The possibility to establish a strong coupling regime between an atom and an optical resonator led to implementation of a non-destructive photon detector [20], a quantum phase switch between a single atom and a single photon [21], and a quantum gate between an atom and a photon [22, 23].

An alternative approach to enter the regime of quantum nonlinear optics is exciting a three-level system by means of a weak probe field driving the initial two level system and a strong control field coupling to a third metastable state. Due to the effect known as electromagnetically induced transparency (EIT), a medium changes from opaque to transparent in a narrow spectral window. Under the resonant condition, the probe light pulse propagates through the medium in the form of polariton with dramatically reduced group velocity which allows to manipulate it very efficiently [24, 25]. Coupling the metastable third level of the system to the additional fourth level with a resonant light allows to switch the EIT condition on and off, such controlling the transmission of photons. This results in a strong nonlinear response, which allowed to implement an optical transistor gated by just one stored photon [26].

The next very promising approach exploits strong long-range dipole-dipole interaction between Rydberg states. If a Rydberg state is used as a metastable state in the EIT scheme, the interaction between different Rydberg atoms is mapped onto the photons. The simplest realization is resonant Rydberg EIT when the strong interaction between Rydberg atoms tunes the two-photon transition out of resonance, which leads to the destruction of transparency condition and scattering of two or more photons [27]. Such a mechanism reveals the effect called Rydberg blockade, which manifests itself in the existence of a volume around a Rydberg atom where EIT condition is suppressed (excitation of two Rydberg atoms is not possible). Therefore, atoms within the blockade sphere act like two-level absorbers, resulting in a strong optical nonlinearity at the single-photon level.

The first experimental realization of quantum nonlinear optics with Rydberg EIT medium was done by groundbreaking work of Charles Adams group [28], where the authors created a dissipative nonlinear optical medium that transmits only one photon, but scatters two photons. After this important result many groups caught up on applying Rydberg blockade to the field of quantum information processing. Realization of efficient single photon sources [29, 30], creation of entanglement between light and atomic excitations [31], demonstration of single-photon all-optical switches [32] and transistors [33, 34, 35],

single-photon absorbers [36] and interaction induced photon phase shifts [37, 38, 39] are the excellent examples of the opportunities that Rydberg quantum optics brings. Entering a regime of dispersive nonlinearity, where the refraction index depends on the distance between photons, allowed to achieve a bound state of two-photons [40].

Photon-photon interaction induced by Rydberg atoms also opens a possibility to explore many-body physics of strongly interacting photons. Thus, photonic states exhibiting crystal correlations both in dispersive regime [41, 42] and dissipative regime [43, 44], or three-body interaction between photons [45, 46] were predicted. One way to enter the regime of many-body system of strongly interacting photons is to prepare a system that can support many polaritons. Technically it can be achieved by expanding the polariton propagation to three-dimensional geometry.

This Thesis

The scientific story of our group starts in 2014 when the first version of the apparatus that allowed realization of giant optical nonlinearities with Rydberg atoms was finished. The first big work that was successfully performed on the new machine became an implementation of a single photon transistor [33]. The idea of the experiment is that the transmission of source photons through a medium of ultra-cold Rubidium atoms could be controlled just by a single gate photon due to the mechanism of Rydberg blockade. Demonstration of a single photon transistor became a big achievement in the field of quantum information processing with Rydberg atoms. Another strong achievement was investigation of the dephasing mechanism of Rydberg D-state polaritons into the stationary Rydberg atoms that originates from the state mixing interaction intrinsic for Rydberg D-states [47]. Possibility to use angular dependence of Rydberg interactions as a tuning knob in Rydberg experiments makes this work of high relevance for the field of Rydberg physics [48, 49].

Despite possessing a great machine, the desire to bring experimental possibilities onto the next level inspired the group to think about improving the existing version of the apparatus. It resulted into designing a few new concepts that could significantly boost the performance. Thus, in the framework of this thesis the first version of the experimental apparatus was updated. The first step in this work was to open the vacuum chamber and integrate the already manufactured electric field controller into the system. Control over the electric field is a great enhancement, because it allows to compensate stray electric fields in the chamber and, thus, stabilize the drifts of atomic lines. On the other hand, it became a powerful tool for tuning Rydberg states into strong Förster resonances, which drastically increased performance of a single photon transistor [35]. Exchange of the old glass cell, made from pyrex, by a new glass cell made of quartz became a second improvement. This allowed to improve general stray electric field stability and inhibit strong self-focusing effect appearing under high intensity of our dipole trap beam in a pyrex glass. To enhance the general stability we have improved optical schemes and electronic schemes. Another

big improvement was introducing additional cooling step, namely Raman side-band cooling. It allowed to cool an atomic cloud to lower temperatures without atomic density reduction, as it happens during evaporation cooling, what helps to maintain operation with higher optical depth. This became a crucial factor for the experiments represented in this dissertation.

A significant amount of time during the work on this thesis was devoted to investigation of a possible application of an EMCCD camera for a single photon imaging. The motivation for this task was driven by the interest in entering the field of many-body physics with strongly interacting photons. Here an EMCCD camera provides several opportunities. The first one is a possibility to study an impact of polariton interaction on a transverse mode of propagating polaritons, which could manifest itself, for example, in formation of spatial solitons [50]. Another opportunity is to use each pixel in an EMCCD camera as a unique single photon counter. Such an approach could allow to measure all orders of photon correlations in the many-body system of photons. Therefore, as a test run, photon by photon imaging of a Gaussian beam was shown. This creates nice perspectives for the future experiments in the field of Rydberg quantum optics.

In the main part of this thesis we have studied the polariton physics in two different regimes. The first experiment realizes a classical EIT scheme with a Rydberg medium, in which light propagates through the medium in the form of Rydberg polaritons [51]. In this scheme it is possible to completely stop the light inside the medium by fully transferring the electromagnetic component of the polariton to the atomic component [30]. In our work we investigate storage and retrieval of Rydberg polaritons under the condition of Rydberg molecules formation [52], which starts to happen at the atomic density around 10^{12} cm^{-3} . This regime is, in particular, interesting because formation of Rydberg molecules was considered as a limiting factor on the coherence of slow and stored Rydberg polaritons. From the position of Rydberg quantum optics, we find that coherent photonic gates based on Rydberg-mediated photon-photon interaction could be operated at higher densities, boosting their fidelity compared to current realizations [53, 54].

The second experiment enters the regime of many interacting photons. Our aim is to generate a highly correlated state of light, namely photon crystal, in a dissipative Rydberg-EIT medium [43, 44]. Based on the theoretical proposals, it is necessary to maintain a one dimensional propagation condition for polaritons and, at the same time, keep optical depth (OD) per blockade as high as possible. In this case, pumping the atomic medium at high input photon rates should result in formation of a train of polaritons inside the medium and, consequently, a train of photons on the output of the medium. Trying to satisfy these conditions, we obtain features indicating formation of a photon crystal. In addition, we reveal an obscure effect, that we call Rydberg pollution, appearing in the anomalously high number of detected Rydberg atoms in our experiment that exhibit a nonlinear growth with the input photon rate. This effect can put additional restrictions on the many relevant experiments in the field of Rydberg quantum optics.

This thesis is organized as follows: Chapter 2 introduces a theoretical background, containing necessary knowledge on Rydberg atoms, EIT and Rydberg molecules. Chapter 3 describes experimental apparatus and a technique developed for a single photon imaging. The experimental results on EIT of Rydberg molecules are presented in Chapter 4. The work on generation of a photonic crystal and Rydberg pollution is discussed in Chapter 5. Finally, Chapter 6 provides an outlook for the discussed work and describes the basic idea and experimental realization of the photon subtraction via induced many-body decoherence.

Chapter 2

Theoretical background

2.1 Rydberg atoms

Rydberg atoms are the atoms excited to high principal quantum numbers n . The most common choice for Rydberg atoms is alkali atoms, because of the hydrogen like structure that makes it easy to work experimentally with and often simple for calculations. Properties of such atoms are well studied and reviewed in different sources [55, 56, 57]. In this work ^{87}Rb is used as a medium for Rydberg excitations and therefore in this chapter we will highlight some of the most important properties of Rydberg atoms and their interactions typical for Rubidium. We will start with some general overview of Rydberg atoms in Chap. 2.1.1, and then, to get a deeper insight, the calculation of the electron's wavefunction will be presented in Chap 2.1.2. The strong interaction with an external electric field will be discussed in Chap. 2.1.3 and the very important overview of the dipole-dipole interaction of Rydberg atoms is given in Chap. 2.1.4.

2.1.1 General Properties

The properties of a Rubidium atom are very similar to those one of a hydrogen, because Rubidium atom consists of a single valence electron that is revolving around a positively charged core. This core consists of a nucleus and all other electrons that are positioned in closed shells. Thus the discrepancy for a valence electron from a simple $1/r$ Coulomb potential arises from the repulsive interaction of a valence electron and core electrons. This leads to a modification of a binding energy of a Rydberg electron which can be written as [56]

$$E(n, l, j) = -\frac{Ry}{(n - \delta(n, l, j))^2} = -\frac{Ry}{(n^*)^2}, \quad (2.1)$$

where Ry is an element related Rydberg constant, $Ry = R_\infty/(1+m_e/m_{\text{nucleus}}) = 109\,736.605\text{ cm}^{-1}$, and $R_\infty = 109\,737.316\text{ cm}^{-1}$ is a Rydberg constant. The effective principal quantum number n^* strongly depends on l , while dependence on the total angular momentum of the valence electron arises from the fine structure splitting and much weaker. The quantum defect $\delta(n, l, j)$ is described by empirical formula [58, 59]

$$\delta(n, l, j) = \delta_0 + \frac{\delta_2}{(n - \delta_0)^2} + \frac{\delta_4}{(n - \delta_0)^4} + \frac{\delta_6}{(n - \delta_0)^6} \quad (2.2)$$

Property	Scaling	$5S_{1/2}$	$100S_{1/2}$
Binding energy E	$(n^*)^{-2}$	4.18 eV	1.43 meV
Level spacing	$(n^*)^{-3}$	2.5 eV ($5S \leftrightarrow 6S$)	29 μ eV ($99S \leftrightarrow 100S$)
Orbit radius	$(n^*)^2$	$5.63a_0$	$13998a_0$
Polarizability α	$(n^*)^7$	$-79.4 \text{ mHz V}^{-2} \text{ cm}^2$	$-6.2 \text{ GHz V}^{-2} \text{ cm}^2$
Lifetime τ	$(n^*)^3$	26.2 ns ($5P_{3/2} \leftrightarrow 5S_{1/2}$)	336 μ s at 300K
vdW coefficient C_6	$(n^*)^{11}$	4707 au	$5.4 \cdot 10^{21}$ au

TABLE 2.1: Properties of Rydberg atoms for ^{87}Rb . The general scaling with effective principal quantum number n^* can be expressed by power laws. The values for an electron in the 5S ground state and 100S Rydberg state are compared. The data is taken from [63, 64, 65, 55, 56].

but for large principal quantum numbers it is enough to include only δ_0 and δ_2 . For ^{87}Rb quantum defect takes the values of $\delta_0(l=0) = 3.13$, $\delta_0(l=1) = 2.64$, $\delta_0(l=2) = 1.35$, $\delta_0(l=3) = 0.016$, $\delta_0(l > 3) \approx 0$ [59, 60, 61]. And more precise values for nS and nD have been measured in [62]. It is seen that for $l > 3$ the quantum defect is very small and therefore the energies of the states are almost equivalent to ones in hydrogen and are called "hydrogen states".

As it was said before the properties of alkali Rydberg atoms are similar to hydrogen, where most of the properties come from the binding energies. Thus in hydrogen these properties are determined by principal quantum number n and for alkali atoms one has to use an effective principal quantum number n^* in all the scalings [55]. Table 2.1 shows an overview of some important values and their corresponding scaling. The orbital radius of a Rydberg electron, which is defined as $\langle r \rangle = 0.5(3(n^*)^2 - l(l+1))$, is much larger than the one for a ground state atom. The spontaneous lifetime of Rydberg states is defined by a radiative decay to lower lying levels and due to the small spatial overlap between Rydberg wave function and ground state wave function the lifetime is quite long, with the scaling of $(n^*)^3$. For 100S state the spontaneous decay lifetime is 1.3 ms. For Rydberg state with $n \geq 40$ the absorption and stimulated emission of thermally occupied infrared modes to neighboring states start to dominate the lifetime. Therefore the black body radiation at a temperature of $T = 300 \text{ K}$ changes the lifetime of 100S to 336 μ s [65]. Another property, that originates from the large orbital radius and is widely used in the Rydberg experiments for Rydberg atoms detection, is the relatively low ionization threshold which scales with $(n^*)^{-4}$.

2.1.2 Rydberg Electron Wave Function

Further understanding of the properties of Rydberg atoms requires knowledge of a Rydberg atom wave function. The wave function can be calculated by solving Schrödinger's equation for the valence electron, which in atomic units written as [55]

$$\left(-\frac{\nabla^2}{2} + V(r) \right) \psi(r, \theta, \phi) = E\psi(r, \theta, \phi). \quad (2.3)$$

Here we define the distance between the valence electron and the nucleus as r , θ and ϕ are spherical angles, $V(r)$ is the spherically symmetric potential created by the core. The next step is to separate the radial and angular parts of the wave function $\psi(r, \theta, \phi) = R(r)Y(\theta, \phi)$. Firstly, one can obtain an angular part of the wave function that is similar for hydrogen and Rubidium

$$Y_{lm}(\theta, \phi) = \sqrt{\frac{(l-m)! 2l+1}{(l+m)! 4\pi}} P_l^m(\cos \theta) e^{im\phi}, \quad (2.4)$$

where P_l^m is the associated Legendre polynomial, l is an angular momentum and it is zero or a positive integer, m takes integral values from $-l$ to l and is a projection of an angular momentum onto the quantization axis. Next, one can obtain the equation for a radial part of the wave function

$$\left(-\frac{d^2}{dr^2} - \frac{2}{r} \frac{d}{dr} + \frac{l(l+1)}{r^2} + 2V(r) \right) R(r) = 2ER(r) \quad (2.5)$$

where $l(l+1)/r^2$ is twice the centrifugal potential. Now we have to take into account the impact of the core on the Coulomb potential that appears as a stronger attractive potential corresponding to an effective charge $Z_{\text{eff}} > 1$. In addition ionic core can be polarized by the valence electron which leads to additional modification in the potential. Therefore one should use an effective potential in Shrödinger Eq. 2.5 for $V(r)$ [66, 67, 68]

$$V_{\text{eff}}(r) = -\frac{Z_{\text{eff}}(r, l)}{r} - \frac{\alpha_c}{2r^4} \left(1 - e^{-\left(\frac{r}{r_c}\right)^6} \right). \quad (2.6)$$

The first summand in Eq. 2.6 reflects the screened Coulomb potential of the core with the effective charge Z_{eff} that depends on the position r and angular momentum l [66]

$$Z_{\text{eff}} = 1 + (Z-1)e^{-a_1 r} - r(a_3 + a_4 r)e^{-a_2 r}. \quad (2.7)$$

The coefficients a_1 , a_2 , a_3 and a_4 are obtained from fitting the experimental data. It is seen that the effective charge Z_{eff} goes to Z as $r \rightarrow 0$ and to 1 as $r \rightarrow \infty$. The second summand in Eq. 2.6 reflects the interaction between the induced dipole moments of the core electrons and the Rydberg electron with the static dipole polarizability $\alpha_c = 9.0760$ au and r_c is a cutoff radius introduced to truncate the unphysical short-range contribution of the polarization potential near the origin [66]. Another contribution one can consider as a correction to the effective potential is a spin-orbit coupling [69]

$$V_{\text{so}} = \frac{\alpha^2}{2r^3} \vec{l} \cdot \vec{s} \frac{dV_{\text{eff}}}{dr} \left(1 - \frac{V_{\text{eff}}}{2} \right)^{-2} \quad (2.8)$$

where α is a fine structure constant. This potential can be approximated [68, 70] as

$$V_{\text{so}} = \frac{\alpha^2}{2r^3} \vec{l} \cdot \vec{s}. \quad (2.9)$$

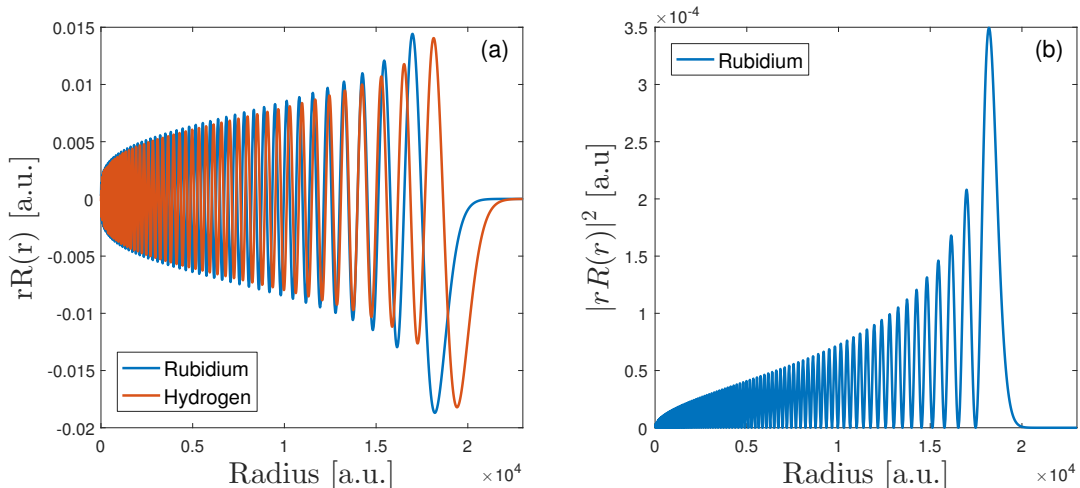


FIGURE 2.1: Radial wave function of ^{87}Rb calculated for 100S state. (a) The comparison between Rubidium wave function and hydrogen wave function. (b) Probability density to find an electron at the position r

Finally we obtain a full potential that is the sum of effective potential and spin-orbit correction $V_{\text{eff}} + V_{\text{so}}$ that one should use in Eq. 2.5 to calculate the radial wave function. It is impossible to find an analytic solution to those equation, thus $R(r)$ can be calculated by numerical integration of Eq. 2.5. In the literature a square root scaling is used to perform such an integration [71]

$$\tilde{r} = \sqrt{r}, \quad \tilde{R} = r^{3/4}R(r), \quad (2.10)$$

and we use Numerov algorithm to solve Eq. 2.5. Following [68] we choose the core radius $\alpha_c^{1/3}$ as a minimal inner bound for integration and the outer edge of the wave function $r_\infty = 2n(n+15)$, that is sufficiently bigger than the classical inner turning point of the wave function. For high values of l we set minimum inner bound to the classical inner turning point $(n^*)^2 - n^*\sqrt{(n^*)^2 - l(l+1)}$. The boundary conditions for integration are $\tilde{R}(r_\infty) = 0$ and $\partial\tilde{R}(r_\infty)/\partial\tilde{r} \lesssim 0$.

Fig. 2.1(a) shows the calculated wave function for ^{87}Rb at 100S state and hydrogen wave function for comparison. It is seen that both wave functions of electrons have strong oscillatory character, but there is a significant shift between these two wave functions that arises from the fact that the binding energy of a Rubidium valence electron is higher. Fig. 2.1(b) depicts the probability density to find an electron at the position r . It is clear that the electron is mostly found at large distances from the core.

2.1.3 Rydberg Atoms in Electric Field

Another remarkable property originating from the large separation of a valence electron and ionic core is a high sensitivity of Rydberg atoms to electric field.

Interaction between the field and the atom can be represented by the operator [72]

$$V_E = -\vec{d} \cdot \vec{\mathcal{E}} \quad (2.11)$$

where $\vec{\mathcal{E}}$ is an electric field and \vec{d} is a dipole moment operator. Therefore to find the eigenstates and eigenenergies of the system one has to diagonalize the Hamiltonian of the form

$$H = H_{\text{atom}} - \vec{d} \cdot \vec{\mathcal{E}} \quad (2.12)$$

If the effect of electric field is small and results only to a tiny shift of the levels, one can treat V_E as a first order perturbation to the atomic Hamiltonian H_{atom} . The energy shift of the state with principal quantum number n can be calculated as the average value

$$\delta E_n = \langle n | V_E | n \rangle. \quad (2.13)$$

It is known [72] that the operator \vec{d} has odd parity, and consequently has nonzero matrix elements only between two states of opposite parity.

In hydrogen, due to degeneracy, states $|nlm_l\rangle$ with the same energy E_n can have different parity that is $(-1)^l$ and the true state would be a linear combination of such states of different parity

$$|n\rangle = \sum_{lm_l} a_{nlm_l} |nlm_l\rangle. \quad (2.14)$$

Thus, Eq. 2.13 will involve terms like $\langle nlm_l | d | nlm_l \rangle \neq 0$, leading to a nonzero shift δE_n . This is a result of special nature of the Coulomb potential, which does not separate parity eigenstates. The same also holds for Rubidium atoms with $l > 4$, where the states are also degenerate and possess different parity and therefore Stark effect is linear with the applied electric field.

But it is not the case for all other atoms including Rubidium with $l \leq 4$, where the correction to Coulomb potential is sufficient to lift up the degeneracy, and each energy level has states of only one parity. The average in Eq. 2.13 for such a state is identically zero. Therefore one has to use the second order perturbation

$$\delta E_{nlm_l} = \sum_{n'l'm'_l} \frac{\langle nlm_l | V_E | n'l'm'_l \rangle \langle n'l'm'_l | V_E | nlm_l \rangle}{E_{nlm_l} - E_{n'l'm'_l}}, \quad (2.15)$$

which results in a quadratic Stark shift

$$\delta E_{\text{Stark}} = -\frac{1}{2} \alpha \mathcal{E}^2 \quad (2.16)$$

with the polarizability α that depends on the absolute value of the projection of total angular momentum $|m_j|$. The sign of the polarizability α depends on the energy difference of the adjacent states and coupling strength and the value can be numerically calculated. For example, for 100S state with $m_j = 1/2$ we obtain the value of $6.2 \text{ GHz V}^{-2} \text{ cm}^2$.

We calculate a Stark map of ^{87}Rb at 100S state, shown in Fig. 2.2. Basically it represents the position of energy levels as a function of electric field. We show two stark maps for two different values of the projection of total angular momentum $|m_j| = 1/2$ (Fig. 2.2(a)) and $|m_j| = 3/2$ (Fig. 2.2(b)). It is clearly seen that for high l states ($l > 4$) Stark effect obeys the linear character (see 97

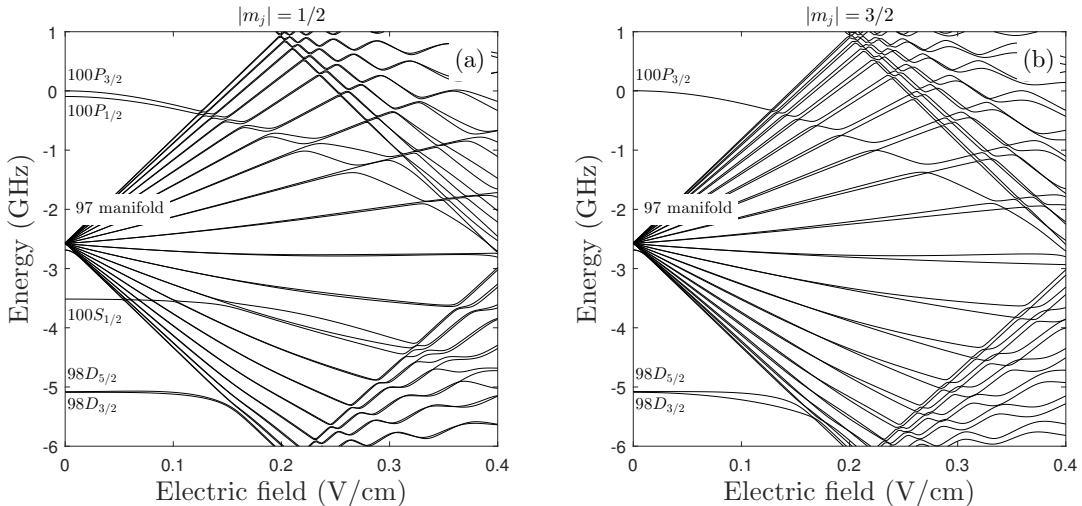


FIGURE 2.2: Stark map of ^{87}Rb calculated for 100S state for $|m_j| = 1/2$ (a) and $|m_j| = 3/2$ (b).

states manifold for example) while for lower l ($l \leq 4$) Stark effect is quadratic in external electric field. For these plots we have restricted the calculations to the span of 10 neighboring states in principal quantum number n and 20 states in angular momentum.

In our experiment Stark effect plays a huge role because it became a daily routine for a cancellation of stray electric fields in the system (for details see Chapter 3.1.5).

2.1.4 Interaction of Rydberg Atoms

Ability of Rydberg atoms to strongly interact with each other lays in the heart of many Rydberg experiments. One of the key properties of Rydberg atoms interaction for the quantum information processing is the ability to turn on and off the two-atom interaction with a contrast of 12 orders of magnitude. Controlling interaction strength over such a wide range appears to be unique to the Rydberg systems [57]. This property of Rydberg atoms was used in some remarkable works from recent years [51, 73, 28, 74, 75].

The general form of the interaction potential between two Rydberg atoms with the dipole moment \vec{d}_1 and \vec{d}_2 and separated by a distance \vec{r} can be written as [76, 77, 78, 79, 80]

$$V_{dd} = \frac{\vec{d}_1 \cdot \vec{d}_2 - 3(\vec{r} \cdot \vec{d}_1)(\vec{r} \cdot \vec{d}_2)/r^3}{4\pi\epsilon_0 r^3} \quad (2.17)$$

Now we consider two non-overlapping atoms A and B , with nuclei separation of distance R . We follow consideration in [57] to write the electrostatic dipole-dipole interaction

$$V_{dd} = \frac{e^2}{R^3} (\vec{a} \cdot \vec{b} - 3\vec{a} \cdot \hat{R}\hat{R} \cdot \vec{b}) \quad (2.18)$$

where \vec{a} and \vec{b} are the positions of the two Rydberg electrons measured from their respective nuclei.

We consider atoms that are excited to the same fine-structure level (extension to the different levels is possible) so that two-atom state for $R = \infty$ can be written

$$|\psi_2\rangle = |\psi_A\psi_B\rangle = |\psi_{nlj}\psi_{nlj}\rangle. \quad (2.19)$$

This state has a degeneracy of $(2j+1)$ in the absence of external fields. The dipole-dipole interaction leads to transitions to different two atom states where the angular momentum quantum numbers of each electron obey the usual dipole selection rules: $l_a, l_b = l \pm 1$, $j_a, j_b = j \pm 0, 1$. Usually, only the small amount of such states, that possess smallest energy difference and largest dipole matrix elements, contribute to the dipole-dipole interaction and others do not play significant role [81]. So, often there is a significant contribution only from another single pair state and thus we consider only two coupled channels $nlj + nlj$ and $n_a l_a j_a + n_b l_b j_b$ with an energy defect $\delta = E_{n_a l_a j_a} + E_{n_b l_b j_b} - 2E_{nlj}$. The eigenstates of this two-level system are linear combinations of states from different channel [81]. We denote $nlj + nlj$ components of the wave function as $|\phi\rangle$ and the $n_a l_a j_a + n_b l_b j_b$ components as $|\chi\rangle$ and then we can write the time independent Schrödinger equation that describes dipole-dipole interaction in the matrix form

$$\begin{pmatrix} \delta \cdot I_\chi & V_{dd} \\ V_{dd}^\dagger & 0 \cdot I_\phi \end{pmatrix} \begin{pmatrix} |\chi\rangle \\ |\phi\rangle \end{pmatrix} = \Delta \begin{pmatrix} |\chi\rangle \\ |\phi\rangle \end{pmatrix}. \quad (2.20)$$

Here V_{dd} is a $\alpha(2j_a+1)(2j_b+1) \times (2j+1)^2$ operator (with $\alpha = 1$ if $n_a l_a j_a = n_b l_b j_b$ and $\alpha = 2$ otherwise), and I_χ and I_ϕ are identity matrices on the $\alpha(2j_a+1)(2j_b+1)$ and $(2j+1)^2$ dimensional Hilbert subspaces of the $|\chi\rangle$ and $|\phi\rangle$ wave function components, respectively. Solving this one for $|\chi\rangle$ and substituting into the second row of Eq. 2.20 we obtain nonlinear eigenvalue equation for $|\phi\rangle$:

$$\frac{V_{dd}^\dagger V_{dd}}{\Delta - \delta} |\phi\rangle = \Delta |\phi\rangle \quad (2.21)$$

Due to the nature of matrix elements of the operator $V_{dd}^\dagger V_{dd}$ that all share dependence on interatomic distance of $1/R^6$ and $\tilde{C}_3 = e^2 \langle r \rangle_{nl}^{n_a l_a} \langle r \rangle_{nl}^{n_b l_b}$, it is convenient to parametrize these van der Waals eigenstates with eigenvalues D_ϕ (which can be calculated using angular momentum algebra [81])

$$V_{dd}^\dagger V_{dd} |\phi\rangle = \frac{\tilde{C}_3^2}{R^6} D_\phi |\phi\rangle \quad (2.22)$$

Knowing the solutions, we insert them into Eq. 2.21 and solve for the Förster energy eigenvalues Δ ,

$$\Delta_\phi(R) = \frac{\delta}{2} - \text{sign}(\delta) \sqrt{\frac{\delta^2}{4} + \frac{\tilde{C}_3^2}{R^6} D_\phi} \quad (2.23)$$

which constitute the R-dependent potential curves between the atoms, correlating to the $nlj + nlj$ eigenstates for large R and describing the states of interest

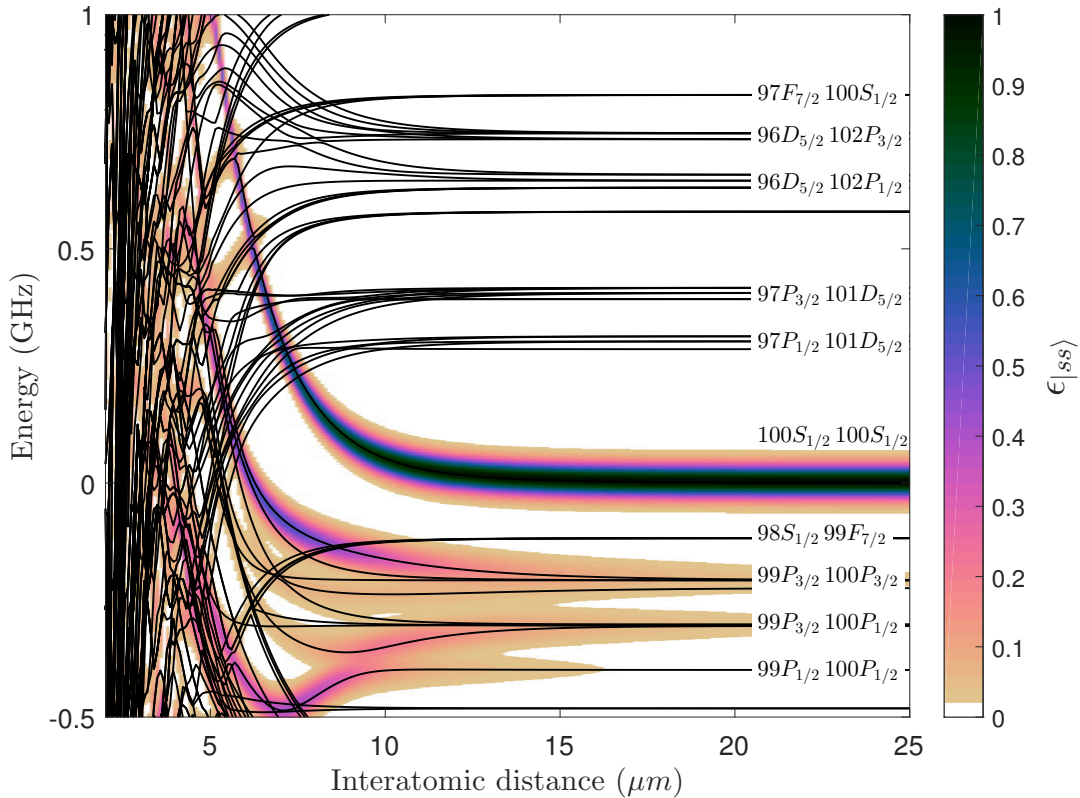


FIGURE 2.3: Potential landscape around the ^{87}Rb $|100S_{1/2} 100S_{1/2}\rangle$. Colormap reflects the admixture $\epsilon_{|ss\rangle}$ to the perturbed pair states.

with energy shifts due to the Rydberg-Rydberg interaction.

We can define crossover distance $R_c = |\tilde{C}_3 \sqrt{D_\phi} / \delta|^{1/3}$ that defines the energies transition from the van der Waals to the resonant form. At large distances $R \gg R_c$ the energy shift is of the classic van der Waals form

$$\Delta_\phi \approx \frac{\tilde{C}_3^2 D_\phi}{\delta R^6} = \frac{C_6}{R^6}. \quad (2.24)$$

with the van der Waals coefficient $C_6 = \tilde{C}_3^2 D_\phi / \delta$. This limit is called van der Waals regime where the interaction potential is proportional to $1/R^6$.

At small distances $R \ll R_c$, the two channels are effectively degenerate and the energy is

$$\Delta_\phi \approx -\text{sign}(\delta) D_\phi \frac{\tilde{C}_3}{R^3} = \pm \frac{C_3}{R^3} \quad (2.25)$$

where $C_3 = \tilde{C}_3 \cdot D_\phi$. This regime provides the largest interaction energy between two Rydberg atoms. The nonzero defect results in a substantial reduction in the interaction strength.

In this thesis the software developed in the group by Weber et al. [82] was used to calculate Rydberg interaction potentials. This software possesses many features, some of them are using different orders of the multipole expansion in the coupling of two atoms (dipole-dipole, dipole-quadrupole, quadrupole-quadrupole, etc.), including interaction with electric or magnetic field pointing in arbitrary direction relative to the inter-atomic axis; or taking into account

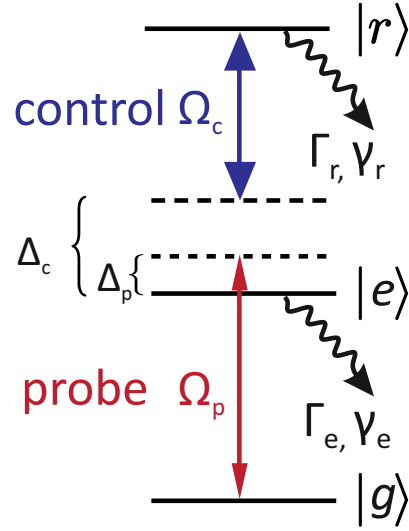
angular dependence of the interaction, which can be mediated by any external electromagnetic field which direction does not coincide with interatomic axis of two atoms (as a result of the coupling of the corresponding eigenstates to the external field being dependent on the angle between the interatomic axis and field direction). As an example of such a calculation, Fig. 2.3 presents the potential landscape around the ^{87}Rb $|100S_{1/2} 100S_{1/2}\rangle$. In this calculation the dipole-quadrupole interaction was included, which results in admixture of the $|100S_{1/2} 100S_{1/2}\rangle$ pair state into several close-lying attractively interacting pair states (such as $|99P_{3/2} 100P_{3/2}\rangle$, $|99P_{3/2} 100P_{1/2}\rangle$ and others). This admixture of $|ss\rangle$ (in our case $|ss\rangle = |100S_{1/2} 100S_{1/2}\rangle$) to any Rydberg pair state $|\Psi\rangle$ is quantified by $\epsilon_{|ss\rangle}(\Delta) = |\langle\Psi|ss\rangle|$ [83, 82] (with Δ being a detuning from the zero energy) and is reflected in Fig. 2.3 as a color map. Such an admixture results in efficient optical excitation of additional Rydberg atoms at specific distances to a first seed excitation.

It is clearly seen that with decreasing distance the pair state $|100S_{1/2} 100S_{1/2}\rangle$ potential is getting shifted towards the high energies which originates from the van der Waals interaction of the Rydberg atoms (see Fig. 2.3). Fitting the calculated potential line with the vdW potential C_6/R^6 , one can obtain C_6 coefficient, which is $4.4 \times 10^4 \text{ GHz } \mu\text{m}^6$ for 100S state that is 18 orders of magnitude higher than those of the $|5S_{1/2} 5S_{1/2}\rangle$ [64, 84]. In general, this shift inhibits excitation of two Rydberg atoms (for example, with the same laser light) within some characteristic volume, called Rydberg blockade volume, because energy of the two-atom excited state is higher than the double energy of a single-atom excited state. The particular conditions for this to happen might be given by the linewidth of the Rydberg state or the excitation light. This effect is called *Rydberg blockade* and it will be discussed later in the context of *Electromagnetically Induced Transparency* (see Chapter 2.2.5).

2.2 Interaction of Light with Atomic Medium

Electromagnetically induced transparency (EIT) is an effect that modifies optical response of an atomic medium by inducing the coherences of an atomic states with laser light. This leads to quantum interference between the excitation pathways that control optical response and eliminates the absorption and refraction at the resonant frequency of a transition. EIT greatly enhances nonlinear susceptibility in the spectral region of induced transparency of the medium and thus is of great importance in atomic physics [85]. In this section we first start with discussing the physical background of EIT in Chapter 2.2.1. Next we discuss the slow down of light in the atomic medium under EIT conditions in Chapter 2.2.2. We discuss the dark-state polariton picture of EIT in Chapter 2.2.3 and the possibility of light storage in Chapter 2.2.4. We finish the section with continuation of the discussion started in Chapter 2.1.4 about the Rydberg blockade, discussing the blockade appearing in EIT in Chapter 2.2.5.

FIGURE 2.4: The typical system for EIT in this work: ladder type three level scheme. The probe field Ω_p couples ground state $|g\rangle$ and intermediate state $|e\rangle$, detuned with the respect to the atomic transition by $\Delta_p = \omega_{eg} - \omega_p$. The control field Ω_c couples intermediate state $|e\rangle$ and Rydberg state $|r\rangle$, detuned by $\Delta_c = \omega_{re} - \omega_c$. The system undergoes a spontaneous emission with the rates Γ_r and Γ_e from the $|r\rangle$ and $|e\rangle$, respectively; and in addition dephasing due to collisions, stray electric fields, thermal motion of atoms and other dephasing mechanisms are included as γ_r and γ_e .



2.2.1 Electromagnetically Induced Transparency

In this chapter we will mostly follow the consideration from [85, 86] to explain the physics behind EIT. We will consider three level system consisting of a ground state level $|g\rangle$, an intermediate state $|e\rangle$ and a long-lived Rydberg state $|r\rangle$ in ladder type configuration (see Fig. 2.4). The transition $|g\rangle - |r\rangle$ is dipole forbidden. The population decay due to spontaneous emission is described by Γ_r (for decay of $|r\rangle$ to $|g\rangle$) and Γ_e (for decay of $|e\rangle$ to $|g\rangle$), and additional dephasing due to collisions, stray electric fields, thermal motion of atoms and other dephasing mechanisms are included as γ_r and γ_e . Two laser fields are used to couple the ground state $|g\rangle$ to the Rydberg state $|r\rangle$: a weak probe field Ω_p couples the ground state $|g\rangle$ and the intermediate state $|e\rangle$ with the detuning from atomic transition $\Delta_p = \omega_{eg} - \omega_p$; and a strong control field Ω_c couples the intermediate state $|e\rangle$ and the Rydberg state $|r\rangle$ with the detuning from the atomic transition $\Delta_c = \omega_{re} - \omega_c$ (ω_p and ω_c are the probe and the control laser frequencies, correspondingly). Here the coupling of the light fields to the atoms is expressed in terms of the Rabi coupling (or Rabi frequency) $\Omega = \boldsymbol{\mu} \cdot \mathbf{E}_0 / \hbar$, with \mathbf{E}_0 being the amplitude of the electric field \mathbf{E} , and $\boldsymbol{\mu}$ the transition electronic dipole moment.

Therefore, the system is described by the Hamiltonian $H = H_{\text{atom}} + H_{\text{int}}$, where H_{atom} is a Hamiltonian of a bare atom and H_{int} comes from interaction with the light fields. Using the rotating frame approximation, interaction Hamiltonian in rotating frame takes a form [85]

$$H_{\text{int}} = -\frac{\hbar}{2} \begin{pmatrix} 0 & \Omega_p & 0 \\ \Omega_p & 2\Delta_p & \Omega_c \\ 0 & \Omega_c & 2(\Delta_c - \Delta_p) \end{pmatrix}. \quad (2.26)$$

In the case of a two photon resonance ($\Delta_p = \Delta_c$), one of the eigenstates of the system is the state

$$|a^0\rangle = \frac{\Omega_c^* |g\rangle - \Omega_p |r\rangle}{|\Omega_c|^2 + |\Omega_p|^2}, \quad (2.27)$$

which has no contribution from the intermediate state $|e\rangle$ and therefore called a dark state. If we start with the system being in the ground state $|g\rangle$, switching on the control light Ω_c does not redistribute the population and it remains in the $|g\rangle$. In the case of the weak probe field $\Omega_p \ll \Omega_c$ applied, the ground state becomes identical to the dark state $|a^0\rangle$ from which excitation cannot occur. Therefore when the weak probe pulse Ω_p arrives to the system (under slow varying amplitude condition), the population adiabatically follows the state $|a^0\rangle$, which is the dark state, and thus absorption from the probe pulse is not possible. This effect is called electromagnetically induced transparency (EIT).

To take more insight into EIT the semi-classical analysis can be applied. The coupling of the atom and the light field can be described by the time-dependent interaction Hamiltonian [85, 87]

$$H_{\text{int}} = -\frac{\hbar}{2} \left[\Omega_p(t) \hat{\sigma}_{eg} e^{i\Delta_p t} + \Omega_c(t) \hat{\sigma}_{re} e^{i\Delta_c t} + h.c. \right], \quad (2.28)$$

where $\hat{\sigma}_{ij} = |i\rangle \langle j|$ is the atomic projection operator ($i, j = g, e, r$). The time evolution of the system in the language of the density matrix is governed by the master equation in the Lindblad form

$$\begin{aligned} \frac{d\rho}{dt} = \frac{1}{i\hbar} [H_{\text{int}}, \rho] &+ \frac{\Gamma_e}{2} [2\hat{\sigma}_{ge}\rho\hat{\sigma}_{eg} - \hat{\sigma}_{ee}\rho - \rho\hat{\sigma}_{ee}] \\ &+ \frac{\Gamma_r}{2} [2\hat{\sigma}_{er}\rho\hat{\sigma}_{re} - \hat{\sigma}_{ee}\rho - \rho\hat{\sigma}_{ee}] \\ &+ \frac{\gamma_e}{2} [2\hat{\sigma}_{ee}\rho\hat{\sigma}_{ee} - \hat{\sigma}_{ee}\rho - \rho\hat{\sigma}_{ee}] \\ &+ \frac{\gamma_r}{2} [2\hat{\sigma}_{rr}\rho\hat{\sigma}_{rr} - \hat{\sigma}_{rr}\rho - \rho\hat{\sigma}_{rr}], \end{aligned} \quad (2.29)$$

where the second and the third terms on the right-hand side describe spontaneous emission from state $|e\rangle$ to $|g\rangle$ and from $|r\rangle$ to $|g\rangle$ with rates Γ_e and Γ_r . And last two terms describe energy-conserving dephasing processes with rates γ_e and γ_r .

In Maxwell's equations polarization plays a role of a source of electromagnetic field, therefore we would like to investigate the polarization generated in the atomic medium by the applied electric fields to study electromagnetic field dynamics [85]:

$$\vec{P}(t) = -\sum \langle e\mathbf{r}_j \rangle / V = \frac{N_{\text{atom}}}{V} \left[\boldsymbol{\mu}_{ge} \rho_{ge} e^{-i\omega_{eg}t} + \boldsymbol{\mu}_{er} \rho_{er} e^{-i\omega_{re}t} + \text{c.c.} \right] \quad (2.30)$$

Here N_{atom} amount of atoms are contained in the volume V , yielding the atomic density $\varrho = N_{\text{atom}}/V$, and been identically coupled to the electromagnetic field. For the case of the weak probe field $\Omega_p \ll \Omega_c$ it is possible to derive the linear

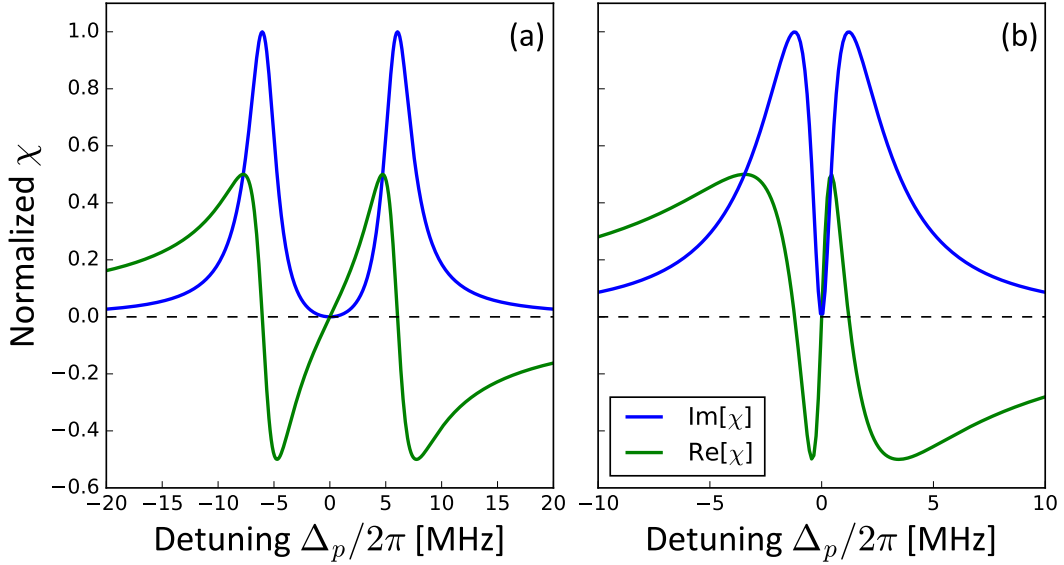


FIGURE 2.5: EIT absorption spectra for different values of the control field and $\gamma_{rg} = 0$, $\gamma_{eg} = 2\pi \cdot 6.05$ MHz: (a) $\Omega_c = 2\gamma_{eg}$; (b) $\Omega_c = 0.4\gamma_{eg}$.

susceptibility χ [85]

$$\chi = \frac{|\mu_{eg}|^2 \rho}{\epsilon_0 \hbar} \left(\frac{4\delta (|\Omega_c|^2 - 4\delta\Delta_p) - 4\Delta_p\gamma_{rg}^2}{\left[|\Omega_c|^2 + (\gamma_{eg} + i2\Delta_p)(\gamma_{rg} + i2\delta)\right]^2} + i \frac{8\delta^2\gamma_{eg} + 2\gamma_{rg} (|\Omega_c|^2 + \gamma_{rg}\gamma_{eg})}{\left[|\Omega_c|^2 + (\gamma_{eg} + i2\Delta_p)(\gamma_{rg} + i2\delta)\right]^2} \right) \quad (2.31)$$

where $\delta = \Delta_c - \Delta_p$; $\gamma_{eg} = \Gamma_e + \gamma_e$ and $\gamma_{rg} = \Gamma_r + \gamma_r$ determine the decay of ρ_{eg} and ρ_{rg} respectively. In general it is also possible to account for the finite laser linewidth by changing the effective linewidths $\gamma_{eg} \rightarrow \gamma_{eg} + \gamma_p$ and $\gamma_{rg} \rightarrow \gamma_{rg} + \gamma_p + \gamma_c$ [88], where γ_p and γ_c are the half linewidths of the probe laser and control laser, respectively (this approach is held only for Lorentzian lineshapes). In the Rydberg experiments with ^{87}Rb one can use the following approximation of the dephasing rates: $\gamma_{eg} = \Gamma_e$ and $\gamma_{rg} = \gamma_r$, which will be implied everywhere later if other is not explicitly used.

The linear susceptibility given by Eq. 2.31 predicts many important features of the EIT. Beyond the modification of the absorption due to the appearance of dressed atomic states it is seen that for two-photon Raman resonance ($\delta = 0$), both the real and imaginary parts of the linear susceptibility vanish in the ideal limit of $\gamma_{rg} = 0$. It is important to note that this result is independent of the strength of the coherent control field and it is shown in Fig. 2.5. For the case when $|\Omega_c| > \gamma_{eg}$, the absorption profile carries the signature of an Autler-Townes doublet: at $\delta = 0$ the loss vanishes and on the high and low energy sides of the doublet absorption is enhanced (Fig. 2.5(a)). For the case, where $|\Omega_c| \ll \gamma_{eg}$ one can observe a sharp transmission window with a linewidth much narrower than γ_{eg} (Fig. 2.5(b)).

In our experiments we work with optically thick media therefore we are

interested in the collective response of the entire medium, which is given by the amplitude transfer function, or in reduced variant as a transmission [85]

$$T = \exp\left(-OD \frac{\gamma_{eg}}{2} \text{Im}[\chi/\chi_0]\right), \quad (2.32)$$

where $OD = 3\lambda_0^2 \rho L / 2\pi$ is an optical depth of the medium (OD), λ_0 is the wavelength of the probe light in vacuum and L is the length of the medium; $\chi_0 = |\mu_{eg}|^2 \rho / \epsilon_0 \hbar$ is the prefactor of the linear susceptibility from Eq. 2.31. The EIT transmission window near the resonance $\delta = 0$ has a Gaussian profile with the width

$$\Delta\omega_{\text{EIT}} = \frac{\Omega_c^2}{\Gamma_e} \frac{1}{\sqrt{OD}}. \quad (2.33)$$

The two remarkable features are that the width of the spectral window in which EIT medium appears transparent decreases with OD and on the other side can be significantly broadened by a strong control field Ω_c . From this, one can see that by decreasing the power of control field and increasing the OD of the medium it is possible to obtain the infinitely narrow transmission peak with a unity transmission. However it is only the case when $\gamma_{rg} = 0$ and including nonzero value into consideration leads to the modification of the transmission value at the resonance $\delta = 0$:

$$T_{\text{max}} = \exp\left(-\frac{OD}{1 + \frac{\Omega_c^2}{\Gamma_e \gamma_{rg}}}\right). \quad (2.34)$$

This restricts the possible values that OD and Ω_c can take in the experiment to observe the EIT transmission window.

The discussed features of the transmission are depicted in Fig. 2.6(a). First of all, the classical two-level absorption valley of $|g\rangle - |e\rangle$ transition is shown as a reference (blue dashed line). Adding the control field coupling to the Rydberg state $|r\rangle$ results in the appearance of a narrow transmission window in the center of the absorption valley (green line) with the transmission reaching unity exactly at the resonance. Adding a dephasing rate of the Rydberg state γ_{rg} results in decreasing of the transmission on resonance (red line); and increasing of the Rabi frequency of the control light broadens the transmission window (black line).

2.2.2 Slow light

In this chapter we consider another remarkable feature arising from the modified linear susceptibility χ . As we have seen from the EIT consideration the coherent dip in EIT can be very narrow which results in the imaginary part of the linear susceptibility χ and, therefore, refractive index \tilde{n} possess large derivatives. As the real and imaginary parts of the refractive index obey the Kramers-Kronig relations, the real part of the refractive index \tilde{n} (the phase index) can have large values and steep gradients [89]. Now we consider the case of frequencies close to two photon resonance $\delta = 0$ and a negligible decay $\gamma_{rg} = 0$, then the real

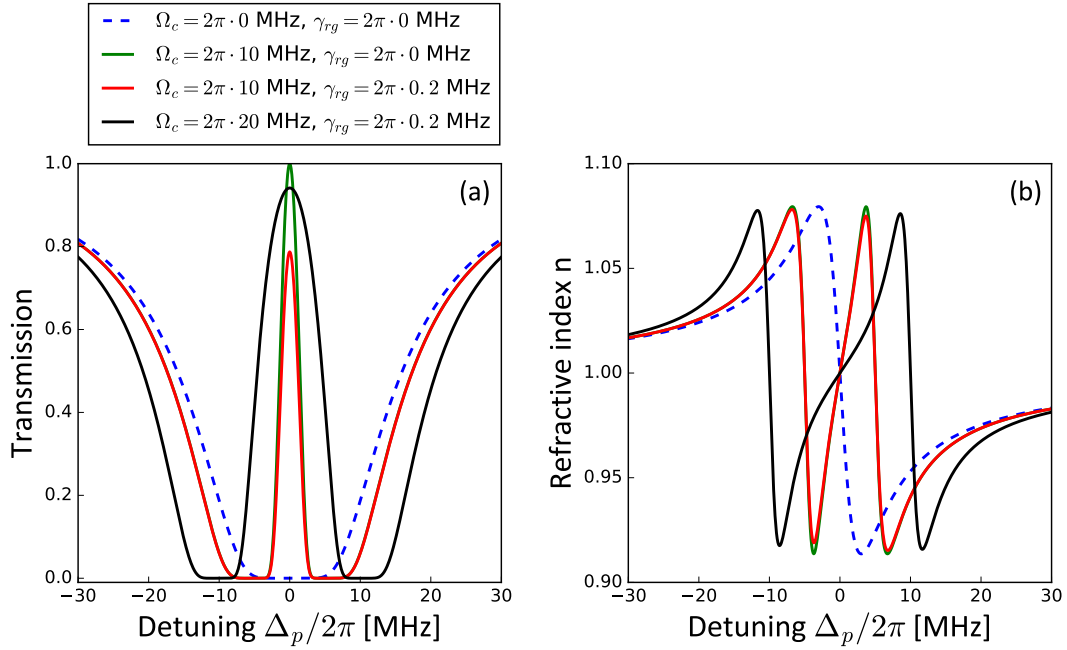


FIGURE 2.6: (a) Transmission spectra of the probe beam for ^{87}Rb for different values of the control Rabi frequency Ω_c and Rydberg state dephasing γ_{rg} : $\Omega_c = 0$ MHz (blue line) depicts the two-level absorption valley; $\Omega_c = 2\pi \cdot 10$ MHz, $\gamma_{rg} = 0$ MHz (green line) and $\gamma_{rg} = 2\pi \cdot 0.2$ MHz (red line) reveal the damping of on-resonance transmission; $\Omega_c = 2\pi \cdot 20$ MHz and $\gamma_{rg} = 2\pi \cdot 0.2$ MHz (black line) reveals the power broadening of the transmission window. (b) Real part of the refractive index vs probe light detuning: refractive index of a two level system (blue line) possesses the anomalous dispersion; EIT changes the dispersion from anomalous to normal with steep gradients around the resonance (green and red line); increasing of the control light Rabi frequency leads to decrease in a gradient around the resonance (black line).

part of the linear susceptibility Eq. 2.31 takes a form of [85]

$$\text{Re}[\chi] = \frac{3\rho\lambda_0^3}{4\pi^2} \frac{2\Gamma_e\delta}{\Omega_c^2} + \mathcal{O}(\delta^2). \quad (2.35)$$

The real part of the refractive index of the medium is $n = \sqrt{1 + \text{Re}[\chi]}$, and due to the fact that the dispersive feature $\text{Re}[\chi]$ changes from anomalous to normal in the case of EIT, the linear dispersion $dn/d\omega_p$ is positive (see Fig. 2.6(b)). This results in the reduction of the group velocity on EIT resonance, according to

$$v_{gr} = \left. \frac{d\omega_p}{dk_p} \right|_{\delta=0} = \frac{c}{n + \omega_p (dn/d\omega_p)}. \quad (2.36)$$

The group velocity can be extremely low, depending on the value of $(dn/d\omega_p)$. For the case of the single photon resonance of the probe field $\Delta_p = 0$, one gets the group velocity

$$v_{gr} = \frac{c}{1 + n_{gr}} = \frac{c}{1 + \rho\sigma_0 c \frac{\Gamma_e}{\Omega_c^2}} \quad (2.37)$$

where $\sigma_0 = 3\lambda_o^2/2\pi$ is the absorption cross section of an atom. The reduction in the group velocity results in the group delay of a probe pulse inside of the medium of the length L :

$$\tau_d = L \left(\frac{1}{v_{gr}} - \frac{1}{c} \right) = \varrho \sigma_0 L \frac{\Gamma_e}{\Omega_c^2} = OD \frac{\Gamma_e}{\Omega_c^2}. \quad (2.38)$$

The important fact to be noted is that in the imperfect case of $\gamma_{rg} \neq 0$ (due to collisions of atoms or fast phase fluctuations in the laser fields) the value of $n_{gr} = \varrho \sigma_0 c \Gamma_e / \Omega_c^2$ has to be replaced by the $n_{gr} = \varrho \sigma_0 c \Gamma_e / (\Omega_c^2 + \gamma_{rg} \gamma_{eg})$. In this case the group velocity takes a higher values for the same density ϱ .

One important property of the lossless propagation of the slowed down light pulse is the spatial compression in the propagation direction [85]. The compression factor is defined by the ratio of the group velocity to the speed of light v_{gr}/c outside the medium. It happens because at the entrance of the medium the front part of the pulse, that is already inside of the medium, propagates much slower than the back part of the pulse. However the electrical field strength stays the same. And when the pulse leaves the medium situation is opposite.

To obtain extremely low values of the group velocity, it is important to satisfy the condition of perfect transparency $\delta = 0$, use very high atomic densities ϱ and low intensities of the coupling filed $I_c \sim \Omega_c^2$ (see Fig. 2.6(b)). The most remarkable observations of the slow light were done in the work [90], where it was possible to slow the light down to 17 m/s in a Bose condensate of Na atoms, and in the works [91, 92] where the similar values were achieved in a buffer-gas cell of hot Rb atoms.

2.2.3 Dark-state polaritons

In the previous chapter we discussed the spatial compression of the pulse entering the EIT medium. This compression leads also to the reduction of the total number of probe photons inside of the medium by the factor v_{gr}/c , even though in the absence of losses the time-integrated photon flux through any plane inside of the medium is constant [85]. Thus, electromagnetic energy, or number of photons, must be temporarily stored inside of the combined system of atoms and control field. It happens in the following manner: before the probe pulse arrives to the medium of three-level atoms, all the atoms are in the ground state $|g\rangle$ and the control field does not affect the system. In this limit $|g\rangle$ is identical to the dark state $|a^0\rangle$. When the front part of the pulse enters the medium the dark state $|a^0\rangle$ makes a small rotation from the $|g\rangle$ to the superposition of the $|g\rangle$ and $|r\rangle$ (see Eq. 2.27). In this process energy is taken out of the probe pulse and transferred to the atoms and the control field. This rotation reverses after the probe pulse passes the maximum amplitude point. Therefore, energy is returned back to the probe pulse at its end part. As we know from the Chapter 2.2.2, the weaker the strength of the control field Ω_c the longer time the pulse spends inside of the medium, and thus the longer the excursion of the dark state away from the ground state $|g\rangle$. Mathematical description of

this process is given by a quasiparticle dark-state polariton [93, 86, 85]

$$\Psi(z, t) = \cos \vartheta \mathcal{E}_p(z, t) - \sin \vartheta \sqrt{\varrho} \rho_{rg}(z, t) e^{i\Delta kz} \quad (2.39)$$

with the mixing angle determined by the group index

$$\tan^2 \vartheta = \frac{\varrho \sigma_0 c \Gamma_e}{\Omega_c^2} = n_{gr} \quad (2.40)$$

and \mathcal{E}_p is the normalized, slowly varying probe field strength, $E_p = \mathcal{E}_p \sqrt{\hbar \omega_p / 2 \epsilon_0}$ with ω_p being the probe field frequency; $\Delta k = k_c^\parallel - k_p$, where k_p is the wave number of the probe field and k_c^\parallel is the projection of the control field wave vector along z axis. Under condition of a single-photon resonance, Ψ obeys the simple shortened wave equation

$$\left[\frac{\partial}{\partial t} + c \cos^2 \vartheta \frac{\partial}{\partial z} \right] \Psi(z, t) = 0 \quad (2.41)$$

which describes a form-stable propagation with velocity

$$v_{gr} = c \cos^2 \vartheta. \quad (2.42)$$

Speaking in the language of dark-state polaritons, the slowing down of the group velocity of light in an EIT medium can be considered as a lossless and form-stable propagation of a dark-state polariton through the medium. In essence, a dark-state polariton is a mixture of the electromagnetic and atomic spin excitations. A mixing angle defines the proportion between electromagnetic and atomic components, and consequently the group velocity of the polariton propagating through the medium, and, as it is seen from Eq. 2.40, it depends on the atomic density and the strength of the control field. There are two limits for a dark-state polariton: the first one is when it takes almost purely atomic form, what happens when $\vartheta \rightarrow \pi/2$, and in this case the propagation velocity is close to 0; the opposite case is when a dark-state polariton is almost entirely electromagnetic in nature at $\vartheta \rightarrow 0$ with a propagation speed close to the speed of light in vacuum c .

2.2.4 Storage of light

As it was shown in the previous chapters the slow light propagation through the atomic medium can be described as a propagation of a dark-state polariton, that is a coherent superposition of an electromagnetic and an atomic component, with a group velocity v_{gr} . Therefore, there is a reasonable question if it is possible to completely stop the light in the medium by transferring the electromagnetic component completely to the atomic component, and, thus, store photons in the medium, with a possibility of a subsequent retrieval later in time. To give an answer to this question we consider a pulsed probe light field with a finite spectral width and a medium with an infinitely long-lived dark state (to eliminate the relevant absorption). For the lossless propagation of the pulse through the medium the spectral width of the pulse $\Delta\omega_p$ has to be much

smaller than the transparency window width $\Delta\omega_{\text{EIT}}$ [85]

$$\Delta\omega_p \ll \Delta\omega_{\text{EIT}} = \frac{\Omega_c^2}{\Gamma_e} \frac{1}{\sqrt{OD}} = \frac{\sqrt{OD}}{\tau_d} \quad (2.43)$$

From this we see that it is not possible to completely stop the pulse ($\tau_d \rightarrow \infty$), since the transparency window width would vanish and the pulse would be totally absorbed. To overcome this limitation it was proposed to reduce the group velocity adiabatically to zero in time [86]. The most common way to achieve this is by reducing the control Rabi frequency resulting in the narrowing of the probe pulse spectrum proportional to the group velocity such that it can stay within the transparency window at all times

$$\Delta\omega_p(t) = \Delta\omega_p(0) \frac{v_{gr}(t)}{v_{gr}(0)}. \quad (2.44)$$

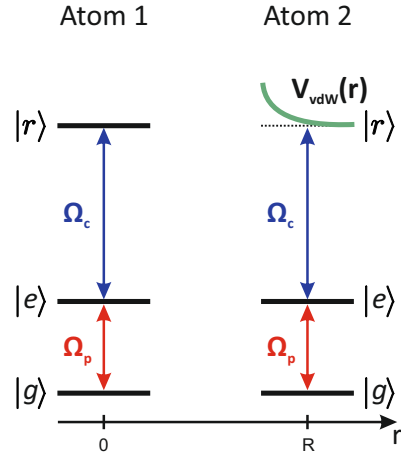
Considering conditions of adiabaticity, it was shown that limitations on the rate of change of the coupling field are rather weak [94, 95]. At the small values of the control field Ω_c and, thus, small velocities v_{gr} even an instantaneous switch off of the electric field would not lead to high losses, only to a loss of the very small electromagnetic fraction of the polariton [94, 25].

It is important to consider the light stopping process in the dark-state polariton picture. The propagation equation Eq. 2.41 is still valid but with the time dependent mixing angle $\vartheta \rightarrow \vartheta(t)$. When the adiabatic rotation from $\vartheta = 0$ to $\vartheta = \pi/2$ is performed, the polariton changes its character from the electromagnetic to pure spin excitation, and this leads to a deceleration of the polariton and, finally, a full stop. It is very important that provided the rotation is adiabatic, all properties of the original light pulse are coherently transferred to the atomic spin system in this process modulo an overall phase determined by that of the coupling field [85]. If we consider a single-photon state of a single radiation mode $|1\rangle_{ph}$ and an atomic cloud consisting of N atoms in the ground state $|g_1, g_2, \dots, g_N\rangle$, then the stored light pulse can be described by a Dicke-like state [95, 96]

$$|\Psi\rangle = \frac{1}{\sqrt{N}} \sum_{j=1}^N e^{i\Delta k x_j} |g_1, \dots, r_j, \dots, g_N\rangle, \quad (2.45)$$

where $\Delta\mathbf{k} = \mathbf{k}_p + \mathbf{k}_c$ is the wavevector of the excitation, x_j describes the position of atom j ; $|g_1, \dots, r_j, \dots, g_N\rangle$ is a collective state with atom j in the Rydberg state $|r\rangle$ and all others in the ground state $|g\rangle$. In this way, EIT medium can act as a quantum memory for photons. Retrieving photons back from the cloud is possible by increasing the strength of the control field Ω_c back, which would result to an opposite rotation of ϑ and acceleration of a polariton with a change of a character from atomic to electromagnetic.

FIGURE 2.7: Rydberg blockade during laser excitation of EIT. The interaction between two atoms lifts up the EIT condition for the atom at position R due to the level energy shift induced by the interaction (green line). The blockade radius is defined by the distance where energy shift is equal to EIT linewidth.



2.2.5 Rydberg blockade on EIT

In this chapter we will describe the effect of a Rydberg blockade in the connection to EIT. The nature of this effect originates from the dipole-dipole interaction of Rydberg atoms, that was discussed in the Chapter 2.1.4, and it results in the strong interaction of dark-state polaritons, when one polariton can turn a part of the medium to be completely absorptive for another polaritons in the medium.

To illustrate this effect we consider a probe pulse propagating in the atomic ensemble on EIT resonance in the form of a dark-state polariton with a large atomic component. If there are two or more photons in the probe pulse, there would be two or more polaritons existing simultaneously in the atomic medium. For simplicity we consider the case of two dark-state polaritons propagating at the distance R between them: due to their atomic components represented by coupling to a Rydberg state $|r\rangle$, they will experience a van der Waals potential $V_{\text{vdW}}(R)$ which results in the energy shift of the state $|r\rangle$. The situation is depicted in Fig. 2.7, where atom at the position 0 is excited to $|r\rangle$, and atom at the position R experiences a modified energy shown by the green line in Fig. 2.7 with the scaling of r^{-6} for the case of van der Waals interaction. From EIT point of view for the polariton at the distance R it means that EIT is tuned out of resonance with the control field detuning $\Delta_c = V_{\text{vdW}}(R)/\hbar$. This results into decoupling of the polariton at the distance R from the Rydberg state and leaving coupling only to the two-level scheme consisting of $|g\rangle$ and $|e\rangle$, which causes absorption of photons and scattering them in 4π solid angle. This allows to define the so-called Rydberg blockade [74]: it is a distance at which the interaction induced shift of the energy of Rydberg state $|r\rangle$ is equal to the EIT linewidth $\hbar\Delta\omega_{\text{EIT}}$ (Eq. 2.33).

For the case of the van der Waals interaction

$$V_{\text{EIT}} = \frac{C_6}{r_b^6} = \hbar\Delta\omega_{\text{EIT}} = \frac{\Omega_c^2}{\Gamma_e \sqrt{OD}}, \quad (2.46)$$

which results in the blockade radius being

$$r_b = \left| \frac{\Gamma_e C_6 \sqrt{OD}}{\Omega_c^2} \right|^{1/6} \quad (2.47)$$

Essentially, the blockade radius defines the region within which it is not possible to excite two Rydberg atoms, or, in the case of propagating polaritons, it is a region within which two polaritons cannot exist at the same time.

The other ways to define the blockade region exist in the literature, such as using a EIT linewidth $\Delta\omega_{\text{EIT}}^{\text{exp}}$ extracted from the experiment as a threshold for the interaction induced energy shift of $|r\rangle$ [28].

The discussed process maps Rydberg-Rydberg interaction on the photons and it can be considered as an quantum optical nonlinearity: a single photon propagates through the EIT medium obeying the description with 3-level EIT susceptibility χ_{EIT} (see Eq. 2.31), while propagation of a second photon would obey the 2-level physics with $\chi_{2\text{-level}}$. The strength of such a nonlinearity depends on the amount of atoms surrounding the Rydberg atom and efficient realization requires high OD per blockade radius [97].

Actually, in the Rydberg-EIT setup there are two regimes of strong quantum nonlinearity [97]. The first one, dissipative nonlinearity, denotes the case when transmission of a single photon is way higher, than transmission of a pair of photons - the case described above. To quantify nonlinearity in this regime, one would measure a second order correlation function $g^{(2)}(t_1, t_2) = \langle n(t_1)n(t_2) \rangle / [\langle n(t_1) \rangle \langle n(t_2) \rangle]$ of the transmitted field for a weak classical input, where t_1 and t_2 are photon detection times, and $n(t)$ is a detection rate. In the case of strong scattering of photon pairs, one observes the anti-bunching feature $g^{(2)}(t_1 = t_2) \ll 1$. The regime of dissipative nonlinearity in the Rydberg-EIT experiment is achieved by setting the detuning of the probe laser Δ_p and control laser Δ_c from the intermediate level $|e\rangle$ to zero.

The second regime is called dispersive regime, when single photon and pair of photons are transmitted equally, but they acquire different optical phases. Such a nonlinearity is considered to be strong if the phase difference ϕ is on the order of π . In the Rydberg-EIT experiment such regime is achieved by detuning the probe and control field from the intermediate state $|e\rangle$. We refer to the review by Firstenberg, Adams, and Hofferberth [97] for the details on the dispersive regime.

2.3 Ultralong-range Rydberg molecules

In this section the extremely short introduction into the field of ultralong-range Rydberg molecules is given. There is no deep studies of the Rydberg molecule physics in this thesis, therefore it is not the aim of this chapter to discuss the rich physics underlying molecule formation. However, one part of the experimental work in this thesis is devoted to the dynamics of EIT medium under the condition of Rydberg molecule formation, therefore it is necessary to provide some very basic overview of the Rydberg molecules.

The field of ultralong-range Rydberg molecules deals with another type of Rydberg atoms interaction that was predicted first by Chris Greene and co-workers in 2000 [52]. They have proposed an interaction between a Rydberg atom and a ground state atom that takes place through the attraction between the electric field of the valence electron of a Rydberg atom and a polarizable ground state atom. This mechanism allows to trap a ground state atom in the potential created by a Rydberg electron and, therefore, form a Rydberg molecule. Of course, one has to take into account a probability density of a Rydberg electron that was discussed in Chapter 2.1.2, and this requires a quantum mechanical treatment of the problem, which is known as a scattering process between the low energy Rydberg electron and the ground state atom.

We will discuss the approach first used by Enrico Fermi in 1934 [98, 99] to treat the quantum mechanical problem of scattering by using the concepts of scattering length and pseudopotential. The idea that stands behind this concept is to treat the Rydberg electron as a quasi-free particle implying that de Broglie wavelength is much larger than some characteristic interaction length (exception are the regions that are very close to the ionic core). Then the scattering process can be described by a s-wave scattering length a_s , which defines the phase shift between ingoing and outgoing wave function outside the region of interaction. The sign of the scattering length defines the interaction to be whether attractive ($a_s < 0$) or repulsive ($a_s > 0$). In this approach the short range features of the potential cannot be resolved, therefore, it is replaced by the pseudopotential (in the first order)

$$V_{\text{pseudo}} = \frac{2\pi\hbar^2 a_s}{m_e} \delta(\mathbf{r} - \mathbf{R}) \quad (2.48)$$

where \mathbf{r} is the position of the Rydberg electron and \mathbf{R} is the position of the ground state atom, m_e is mass of an electron. To find the interaction potential between the Rydberg electron and the ground state atom one needs to average the pseudopotential over the spatial probability distribution of the Rydberg electron $|\psi(\mathbf{r})|^2$

$$V(\mathbf{R}) = \int d\mathbf{r} V_{\text{pseudo}}(\mathbf{r} - \mathbf{R}) |\psi(\mathbf{r})|^2 = \frac{2\pi\hbar^2 a_s}{m_e} |\psi(\mathbf{R})|^2 \quad (2.49)$$

Another more sophisticated approach is based on the effective range theory [100] that was applied to describe the Rydberg electron – neutral atom scattering [101] to extend the description of Fermi to higher order terms. Omitting the details of these calculations, one should replace the scattering length a_s by energy dependent scattering length $a_s(k)$ to take into account the higher order terms in Fermi description. Therefore, one obtains

$$a_s(k) = a_s + \frac{\pi}{3} \frac{\hbar^2}{m_e e^2 a_0^2} \alpha k + \mathcal{O}(k^2) \quad (2.50)$$

where we denote a_s as a zero energy scattering length. The kinetic energy of Rydberg electron can be calculated from the classical expression

$$k(r) = \sqrt{2E_{\text{kin}}} - \sqrt{2(E_{nl} + 1/r)} \quad (2.51)$$

Theoretically predicted value of a_s for ^{87}Rb is $-15.7a_0$ if the Rydberg electron and the ground state atom are in a triplet state (their spins are parallel), where a_0 is the Bohr radius. This allows an attractive interaction and formation of molecules in ^{87}Rb (however, the singlet scattering length is positive, thus no bound state is possible). The ultralong-range Rydberg molecules show very weak binding energies in the MHz frequency range and therefore require ultracold temperatures.

The vibrational ground state wave function of the Rydberg molecules that possesses the highest binding energy per atom is mostly localized at the position of the outermost lobe of the electron wave function, that is, near the classical turning point of the electron [102]. It is also possible that several ground state atoms are trapped in the potential and therefore the Rydberg molecule can be formed by one Rydberg atom and several ground state atoms. Such molecules are generally called polyatomic and they can be described with the same formalism. In this work we deal mostly with the dilute thermal cloud where densities are not that high, thus, the mean distance between ground state atoms is much bigger than the Rb atom-atom scattering length [103]. It results in the possibility to neglect the interaction between ground state atoms within a polyatomic Rydberg molecule. As a consequence, the binding energy of a polyatomic molecule with n ground state atoms is $n - 1$ times larger than the binding energy of a dimer molecule. When the number of atoms within the electron wave function is high the mean field approach has to be pursued instead of the discrete binding energies picture [98, 104]. In this case no individual bound states are resolved, but the Rydberg line is shifted by [102]

$$\begin{aligned} \Delta E &= \iint d\mathbf{r}d\mathbf{R} V_{\text{pseudo}}(\mathbf{r}, \mathbf{R}) |\psi(\mathbf{r})|^2 \rho(\mathbf{R}) = \int d\mathbf{R} V(\mathbf{R}) \rho(\mathbf{R}) = \\ &= \frac{2\pi\hbar^2 a_s}{m_e} \bar{\rho}, \end{aligned} \quad (2.52)$$

where ρ is the ground state atom density and $\bar{\rho}$ is its average weighted with the probability density of the Rydberg electron. If higher order corrections to the zero-energy scattering length can be neglected, the mean shift depends only on the value of a_s and $\bar{\rho}$. This result is independent from the principal quantum number and is breaking down for low principal quantum numbers.

Chapter 3

Experimental Setup

All the experiments in this thesis were performed using ^{87}Rb atoms. All the techniques that were used in the experiment are standard techniques that are used in other similar experiments worldwide. The design and the implementation of the first version of the apparatus were done by the first generation of PhD students, namely Hannes Gorniaczyk and Christoph Tresp, and, of course, the supervisor Sebastian Hofferbert. Therefore, a comprehensive explanations of all the relevant methods can be found in their brilliant dissertations [105, 106]. The second generation of apparatus received the system for electric field control and ion detection that was designed by the master student Johannes Schmidt and described in his master thesis [107]. The author of this thesis has participated in building and tuning of the second generation apparatus and, thus, has a practical experience with all the experimental methods that are relevant for the experiments.

The aim of this chapter is to give a general overview of the experimental stages and provide general information about experimental work that is done on the daily basis, plus highlight some particular points that were not discussed in the above mentioned dissertations.

3.1 Preparation of ultracold atomic sample

In our work we exploit the benefits that arise from using an atomic ensembles at low temperatures and reasonably high densities. The main benefit is that many decoherence mechanisms are suppressed at low temperatures which, in particular, is very important for our experiments on storage and retrieval of Rydberg polaritons (where the coherence time increases with lower temperature) and for experiments on interaction of single polaritons.

3.1.1 Magneto-optical trap

Our experiment starts in the ultra high vacuum chamber made of steel and a glass cell made of quartz attached to it. It is being operated at the pressure level of $\approx 10^{-10}$ mbar. The Rb dispensers are used to create a background Rb gas, which basically limits the pressure in the system. Magneto-optical trap (MOT) is loaded directly from this Rb background [108, 109] (even though the pressure might not seem that good as in other similar experiments such an approach eliminates the complications connected with the usage of MOT

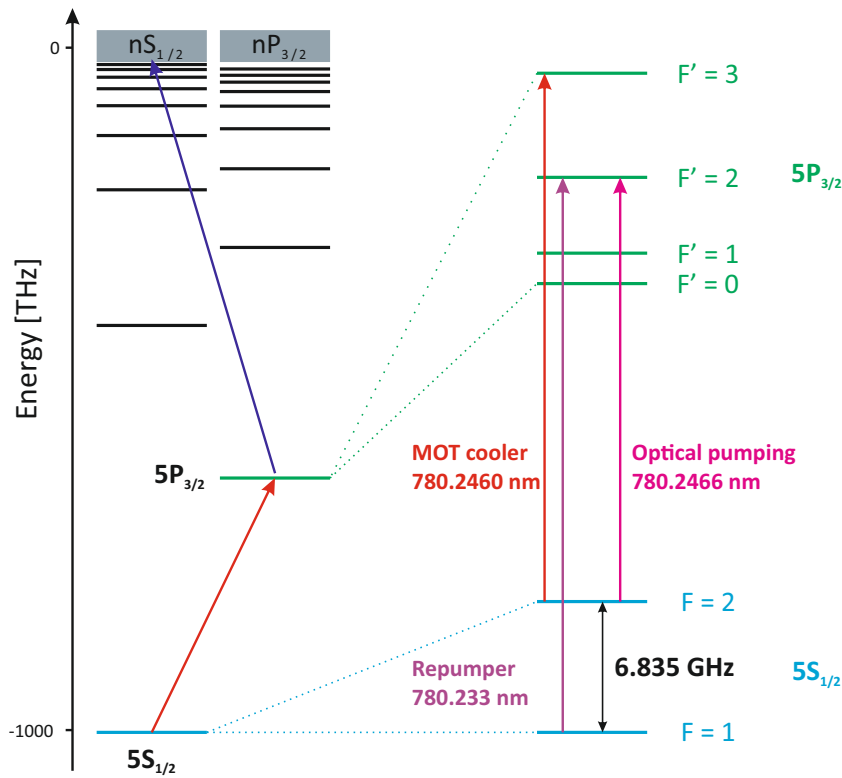


FIGURE 3.1: The very simplified level structure of ^{87}Rb showing only important transitions for cold ensemble preparation. In our experiment we use ^{87}Rb D2 transition line (from $5S_{1/2}$ to $5P_{3/2}$) for atoms cooling and Rydberg excitation. MOT cooler is tuned to the transition between $F = 2$ and $F' = 3$ hyperfine states, while repumper pumps out atoms from $F = 1$ state through $F = 1$ to $F' = 2$ transition. Optical pumping is done by σ^+ polarized light to transfer the population to the dark state $m_F = 2$. Note that the right part of the figure is a schematic representation and not related energetically to the left part.

transfer techniques and is good enough for all the experiments). To obtain a MOT, one requires a laser system and a magnetic field system. The magnetic field system consists of main MOT coils that produce large quadrupole magnetic field necessary for MOT realization, and six offset coils creating homogeneous magnetic field in all three directions. The laser system for MOT consists of two laser lights: MOT cooler and MOT repumper. The respective transitions addressed by these lasers are depicted in Fig. 3.1. The laser cooling is done on the $5S_{1/2}$, $F = 2$ to $5P_{3/2}$, $F' = 3$ transition, since this is the strongest transition in ^{87}Rb . In this process there is an intrinsic loss of population on the $F = 2$ state connected to the possibility of the excitation of $F' = 2$ in the cooling process and subsequent decay to $F = 1$ state. Therefore, repumper laser is used to counteract this loss, which drives the transition $F = 1$ to $F' = 2$ and brings atoms back into the cooling cycle. The MOT cooling cycle is followed by MOT compression and optical molasses phase [87] which results in MOT temperature of around $100\ \mu\text{K}$.

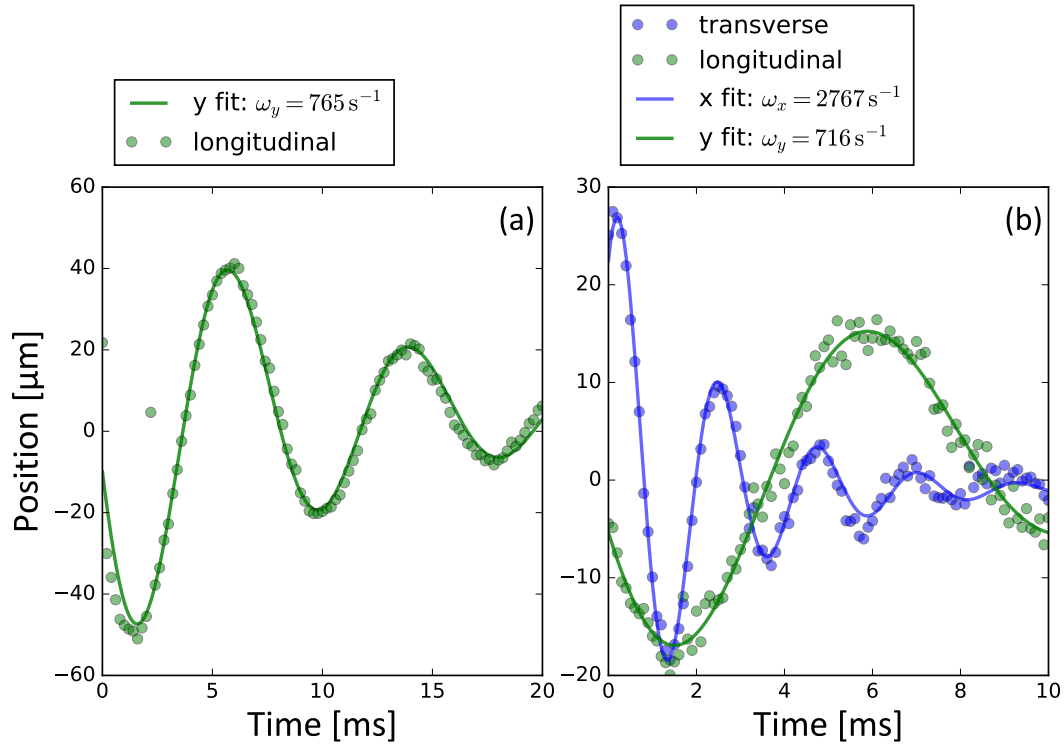


FIGURE 3.2: Measurement of the trap frequencies. (a) Applying a kick with the laser light along the main optical axis that coincides with the long axis of the cigar-shaped cloud (y axis in the laboratory system of coordinates). As a result, atoms in the cloud oscillate in the same direction with the trap frequency $\omega_y = 765 \text{ s}^{-1}$. (b) Applying a kick perpendicular to the main optical axis (x axis in the laboratory system of coordinates) results in the oscillations in both x and y directions due to mutual coupling with the frequencies $\omega_x = 2767 \text{ s}^{-1}$ and $\omega_y = 716 \text{ s}^{-1}$.

3.1.2 Trapping into an optical dipole trap

The next step in the preparation of a cold atomic ensemble is loading atoms in the crossed-beam optical dipole trap (ODT) [110, 111]. In our work we use red-detuned high power laser operated at 1064 nm what is convenient due to the fact that we do not need to lock this laser because the detuning from cooling transition is large and small fluctuations in frequency do not affect the performance; and the excitation probability at this wavelength is very much reduced resulting in the low impact on trapped atoms and, therefore, long lifetime in the trap. Right in the beginning of the MOT loading cycle we turn on two ODT beams, crossed at the angle of 31.4° , possessing Gaussian profile with a waist of $33.4 \mu\text{m}$ at typical optical power of 6.3 W each. This results in the trapping the cigar-shaped cloud with a Gaussian profile: σ_L is a $1/e$ radius of the longitudinal "long" dimension (y axis in laboratory system of coordinates which is a main optical axis of the system) and σ_r is a $1/e$ radius in the transverse "short" dimension (x and z axes in the laboratory system of coordinates). After this, from one to six stages of evaporative cooling are applied to lower the temperature of the cloud [112, 113]. These stages consist of several ramps down to lower values of laser power which results in the gradual

lowering of the depth of the trapping potential, and a final step of holding in the shallow trap. During this procedure the hottest atoms leave the trap and therefore the mean temperature and the total amount of atoms are decreasing. The evaporative cooling step takes a period of time on the order of few hundred ms, and typically one could obtain around 20 000 atoms at approximately 4 μ K, which of course varies for different experiments.

The potential of the dipole trap originates from the ponderomotive force of the laser light [114] and after time-averaging is given by

$$V_p(x) = \frac{e^2 |\mathbf{E}_0(x)|^2}{4m_e \omega_{\text{ODT}}^2}, \quad (3.1)$$

where $\mathbf{E}(\mathbf{x}) = \mathbf{E}_0(\mathbf{x}) \cos \omega_{\text{ODT}}^2 t$ is an electric field of the ODT laser light with the frequency ω_{ODT} . The associated polarizability of the Rydberg state has a different sign than the one for the ground state of ^{87}Rb . It is the reason for only the ground state atoms being trapped in the ODT (attractive potential) but not the Rydberg atoms (repulsive potential).

For characterization of the cloud, necessary for our experiments, we have applied a nice technique that allowed us to obtain trap frequencies of ODT. This technique consists in applying a kick to the atomic cloud with a separate laser light along the main optical axis which coincides with the long axis of the cigar-shaped cloud (y axis in the laboratory system of coordinates), and perpendicular to the main optical axis (along x axis in the laboratory system of coordinates). Such a kick results in the oscillations of atoms in the trap with the corresponding trap frequencies which can be detected as oscillations of the cloud density center position by the standard absorption imaging technique [115, 116, 117]. The results can be seen in Fig. 3.2: applying the longitudinal kick leads to the oscillations only along the same direction (Fig. 3.2(a)), while the transverse kick leads to the oscillations in both directions due to some coupling of these directions, probably caused by misalignment of the pushing laser light (Fig. 3.2(b)). Fitting the exponentially decaying sinus function on the experimental data provides $(\omega_x, \omega_y, \omega_z) = (2767, 765, 2767)$ Hz.

3.1.3 Raman sideband cooling

The degenerate Raman sideband cooling allows to lower temperature of an atomic ensemble without losing atomic density as it happens during the evaporation cooling in the optical dipole trap [118, 119, 120]. This is very important in our experiments because high optical depth (OD) of an atomic cloud is a figure of merit for implementation of strong nonlinearities (see Chapter 2.2).

The principle of the degenerate Raman sideband cooling is illustrated in Fig. 3.3(a). First of all, all the atoms have to be pumped to the $|5S_{1/2}, F = 1\rangle$ state. There are two main components required for an implementation of the Raman sideband cooling scheme: the first one is a 3D optical lattice which allows to generate a three dimensional periodic potential similar to a harmonic oscillator potential. The spacing between vibrational level ν (that represent the kinetic energy of the atoms) has to be higher than the linewidth of the Raman transition between them. The second component is a magnetic field

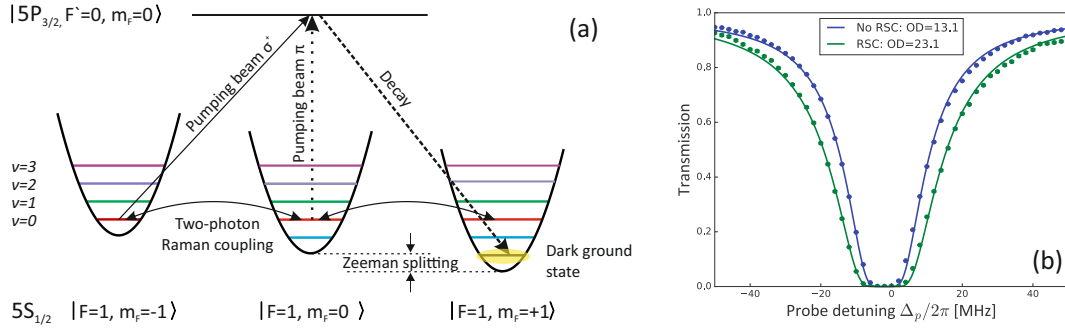


FIGURE 3.3: (a) The scheme of degenerate Raman sideband cooling. The Zeeman shift is identical to vibrational level spacing, all the levels with the same energy are marked with the same color. The pumping light pumps all the atoms into $m_F = 1$ hyperfine state and the two-photon Raman transition lowers the vibrational state of the atoms. The state with $m_F = 1$ and $\nu = 0$ is a dark ground state of the system (highlighted with yellow) and is reached after multiple cooling cycles. (b) The example of an impact of Raman sideband cooling on the OD in our experiment: OD changes from 13.1 in the case of no cooling (blue line) to 23.1 with the cooling (green line).

whose amplitude should be set such that the Zeeman splitting of the hyperfine sublevels m_F matches exactly the spacing of the vibrational levels in the lattice. Such a combination of an optical lattice and a magnetic field results in the particular combination of levels being degenerate, namely all the levels with the identical values of $\nu - m_F$ possess equal energies (levels with equal energies are marked with similar colors in Fig. 3.3(a)).

The next step is to pump atoms in the lowest hyperfine state $m_F = 1$. For this we use a pumping beam that drives the transition from $|5S_{1/2}, F = 1\rangle$ to $|5P_{3/2}, F' = 0\rangle$ that has strong σ^+ component and weak π component to pump the atoms out of $m_F = 0$ hyperfine state. This pumping procedure happens with preserving the vibrational quantum number ν therefore after one cycle we obtain atoms in $m_F = 1$ distributed among the different vibrational levels ν . The state $m_F = 1, \nu = 0$ is a state with the lowest energy and also a dark state of the system, therefore, atoms cannot leave this state. The atoms from the higher vibrational states can undergo the two-photon Raman transition to the neighboring hyperfine state, however, the condition for this transition is that the energy difference between initial and final states has to be close to zero. It means that the atoms from $m_F = 1$ and $\nu > 0$ will undergo a transition to $m_F = 0$ and $m_F = -1$ with the reduction of the vibrational quantum number ν . And later they will be pumped back to $m_F = 1$ state by the pumping light but to new positions with lower energies. Finally, all the atoms will be accumulated in the dark state with a minimal energy, which leads to decreasing the temperature of the atomic ensemble.

The details on the calculations and experimental realization of this scheme can be found in the bachelor thesis of Christoph Braun [121] and PhD thesis of Christoph Tresp [106]. The example of an impact it makes on OD in our system is shown in Fig. 3.3(b), where OD changes from 13.1 to 23.1 if Raman sideband cooling is turned on. This clearly shows the benefit RSC brings to the

system.

3.1.4 Optical pumping

The cooling cycle leaves the atoms being distributed randomly over all the m_F sublevels of the $|5S_{1/2}, F = 2\rangle$ state (degeneracy of these states is lifted due to the presence of magnetic field). To prepare clean quantum experiments all the atomic population has to be pumped to the single sublevel and therefore the cycle of an optical pumping is performed to achieve this [122, 123]. The pumping light is σ^+ polarized and couples $|5S_{1/2}, F = 2\rangle$ with $|5P_{3/2}, F' = 2\rangle$; in addition σ^+ polarized repumper light overlapped with an optical pumping beam couples $|5S_{1/2}, F = 1\rangle$ and $|5P_{3/2}, F' = 2\rangle$ (see the level scheme in Fig. 3.4(a)). Such a combination of laser lights allows to transfer all the population to the stretched state $|5S_{1/2}, F = 2, m_F = 2\rangle$. The comprehensive explanation of optical pumping realization in our experiment can be found in the thesis of Hannes Gorniaczyk [105].

Optical pumping is an important step in the experiment and understanding the quality of an optical pumping is an essential task. For this we have developed the quantum simulations of the optical pumping process by solving the atomic master equation [89]

$$\partial_t \tilde{\rho} = -\frac{i}{\hbar} [\tilde{H}_A + \tilde{H}_{AF}, \tilde{\rho}] + \Gamma \left(\frac{2J_e + 1}{2J_g + 1} \right) \sum_q \mathcal{D}[\Sigma_q] \tilde{\rho} \quad (3.2)$$

Here H_A is an atomic Hamiltonian given by

$$\begin{aligned} \tilde{H}_A = & \sum_{F_e m_e} [\Delta E_{\text{hfs}}(J_e, I, F_e) - \hbar\Delta] |J_e, I; F_e, m_e\rangle \langle J_e, I; F_e, m_e| \\ & + \sum_{F_g m_g} [\Delta E_{\text{hfs}}(J_g, I, F_g) - \hbar\Delta] |J_g, I; F_g, m_g\rangle \langle J_g, I; F_g, m_g| \end{aligned} \quad (3.3)$$

where $\Delta = \omega - \omega_0$ with laser frequency ω , and ω_0 is the transition frequency for the transition center of gravity (i.e., corresponding to the energy difference in the absence of the hyperfine interaction). ΔE_{hfs} is a hyperfine energy shift

$$\begin{aligned} \Delta E_{\text{hfs}}(J, I, F) = & \frac{1}{2} A_{\text{hfs}} K + B_{\text{hfs}} \frac{\frac{3}{2} K(K+1) - 2I(I+1)J(J+1)}{4I(2I-1)J(2J-1)} \\ & + C_{\text{hfs}} \frac{5K^2(K/4+1) + K[I(I+1) + J(J+1) + 3] - 3I(I+1)J(J+1)}{I(I-1)(2I-1)J(J-1)(2J-1)} \\ & - C_{\text{hfs}} \frac{5I(I+1)J(J+1)}{I(I-1)(2I-1)J(J-1)(2J-1)} \end{aligned} \quad (3.4)$$

where J is a quantum number of a total atomic angular momentum, I is a quantum number of a total nuclear angular momentum, $\mathbf{F} = \mathbf{J} + \mathbf{I}$ is a hyperfine quantum number, $K = F(F+1) - I(I+1) - J(J+1)$, A_{hfs} , B_{hfs} and C_{hfs} are usually experimentally measured hyperfine constants (the calculation is possible but might be complex). Indexes g and e refer to ground state and excited state.

The atom–field interaction Hamiltonian in the rotating frame is given by

$$\tilde{H}_{AF} = \frac{\hbar}{2} \sum_q [\Omega_q^* \Sigma_q + \Omega_q \Sigma_q^\dagger] \quad (3.5)$$

where q defines the polarization of light (-1 is σ^+ , 0 is π , $+1$ is σ^-), and Σ_q is defined by

$$\Sigma_q = \sum_{F_g m_g F_e m_e} (-1)^{F_e + J_g + 1 + I} \sqrt{S_{F_g F_e}} \langle F_g m_g | F_e m_e; 1 q \rangle |F_g m_g\rangle \langle F_e m_e| \quad (3.6)$$

where $\langle F_g m_g | F_e m_e; 1 q \rangle$ is a Clebsch–Gordan coefficient, and $S_{FF'}$ being a Wigner 6-j symbol with a prefactor

$$S_{FF'} = (2F' + 1)(2J + 1) \left\{ \begin{matrix} J & J' & 1 \\ F' & F & I \end{matrix} \right\}^2 \quad (3.7)$$

Finally the Lindblad superoperator $\mathcal{D}[\Sigma_q]\tilde{\rho}$ is defined as

$$\mathcal{D}[c]\rho = c\rho c^\dagger - \frac{1}{2} (c^\dagger c\rho + \rho c c^\dagger) \quad (3.8)$$

with $\tilde{\rho}$ being the density matrix.

The example of such a simulation is presented in Fig. 3.4(b), where we show the populations of relevant m_F sublevels varying with time during optical pumping cycle. There we include 13 levels, depicted in Fig. 3.4(a), in the consideration and two laser lights, namely optical pumping and repumper discussed above. All the relevant experimental parameters (intensities, detunings, etc.) are set explicitly such that there is no single free parameter in the calculation. We set the all initial population to be in $|F = 1, m_F = 1\rangle$ state (this is motivated by the fact that RSC brings all the population to this state), then we set intensity of the optical pumping to be $0.11I_{\text{sat}}$ and intensity of the repumper to be $0.15I_{\text{sat}}$ (I_{sat} is the saturation intensity [89]); the polarization of the optical pumping being 99% σ^+ and 1% σ^- , while the polarization of the repumper is 100% σ^+ . In Fig. 3.4(b) we see that the population of the $|F = 1, m_F = 1\rangle$ (green line) is decreasing while the populations of the $|F = 2, m_F = 1\rangle$ (blue line) and $|F = 2, m_F = 2\rangle$ (yellow line) are increasing. This beginning step is a result of the σ^+ polarized repumper that populates these both states. Then the optical pumping light starts to transport the population from the $|F = 2, m_F = 1\rangle$ to $|F = 2, m_F = 2\rangle$.

In the experiment it is not easy to measure the populations of the individual levels. To relate such a calculation to the experiment we perform the probing experiments with the additional probe light tuned into $F = 2 \rightarrow F' = 2$ resonance. Scanning the frequency of the probe light around the resonance frequency we monitor the transmission of the light through the atomic medium consisting of several two-level transitions with different frequencies. If the population distributed among different m_F sublevels of the $F = 2$ state, one should observe a significant absorption. On the other hand if all the population is concentrated at $|F = 2, m_F = 2\rangle$, which is a dark state of the system, the probe light should

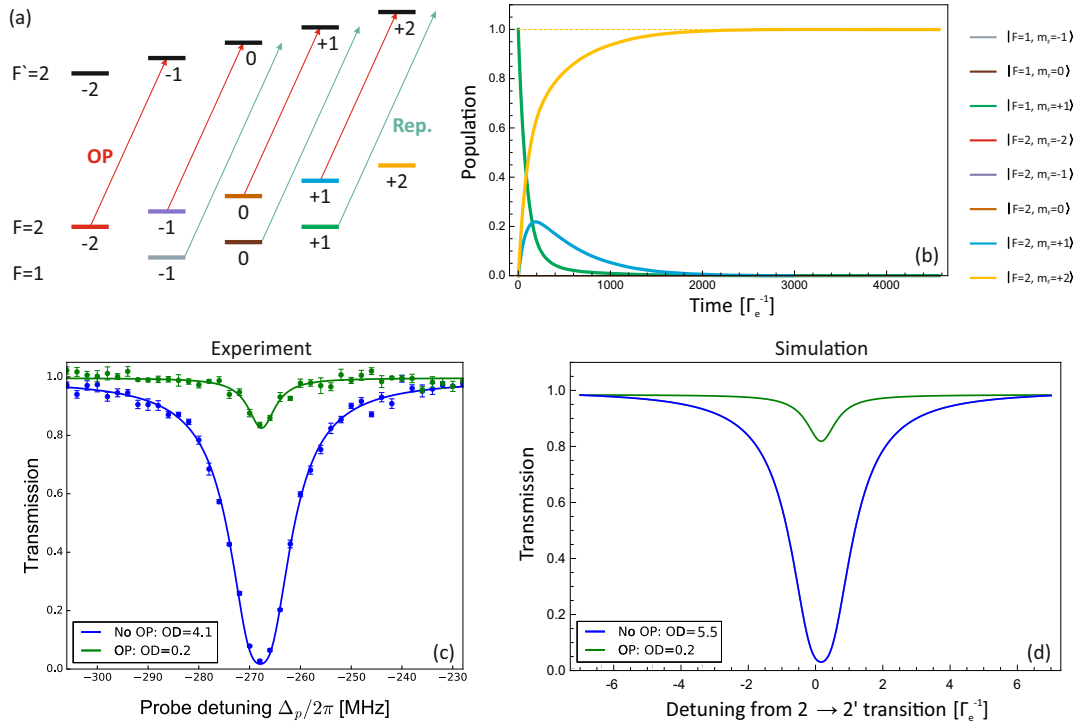


FIGURE 3.4: (a) The level scheme of the optical pumping. The numbers below the levels denote m_F quantum numbers. (b) The simulation without free parameters of the population evolution of the levels from (a) during the optical pumping process. (c) Measurement of the transmission spectra of the $F = 2 \rightarrow F' = 2$ transition. Without optical pumping (blue line) the atoms are distributed over all m_F sublevels of $F = 2$ state which results in the absorption of light. With optical pumping (green line) most of the atoms are in $|F = 2, m_F = 2\rangle$ sublevel which is a dark state and therefore absorption is significantly reduced. Note that presented spectrum does not reveal the best adjustment of the optical pumping. (d) The corresponding simulations of the transmission spectra reveal a good agreement with the experiment.

pass through the medium unaffected. This is shown in Fig. 3.4(c), where the blue line was measured with the optical pumping switched off, revealing absorption with extracted $OD = 4.3$; and the green line is measured with the optical pumping switched on, which significantly decreases the absorption to $OD = 0.2$. The corresponding simulations without free parameters are shown in Fig. 3.4(d): we simulate the transmission spectrum based on the populations of m_F sublevels. It is seen that simulations can well reproduce the experimental behavior, therefore providing a very powerful tool to control the quality of the optical pumping.

3.1.5 Electric field control

In our experiment it is also possible to control electric fields in the cloud, field ionize Rydberg atoms and detect ions on the microchannel plate detector (MCP). This feature was implemented in the second version of the experimental apparatus by adding a set of electrodes to the vacuum chamber, depicted in Fig. 3.5. The electrodes are designed following Löw configuration [56]: they

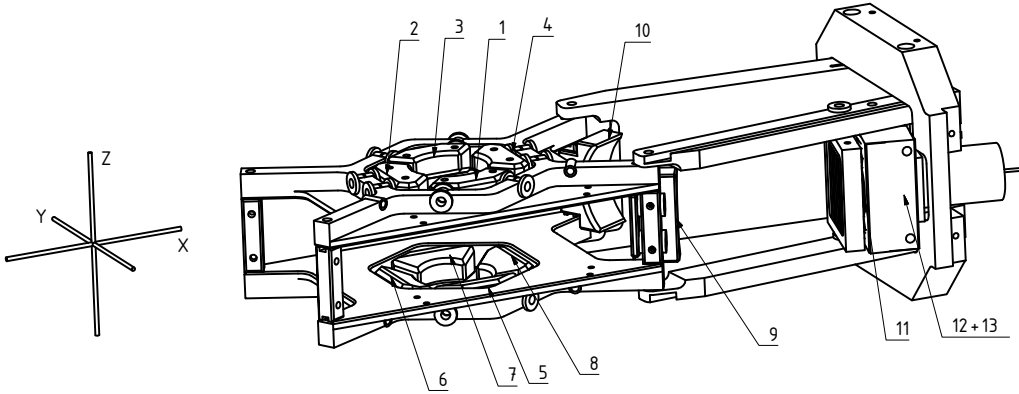


FIGURE 3.5: The scheme of an electric field control system in our experiment. The electrodes 1-8 are used to control the electric field in the atomic cloud positioned in the point center of symmetry of two electrode rings. Electrodes 2 and 6 are used for field ionization and electrode 9 is used for steering the ions towards MCP (electrodes 12 and 13). Electrode 11 is a mesh for shielding the cloud area from electric fields created by MCP. Electrode 10 is a steering electrode and not used in our implementation.

form two rings where the cloud position is right in the point of symmetry of these rings. Electrodes 1-8 are used to control the fields in the cloud. Usually electrodes 2 and 6 are also used to ionize atoms in the cloud (in addition electrodes 4 and 8 can be also used for ionization) and electrode 9 is used to guide the atoms to MCP (electrodes 12 and 13 plus a shielding mesh 11). The details on the design and construction can be found in the master thesis of Johannes Schmidt [107] and PhD thesis of Hannes Gorniaczyk [105]. The details on the MCP characterization can be found in the bachelor thesis of Thomas Dieterle [124]. The electric field configuration can be simulated using commercial software SIMION, which allows to calculate an electric field at any point of the geometry with any potential configuration on the electrodes. As well it is possible to simulate the trajectories of the ions after the ionization of the cloud. Therefore, such calculations were used to find the conversion factors for our system and set the initial parameters for an optimization.

As an example, on the daily basis we perform a stray field cancellation procedure. To find out what stray fields are present in the system we have to sense them. For this we use Stark map spectroscopy the background for which is give in Chapter 2.16. In the experiment we detune the control laser used for Rydberg excitation by $\Delta_c/2\pi = 100$ MHz and measure the transmission spectra of the light through the medium. As well, after each experimental realization we ionize Rydberg atoms and detect the ions on MCP. On top of this we scan the electric field in one particular direction and therefore obtain a 2D Stark map: it is possible to use two-photon absorption spectrum or ion spectrum measured by MCP (see Fig. 3.6). We fit the the parabola to the resonant detunings

$$\Delta_p = \Delta_p^0 + \frac{\alpha}{2}(\mathcal{E}_x - \mathcal{E}_x^0) \quad (3.9)$$

and obtain the offset field that needs to be corrected for. Applying this procedure to all three directions independently we are able to compensate the stray

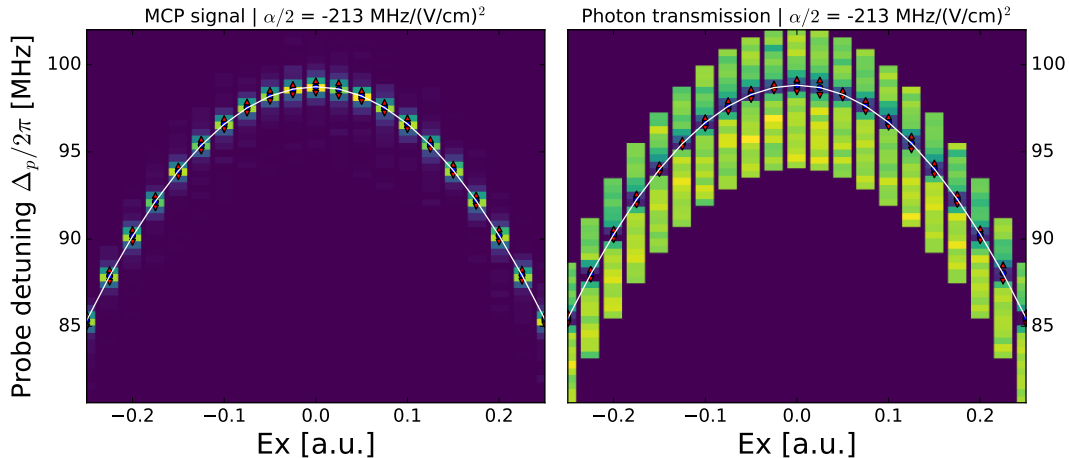


FIGURE 3.6: Stark maps in x direction measured with two-photon absorption spectrum and ionization spectrum at the control field detuning $\Delta_c/2\pi = 100$ MHz. Fitting the parabola allows to correct for an offset field.

fields in all of them. This method also allows to measure the polarizability of Rydberg atoms in the particular state with a good precision if the fields are compensated.

3.2 The laser system for EIT experiments

After the atomic sample is prepared we can perform experiments in it. The experimental system shown in Fig. 3.7 serves for this purposes. To build up an EIT in the medium or perform an excitation of a Rydberg atom we use a pair of counterpropagating lasers: the first is the probe laser which drives the transition from $|5S_{1/2}, F = 2, m_F = 2\rangle$ to $|5S_{1/2}, F = 3, m_F = 3\rangle$ with the wavelength around 780.2 nm and σ^+ polarization (Probe 1 and Probe 2 in Fig. 3.7). The second laser is the control laser that drives the transition from $|5S_{1/2}, F = 3, m_F = 3\rangle$ to $|nS_{1/2}, m_J = 1/2\rangle$ with the tunable wavelength around 480 nm and σ^- polarization (Control 1 and Control 2 in Fig. 3.7). In our setup there is a pair of probe beams and a pair of control beams, which provides an opportunity to perform two-color experiments, such as a single photon transistor. Both probe and control laser lights are coupled into the polarization maintaining single mode fibers for spatial profile filtering and such delivered to the chamber. As well, initially, the polarization out of the fiber is filtered by propagation through a polarizing beam splitter (PBS), and later polarization is controlled by the combination of a quarter waveplate $\lambda/4$ and a half waveplate $\lambda/2$. Such a combination allows to produce clean σ^+ or σ^- polarization in the cloud with a possibility of a compensation of undesired polarization changes due to propagation through other optical elements including the glass cell. Note that the quantization axis is defined by the magnetic field applied during an experimental realization which points along the long axis of the cloud. The control laser is frequency stabilized by locking a frequency sideband to the ultra-stable reference cavity with the Pound-Drever-Hall technique [125]. The same technique is used to stabilize our master laser, which is used for a beat-note offset lock of the probe laser [126]

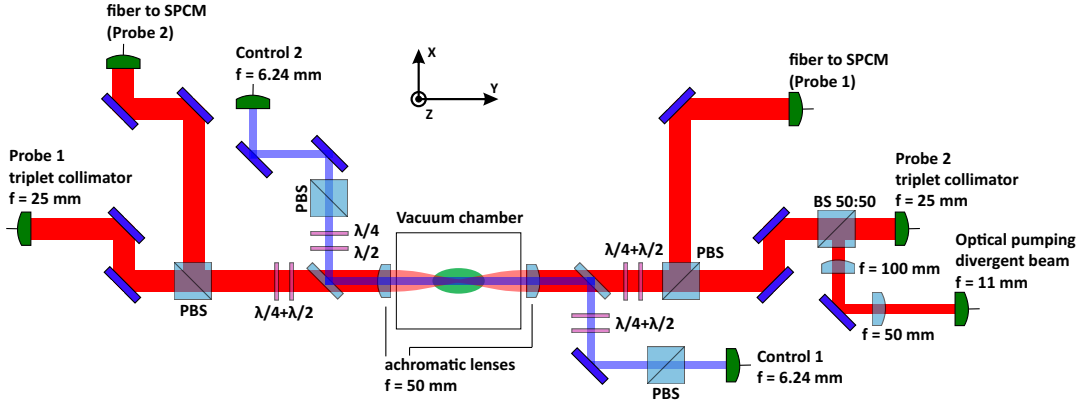


FIGURE 3.7: The illustration of an optical setup used to perform quantum optics experiments in our group. A pair of probe beams at 780 nm (Probe 1 and Probe 2) are focused into the cloud down to $6.2\ \mu\text{m}$ and a pair of control beams at 480 nm (Control 1 and Control 2) are focused down to $14\ \mu\text{m}$, which allows to excite polaritons or stationary Rydberg atoms with at two different principal quantum numbers at a time. The polarization of each laser beam is controlled by the combination of a $\lambda/4$ and a $\lambda/2$ waveplates. Fiber coupled single photon modules (SPCM) are used to detect the transmitted radiation of the probe lasers.

(and other lasers in the experiment). The details on locking the lasers can be found in the master thesis of Christoph Tresp [127].

Both laser lights pass through the achromatic lenses to be focused into the middle of the atomic cloud. These lenses are positioned right in front of the glass cell outside the vacuum to avoid the complications with stray electric fields that could be produced by the surface charges on the dielectric lenses. It allows us to focus the probe beam down to $6.2\ \mu\text{m}$ waist, which grants the condition of 1D propagation for polaritons at high principal quantum numbers (where blockade radius is bigger than the possible excitation region). The control laser is focused down to $14\ \mu\text{m}$ waist to achieve the homogeneous distribution of the light field over the full width of the probe beam.

After the probe light leaves the glass cell it is collimated with the second achromatic lens and coupled to a single mode fiber, which is protected from the stray light with laser line filters. The fiber leads to the Hanbury, Brown and Twiss setup where the beam is split and detected on few single photon counter modules (SPCM). Such an approach allows to overcome the limitation on the counting rate set by the dead time of a single module, plus it allows to calculate a second order correlation function for the measured data. The TTL pulses produced by SPCM are processed with the FPGA based time tagger, that possesses 20 ps time resolution and produced by *Swabian Instruments* (one could find more details in the thesis of one of the founder of the company Michael Schlagmüller [128] or our experience in the bachelor thesis of Marian Rockenhäuser [129]).

Probing the atomic cloud as well as preparation itself requires rapid manipulation of laser fields, magnetic and electric fields, and switching other electronic components. For these purposes we use a computed aided control system "Adwin II pro" by *Jäger Messtechnik*, which allows to generate both TTL and analog

signals with a time resolution of $20\ \mu\text{s}$, and a FPGA based pulse generator by *Swabian Instruments* with a time resolution of $2\ \text{ns}$.

3.3 Single Photon Imaging with EMCCD Camera

In this part we will discuss the side project of implementing a single photon imaging with EMCCD camera. The developed technique finally was not used in the experiments with Rydberg atoms during the working time period of the author. But being a very promising tool for getting more insights into the physics in the field of Rydberg quantum optics, the author hopes that it will be successfully introduced into the experiment in the new version of the apparatus, currently built in Denmark.

3.3.1 Motivation for a single photon imaging with Rydberg atoms

One of the very interesting directions in the field of Rydberg quantum optics is pushing a system into the regime, where one could observe the many-body phenomena with interacting polaritons [11]. There are different approaches in this field, but, for example, one particular way to reach this regime is to prepare a system with many weakly interacting polaritons. Polaritons in such a regime will propagate through a three dimensional system, thus, they will also experience Rydberg interaction in the transverse direction. This interaction can distort incoming beam with a Gaussian profile due to excitation of higher-order spatial modes [50]. Therefore, it is very interesting to study the effect of Rydberg-nonlinearity in the mean-field regime on the beam shape. Here one could expect observation of formation of spatial solitons, when diffraction is balanced by the nonlinearity. Another interesting topic is to study the anisotropy of Rydberg-Rydberg interaction by looking into the transversal modes of propagating polaritons [130, 47]. On the other hand, exploring the regime with only few strongly interacting polaritons propagating through the cloud could allow to study transverse nonlinear effects at the lowest light levels and extract photon number fluctuations in transversely structured beams. In this case the interesting transition to quantum solitons made up by a discrete number of photons can be investigated [131, 132].

To carry out such a research, it would be necessary to perform a spatial imaging of the probe light beam transmitted through the cloud. Due to the low light levels involved in such an experiment, using a normal CCD cameras is not possible because of the high dark noise rate produced on the chip. A way to overcome this limitation is to use an EMCCD camera (electron multiplying charge-coupled device), which is capable of detecting single photons on each individual pixel (see Fig. 3.8(a) for a schematic). In particular such an imaging strategy was used in the experiments on spatial correlations of photon pairs emitted from a spontaneous parametric down-conversion source [133], or in the astrophysics experiments [134].

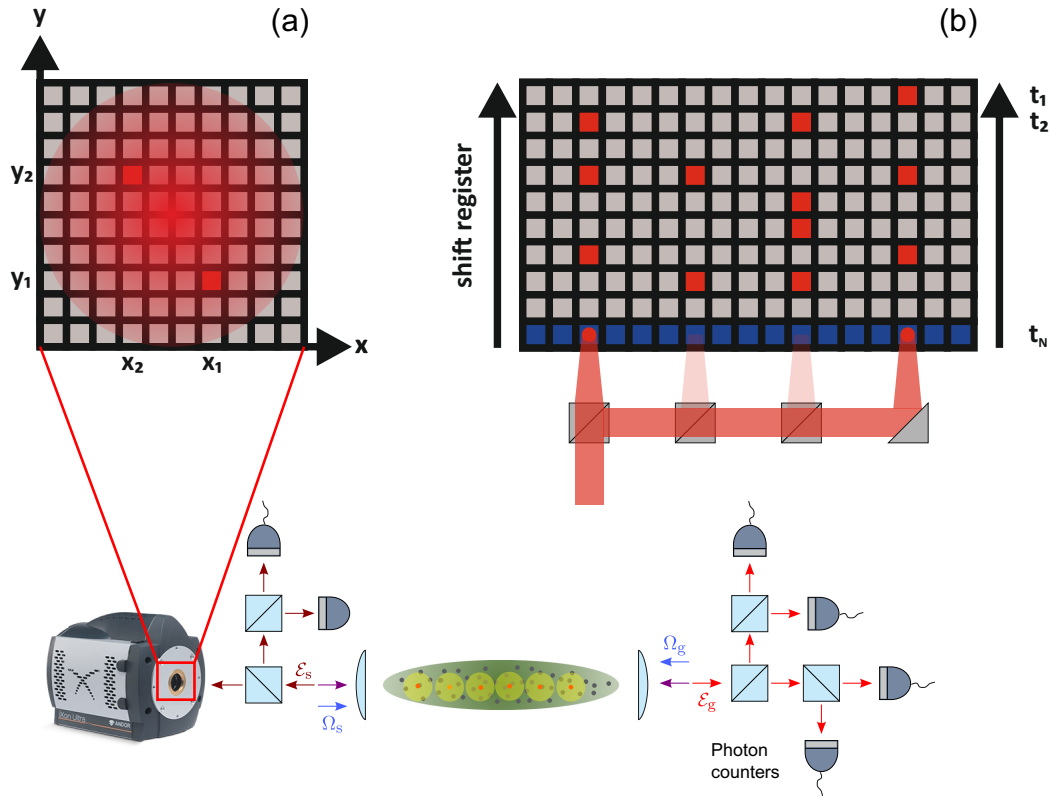


FIGURE 3.8: A schematic for using an EMCCD camera Andor iXon Ultra 897 in the Rydberg experiment: (a) measuring the spatial beam profile applying photon recovery; (b) measuring temporal correlation functions. For measuring temporal correlations, the beam is split into several beams and all of them are focused onto the individual pixels in a single row. After an acquisition time the exposed row is shifted up (away from the beams) therefore exposing a new clean row for a next acquisition step. The procedure is limited by the amount of rows on the chip.

As well, there is another prospect for application of an EMCCD camera in the field. Conversion polaritons into photons allows to easily measure temporal correlations between transmitted photons. Measurement of high-order temporal correlation functions is one of the main methods in understanding physics of a many-body system. For higher photon numbers it becomes bulky and expensive to use single photon counting modules (SPCM) for measuring temporal correlation functions. As a promising alternative one could think about is using an EMCCD camera in a single photon counting mode to replace multiple SPCMs by considering every individual pixel as an individual photon counting module (see Fig. 3.8(b)). For example, such an approach could allow measuring all orders of photon correlations in the system with around 10 polaritons. The time resolution with modern EMCCD cameras could be on the order of tens of nanoseconds, therefore allowing to measure polaritons correlations with typical decay time on the order of microseconds.

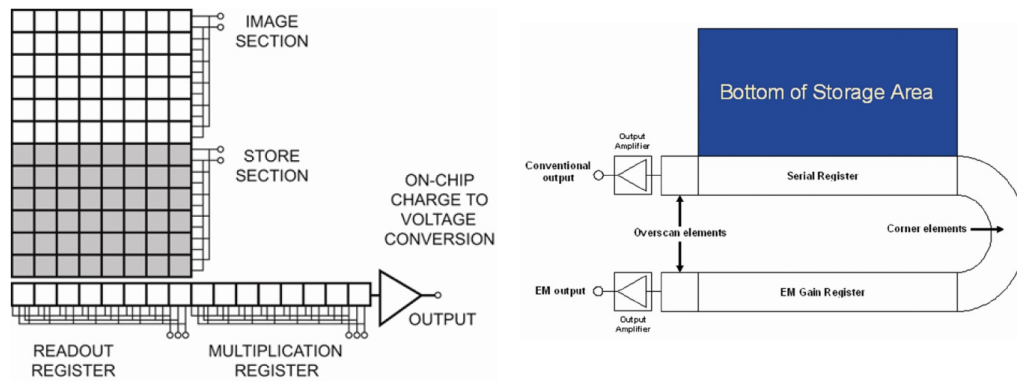


FIGURE 3.9: The structure of the chip in Andor iXon Ultra 897 [135]. The chip consists of two parts with the size of 512×512 pixels: the image section is used for image acquisition, and the storage section is used for image storage to accelerate the process of readout. The readout register is used for readout either to a conventional output or to EM gain output where the amplification takes place. With a special holder designed in our group, the chip positioned such that in the frontal look the storage area is to the right from the image area.

3.3.2 EMCCD camera Andor iXon Ultra 897

For our work we have chosen Andor iXon Ultra 897 EMCCD camera. This camera possesses back-illuminated 512×512 frame transfer sensor with a single pixel size of $16 \times 16 \mu\text{m}$ and overlocks readout up to 17 MHz (56 fps for a full frame). In the same time it can maintain single photon sensitivity, while being stable. The chip can be cooled down to -100°C . The readout noise, that appears when the charge of the detected photoelectrons is converted to an output voltage, can be maintained on the level of $< 1e^-$ with EM gain applied (while for conventional low light level CCDs the readout noise has a standard deviation of 2.5 electrons at best at kHz readout rates and goes up to 10-100 for MHz readout rates). The quantum efficiency of the chip for 780 nm is around 80%.

The structure of the chip is shown in Fig. 3.9, where one can see a pair of matrices of pixels stuck together: an image section and a storage section. An image section is a part of a chip that is open for illumination, while a storage section is a part that is masked with a metal plate, which protects it from the light. During the acquisition the image area is exposed to light which is stored in the form of electronic charge in every pixel. On the command the whole image can be shifted to the storage section. To read out the sensor, charge is moved vertically into the readout register, after which it can be moved horizontally to the output amplifier for a conventional output, or to multiplication (gain) register. The work of multiplication register is based on the process known as "impact ionization": while moving a charge through a register there is tiny but finite probability that this charge will produce another electron-hole pair in the conduction band, which results in the amplification of the signal. There are two main ingredients in any EMCCD camera that allow to stimulate the process of impact ionization: to increase the initial energy of a moving charge

a large electric field is applied in the direction of the move resulting in increase of the probability of impact ionization. At second, there are hundreds of cells in which impact ionization can occur: though the probability of amplification in a single pixel is only around $\times 1.01$ or $\times 1.015$, the gains of up to thousands can be achieved over the entire length of the EM register.

We continue overview with highlighting the most important features of the camera for a practical use in the quantum optics experiment.

The one opportunity to control the camera is to use Andor SOLIS software provided by Andor. This software provides an access to most of the camera functionality, but unfortunately it contains serious drawbacks which could become a problem in the real experiment (see examples below). In the SOLIS environment one can write simple scripts using Andor Basic programming language. For example, a continuous non-stop operation of the camera is not possible without running the simple script *"while(1) run end"*, which puts the camera in the running mode where it waits for triggers to come for the infinite time. Another option is to use Andor SDK and write your own software - it is a way that allows to push to the limits of the device.

There is a bunch of important parameters, that is necessary to preset before starting acquisition (for more theoretical details see [135, 136]):

- Choosing between conventional amplifier (for bright signals) and EM amplifier (for a single photon operation)
- The value of EM gain from 1 to 1000. The higher the value the more sensitive the device.
- Pre-amplifier gain: it was found that working with "Gain 3" (amplification factor of 4.92 from count to electrons), recommended by Andor, produces the best results for a single photon imaging.
- Vertical clock speed defines the speed of a charge transfer in the vertical direction in μs . The rule is the lower the speed the lower the noise. But for a real application it is necessary to set the fastest speed of $0.5 \mu s$ which produces good results.
- Vertical clock amplitude basically defines the voltage applied for the transfer of the charge in vertical direction. This parameter might allow to speed up the process of charge transfer or correct for some distortions due to saturation, but in the same time it increases the spurious charge in the pixels and can produce some noise patterns. Working with the "Normal" value was found to be optimal for most cases.
- Horizontal readout speed has to be set to 17 MHz to achieve a fast operation of the camera.

The most useful mode of operation was found to be a "Fast Kinetics" mode which allows to work with exposure times on a microsecond timescale. In this mode it is possible to crop the part of the chip that will be used for image acquisition, while the rest of the chip is used for storage of the image before the readout. Of course, one should ensure that the light does not fall on the storage

part, which is possible to achieve either with the OptoMask sold by Andor, that allows to select any rectangular area of the chip, or by mechanically masking (gluing a piece of metal on) the part of the image section that will be used for the storage of the signal. The vertical transfer speed is applied to a single row of pixel, so a row 1×512 can reach a frame rate of 11074 fps (according to specs). It is also possible to shrink the illuminated area in the second direction which would not improve the frame rate, but can help to decrease the amount of produced data.

In this regime one can use an "External Trigger" or "Fast External Trigger" to trigger an acquisition event. Every trigger pulse would trigger an acquisition event with a preset exposure time. After filling the full chip with the signal data one has to read it out and this process takes significant amount of time. Therefore, before the readout one can run only a particular amount of acquisition events, which is defined by the number of rows one uses for acquiring an image and would be a ratio between total amount of rows (equal to 1024) and amount of rows from defined imaging area. It is important to mention that once the camera is started and waits for a trigger event, a process called "keep clean" is running in the background. The aim of this process is to clean the pixels of the chip from the spurious charge formed during the waiting period. In the "External Trigger" regime there would be a delay between the trigger pulse and the start of acquisition while for the "Fast External Trigger" regime Andor claims to interrupt the cleaning process and immediately start the acquisition process. However, in practice, it was found that working with Andor SOLIS software (to operate the camera) and using Andor Basic programming language there is still some delay time in the range $0 \dots 20 \mu\text{s}$ between the triggering pulse and the acquisition start. The origin of this delay is not completely clear, but probably originates from the single clean cycle that the device still has to finish or interrupt. In the Andor manual [135] one could find an allusion on user settable delay between the trigger pulse and the acquisition, but this option is not available in SOLIS software. It is possible that only using Andor SDK for programming the camera operation would allow to access this option.

Another limitation connected with using Andor SOLIS software and Andor Basic programming language is a limitation on the frame rate of the camera. Basically it was possible to set the delay time between two consequent readout events only to the value that is an order of magnitude higher than the value predicted by the hardware (see an example below). Again, this restriction was found to be connected with Andor SOLIS and Andor Basic, and could be avoided by using Andor SDK for a camera operation.

As an example, that will be used later for the test of the camera, we chose an area with the size of 51×512 pixels. Exposure time is set to $200 \mu\text{s}$, the horizontal readout speed to 17 MHz and vertical shift speed to $0.5 \mu\text{s}$. It means that before reading out we can accumulate $1024/51 \rightarrow 20$ images stored on the chip. We run the camera in the non-stop regime, where it waits for a trigger signal. The acquisition of 20 images is done by sending 20 trigger pulses with length of $200 \mu\text{s}$, with the delay between them of $400 \mu\text{s}$ (however, the length of the trigger pulse does not matter in Fast External Trigger regime, because the acquisition time is preset and measured by the camera clock). The minimum delay between

two acquisition events should be solely limited by the time necessary to transfer 51 rows vertically and in our case is $0.5 \times 51 = 25.5 \mu\text{s}$, what is confirmed experimentally. After the acquisition of the 20 images the camera must read the image out, which would take the time on shifting 1024 rows vertically and reading out 512×1024 pixels horizontally: $0.5 \times 10^{-6} \times 1024 + (1/17 \times 10^{-6}) \times 512 \times 1024 = 32 \text{ ms}$. Therefore, one would have to wait minimum 32 ms before being able to take another 20 images. However, as it was discussed above, Andor SOLIS and Andor Basic require more time for processing the readout, and this time was limited by 400 ms.

Finally, it is important to note what quantity is obtained after the image acquisition, multiplication and processing the electron signal. First of all, the photons hitting the chip are converted into the photoelectrons with the quantum efficiency of the chip at desired wavelength. Then this electronic signal passes through the EM register and experiences a mean gain g (set by the user) resulting in signal electrons. This signal electrons have to be converted into a voltage which is then digitized by an Analogue to Digital Converter (ADC). Each Analogue to Digital Unit (ADU) is presented as a ‘count’ in the signal intensity scale, with each count (or gray level) corresponding to an exact number of electrons [136]. For the "Gain 3" amplification, 1 count consists of 4.92 electrons on average. Furthermore, the signal value in counts will sit on top of an electronic bias offset value, which is around 480 counts (gray levels) for our camera.

3.3.3 A brief theory of an EMCCD operation

When n photoelectrons are fed into the multiplication register the output signal cannot be precisely described, because multiplication process is a statistical process. Therefore, a random output of x electrons can be described by a conditional probability to obtain x electrons with an input of n photoelectrons [137, 138]:

$$p(x|n) = \frac{x^{n-1} \exp(-x/g)}{g^n (n-1)!} \quad (3.10)$$

with g being the mean gain and $g = (1 + p_c)^m$, where p_c is the probability that a single electron produces another electron in the multiplication register and m is the number of cells in the multiplication register.

The conditional probability $p(x|n)$ is depicted in Fig. 3.10, from which one can see that the inverse problem of finding amount of photoelectrons n from the amount of produced electrons x after the multiplication does not have an unique solution [138]. There is one exception to this: if the light levels in the system are very small, such that on average there is much less than 1 photon falling on each pixel, producing much less than 1 photo electron in each pixel, then we can say that we have either 1 or 0 photon on each pixel. If enough gain is applied, the output of each photon will be a positive peak of a random amplitude, while the output would be zero for zero input photons. This regime is called a photon counting regime and it allows counting photons only in the case when we are sure that the light fluxes are small enough. Such an ideal situation can be extended to the case when we have fluxes with more than 1 photon falling on

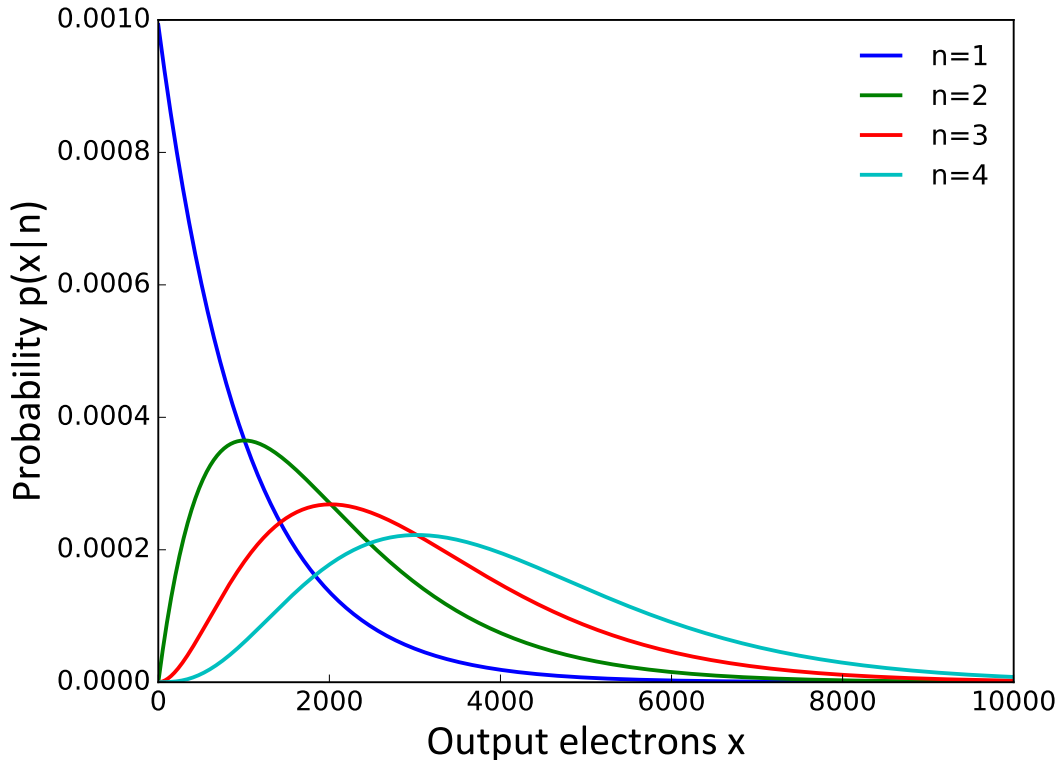


FIGURE 3.10: EMCCD output probabilities for a different number of input photons and a mean gain of 1000.

each pixel on average. In this case, one can divide the acquisition time t_{acq} on equal amount of intervals N and acquire N images with t_{acq}/N acquisition time instead of a single image with t_{acq} . This allows to reduce the amount of photons hitting each pixel during the single exposure period to be well below 1 photon per pixel. Applying, in addition, different statistical tricks like using Bayesian estimator, allows to effectively retrieve the initial amount of photons hitting the chip. This method of exposure time division is well described in the work of Lantz et al. [138], but is not relevant for our work due to intrinsically low fluxes in our experiment, therefore it will not be discussed here.

The described above approach for working with low light fluxes would work well only in the case when there is no noise in the system. Unfortunately, in the reality there are several noise sources which result in the output of the multiplication register to be non-zero even in the absence of photons. The most important sources of noise are [137, 138]:

- Read out noise that appears as additional noise coming from the on-chip output amplifier, where the charge of the detected photoelectrons is converted into an output voltage. It is well described by a Gaussian probability with a zero mean and a standard deviation σ_{read} . At high readout rates (such as 17 MHz used in our tests) the standard deviation can achieve levels of 10-100 electrons per readout.
- Clock induced charge (CIC) and dark noise. According to the specifications of the Andor camera dark noise is negligible for short exposure

times. However, during the parallel transfer of the charge along the chip there is a probability p_{par} to create a spurious charge that will enter the multiplication register when reading a given pixel. Then probability to generate x_{par} electrons at the output is given by

$$p(x_{\text{par}}) = p_{\text{par}}p(x_{\text{par}}|1) = \frac{p_{\text{par}} \exp(-x_{\text{par}}/g)}{g} \quad (3.11)$$

- There is a small probability p_{ser} that a spurious electron is generated inside of the multiplication register, resulting in the output:

$$p(x_{\text{ser}}) = \sum_{i=1}^m \frac{p_{\text{ser}} \exp(-x_{\text{ser}}/p_c^{m-i})}{p_c^{m-i}} \quad (3.12)$$

Here it is very important to note that Eq. 3.11 and Eq. 3.12 are not valid for $x = 0$, which corresponds to the biggest probability. Therefore, $p(x_{\text{par}})$ can be obtained just as $1 - p(x_{\text{par}} > 0)$, which should be done once the sufficiently high value of x is reached. The same is applied to $p(x_{\text{ser}})$.

To find the full noise statistics $p(x|0)$ it is necessary to perform the convolution of three noise probability curves. During this procedure one should take into account the electronic offset of the camera (around 480 gray levels for our camera) and conversion factor from gray levels to electrons (1 gray level corresponds to 4.92 electrons for our measurements), both discussed above. The subtraction of the bias level results in the negative values of electrons x , because the readout noise distribution is centered in zero.

We have studied the noise characteristics of our camera by collecting images in the darkness (with the closed camera lid and shutter); the parameters of these measurements were: 100 μs exposure time, 17 MHz readout rate, 0.5 μs vertical clock speed, vertical clock amplitude is set to "Normal" and pre-amplifier gain is at "Gain 3". The chip temperature is kept at -100°C . We analyze the obtained images by plotting the histogram of gray levels and then fitting the theoretical probability law to this histogram (see Fig. 3.11). We see that, as it was discussed, the probability curve is a Gaussian centered on zero due to readout noise, followed by a long tail due CIC. The obtained fitting parameters are $\sigma_{\text{read}} = 95 e^-$, $p_{\text{par}} = 1.6 \times 10^{-3}$, $p_{\text{ser}} = 2.7 \times 10^{-5}$. These values are in a good agreement to the technical notes of the camera.

With this knowledge of the noise nature in an EMCCD detector we are coming back to the problem of photon counting. To avoid the false photon detection events one should try to reduce the impact of noise, the biggest source of which is coming from the readout of the electrons from the chip and reproduced as a peak in Fig. 3.11. To do this, one can apply a thresholding procedure, which implies that the detection of the photon is considered only in the case when the output is higher than some set threshold value T in gray levels, and when the output is lower, it is considered as an absence of a photon. In the literature the different values of threshold are proposed to fit different applications [137, 139, 138, 140, 141, 142], but in general we found that the threshold of around $3\sigma_{\text{read}}$ produces a decent result in the process of photon counting. As it is noted before, for our camera we measured $\sigma_{\text{read}} = 95 e^- = 95/4.92 \text{ gr.l.} = 19.3 \text{ gr.l.}$. In

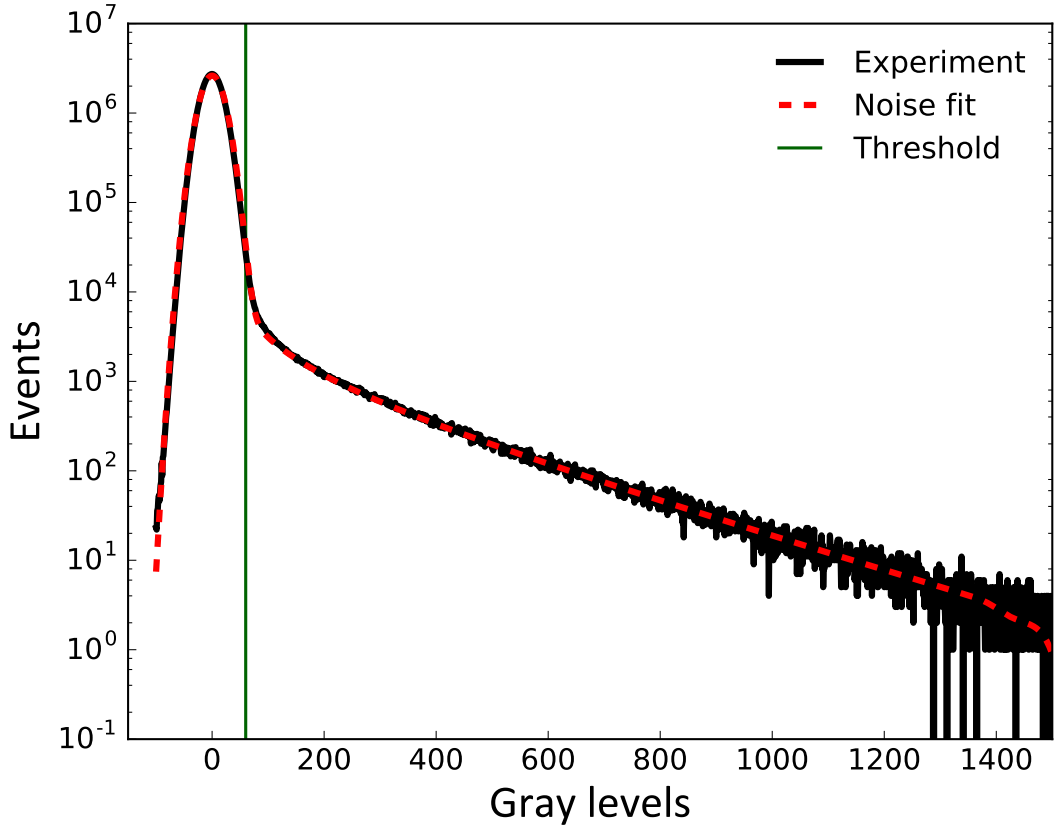


FIGURE 3.11: Histogram of the gray levels for a dark image in log scale: the measured data shown by the black line and the fit based on the model from the text is shown by dashed red line. The extracted fitting parameters are $\sigma_{\text{read}} = 82.6 e^-$, $p_{\text{par}} = 1.6 \times 10^{-3}$, $p_{\text{ser}} = 2.7 \times 10^{-5}$. Green line indicates the threshold of 60 gray levels.

Fig. 3.11 we mark a threshold corresponding to 60 gr.l. what is $3.1\sigma_{\text{read}}$. With a threshold T_0 the fraction of the signal that we would measure for the case of a single incident photon is

$$C_{\text{signal}} = \int_{T_0}^{\infty} p(x|n=1)dT = \int_{T_0}^{\infty} \frac{1}{g} e^{-x/g} = e^{-T_0/g} \quad (3.13)$$

For our case $T_0 = 60 \times 4.92 = 295.2 e^-$ which results in $C_{\text{signal}} = 0.74$. Therefore, we would loose 26% of the real signal by applying such a threshold. At the same time we can estimate how much noise we pick if we apply a threshold of 60 gray levels:

$$C_{\text{noise}} = \sum_{T_0=60}^{\infty} p(x|0) = 0.0044. \quad (3.14)$$

Thus, we pick only 0.44% of the noise produced on the chip during a readout event.

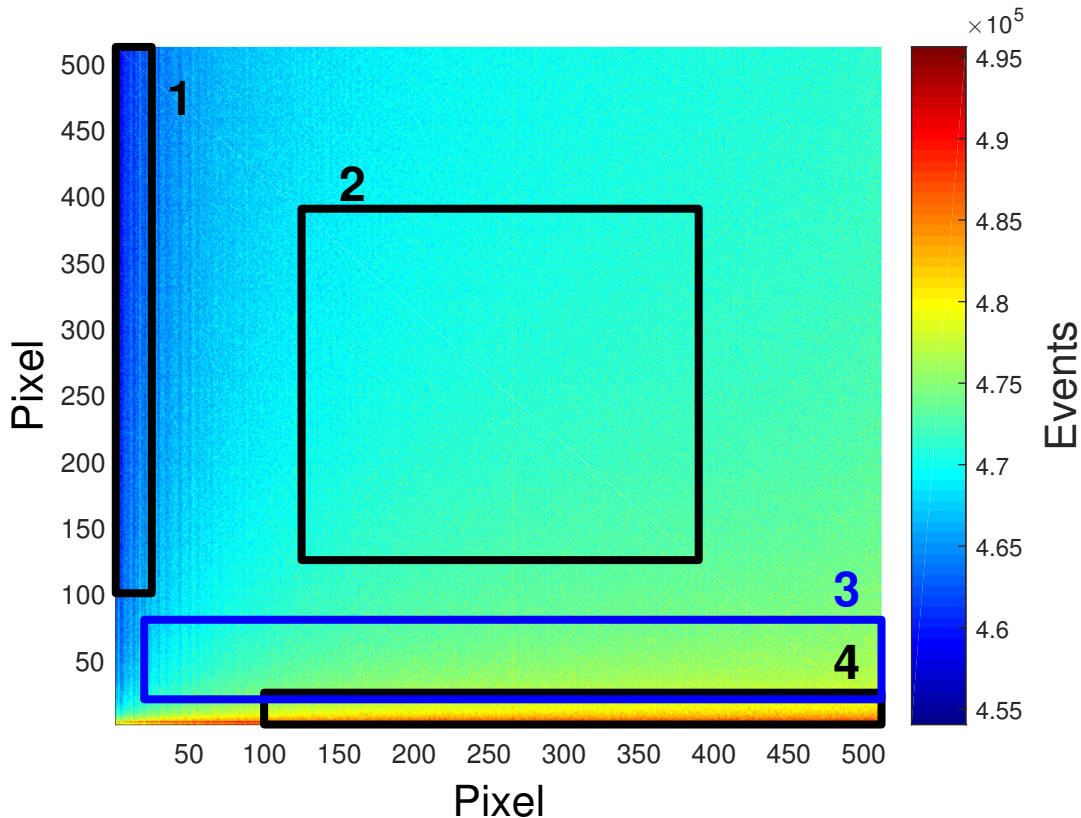


FIGURE 3.12: Dark image of the full chip. Rectangles indicated sections with different noise parameters.

3.3.4 Single photon imaging

Before starting the imaging of a light beam we have investigated dark images of our camera in a detail. One important peculiarity is non-uniform spatial distribution of the noise on the chip. This is depicted in Fig. 3.12: one can see that the noise has different gradients in different directions along the chip. We have extracted noise parameters for different sections of the chip that are presented in the Table 3.1. It is seen that the readout noise stays the same,

	σ_{read}	p_{par}	p_{ser}
Section 1	95	1.5×10^{-3}	1.6×10^{-5}
Section 2	92.4	1.6×10^{-3}	2.3×10^{-5}
Section 3	92.9	2.1×10^{-3}	2.4×10^{-5}
Section 4	94.3	3×10^{-3}	2.7×10^{-5}

TABLE 3.1: Fit parameters for noise at different spatial regions of the chip (see Fig. 3.12).

but noise coming from CIC and generating charges in multiplication register is growing. The nature of this behavior is not absolutely clear, but one sensible reason could be the stray electric fields that are coming from multiplication

register and create a spurious charge in the adjacent pixels. This register is positioned geometrically exactly below the section 4 which explains a higher noise rate there. As well, one could think about some memory effect if the chip is not fully flushed before the next operation. One way or the other, depending on the application, one should think what part of the chip is better to use for a measurement. Unfortunately, there are more local effects of the spatial noise that we will discuss below that restrict the usage much more.

To perform a test imaging we used a single mode fiber that was attached directly to the window of the camera to avoid a stray light. This allows to produce a good Gaussian beam that we want to image photon by photon. The beam was focused such that it fits in 51 rows of pixels on top of the chip. The laser light was controlled with AOM and FPGA based pulse generator which allowed to send pulses of desired duration. The camera was set up into "Fast Kinetics" mode with subarea height of 51 rows and number of series of 20 images (meaning that in 20 images two chips are filled completely and we have to read the data out). The exposure time was set in the software to 100 μs similar to a laser pulse duration. The camera was set in "External trigger" mode, therefore, in parallel to light pulses, trigger pulses were sent to the camera, which triggered the acquisition and shift of the registers. In addition to this, there is a second path of light coupled to a single photon counting module (SPCM) for the calibration purposes to get the absolute value of the input photons. SPCM is triggered in parallel to the camera. As it was discussed above, the waiting time between consequent readout events was 400 ms. To sum up, we send 20 light pulses to the camera of 200 μs duration time and 400 μs in between them; to measure them we trigger 20 exposure events of the camera, which completely fills the chip. After this we have to wait for 400 ms for readout before sending another train of pulses. Usually, we accumulate a few tens of thousands of images.

The results of such a measurement, where we send on average $\langle n_{\text{image}} \rangle = 3.5$ photons per laser pulse and exposure event (which result only in $\langle n_{\text{pix}} \rangle = 1.3 \times 10^{-3}$ photons per pixel per exposure event) could be seen in Fig. 3.13. A single image as a result of a single exposure event (Fig. 3.13(a)) represents only a random distribution of spikes in different pixels, most of which are noise. If we sum up 20000 images (Fig. 3.13(b)) the resulting image is distorted by the noise such that it is not really possible to distinguish a Gaussian mode of the laser light. Applying a thresholding procedure with a threshold of $T_0 = 60$ gr.l. (Fig. 3.13(c)) leads to a nicely distinguished Gaussian mode. Note, that this thresholding sets the fidelity of detecting a single photon to 74%. To restore the average amount of photons hitting a single image, one can count the signal from every pixel in the imaging area and divide by the quantum efficiency of the chip of 80%. We found it to be 2.5 photons for the case of $T_0 = 60$. Correcting it with the fidelity of a single photon detection gives $\langle n_{\text{image}} \rangle = 2.5/0.74 = 3.4$ photons. For comparison Fig. 3.13(d) represents the restored image with $T_0 = 200$. In general it might help to eliminate some part of the noise but it would require to accumulate more data. In this case the fidelity of detecting a single photon is 37% and retrieving the full amount of photons provides $\langle n_{\text{image}} \rangle = 1.3/0.37 = 3.5$ which in excellent agreement with

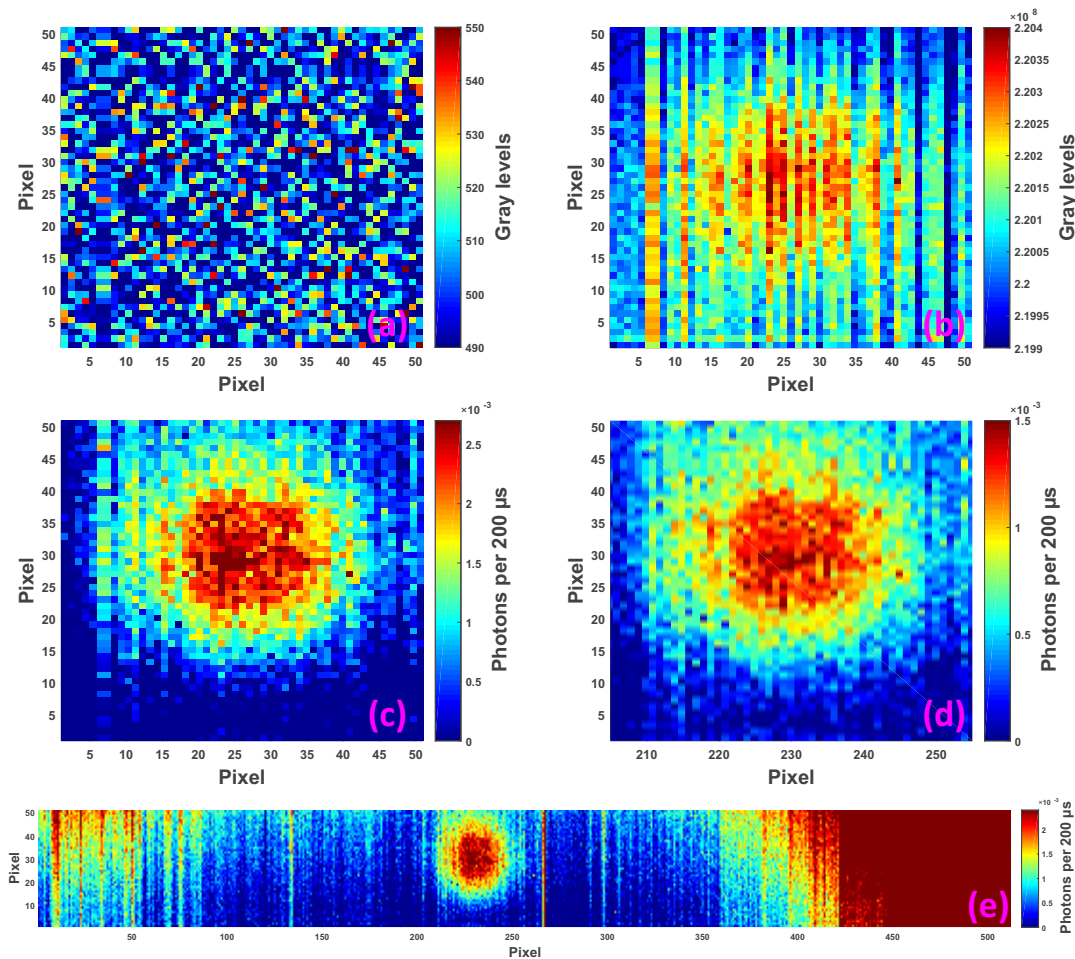


FIGURE 3.13: Imaging of a Gaussian beam with an EMCCD camera sending $\langle n_{\text{image}} \rangle = 3.5$ photons per image or $\langle n_{\text{pix}} \rangle = 1.3 \times 10^{-3}$ photons per pixel on average. (a) A single image of a single shot; (b) A sum of 20000 single shot images; (c) A restored image with $T_0 = 60$ gr.l.; (d) A restored image with $T_0 = 200$ gr.l.

the values obtained from SPCM and thresholding with $T_0 = 60$.

The one important drawback of the measurement with our camera turned out to be a spatial noise on the region of 51×512 pixels that we used for the measurement. In Fig. 3.13(e), the full imaging region is shown after applying thresholding with $T_0 = 60$. It is clearly seen that on the right side of the region the noise signal is way higher than the light signal, making it not possible to use it for real measurements. As well, a pattern of different stripes can be observed anywhere on the chip. For example, on the right from the beam, at pixel 265, there is a prominent stripe of noise that clearly distorts the beam if it is positioned such that it overlaps with the stripe. These distortions are shown in Fig. 3.14. The bright stripe is clearly seen and cannot be eliminated by cranking up the threshold value. Even more, there are some other stripe artifacts that also survive during thresholding. Finally, it is clearly seen that the position of the beam on particular part of the chip is very important. One has to choose it such that noise pattern can be avoided; and usually it is not really possible to get rid of the noise patterns just by changing the threshold

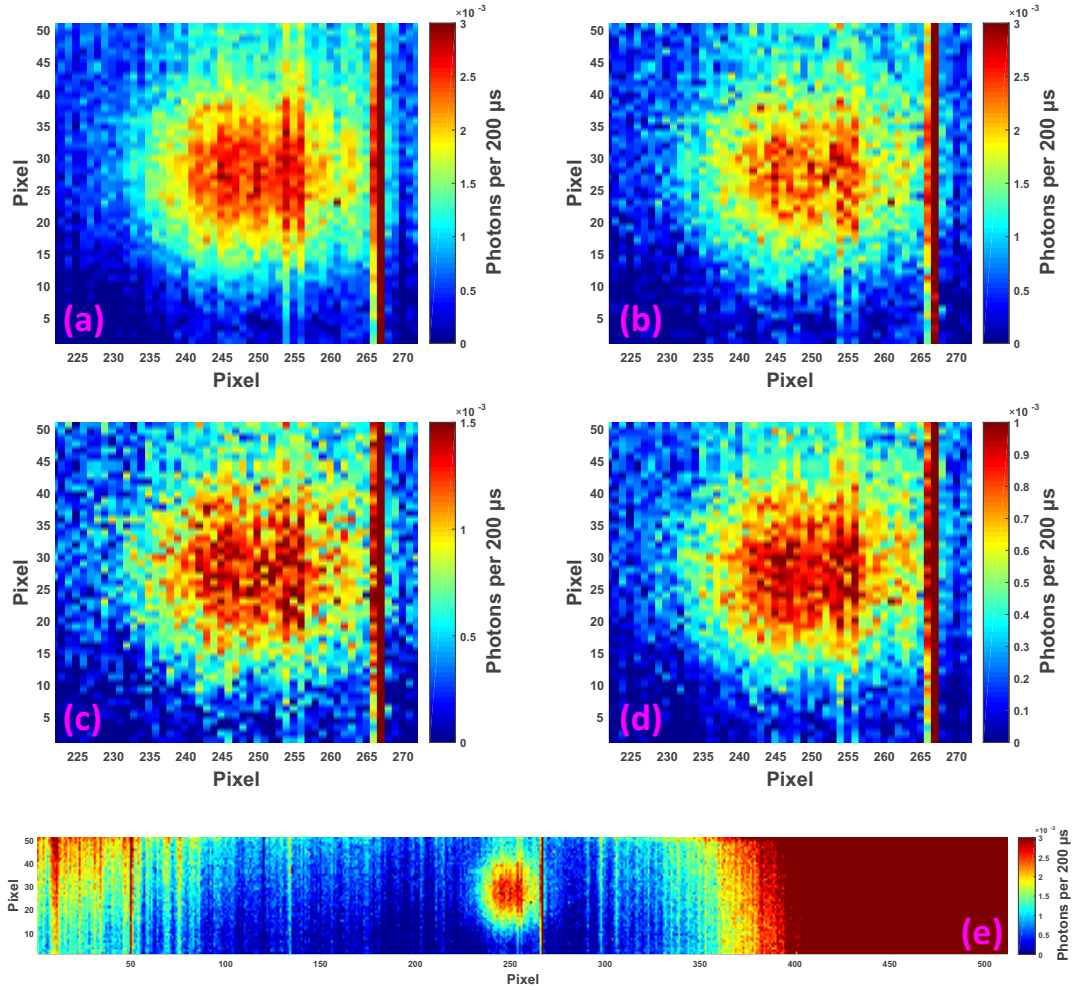


FIGURE 3.14: Imaging of a Gaussian beam with an EMCCD camera. The beam position is changed compare to Fig. 3.13. Different threshold was applied to observe it's effect on the noise patterns: (a) $T_0 = 60$, (b) $T_0 = 100$, (c) $T_0 = 200$ and (d) $T_0 = 300$. On the picture (e) the full scale image after thresholding with $T_0 = 60$ is depicted.

values.

3.3.5 Outlook

In the end of the chapter, it is necessary to say that EMCCD camera has a potential to become a very powerful tool in the experiments on Rydberg quantum optics. But one has to be careful in choosing the right way of setting it up. Especially, it is important to avoid noise patterns that appear on the chip. Another important thing, one has to take care about during the integration of the camera into the experiment, is avoiding stray light. In this sense, using a fiber in our test runs is easy because fiber can be directly connected to the window of the camera what protects the chip from other background light. However, in the experiment one cannot use a fiber to guide a light to the camera because it would completely change the mode of light that hits the fiber. Therefore, integration has to be implemented in free space which can

become a separate topic for investigation. We tested few laserline filters and found out that they also distort the mode of the light, but careful investigation of them possibly can be used for reconstruction of the real light mode afterwards. Otherwise, the new ideas are necessary on how to avoid the stray lights hitting the chip of the camera in the system.

Chapter 4

Electromagnetically induced transparency of ultralong-range Rydberg molecules

We study the impact of Rydberg molecule formation on the storage and retrieval of Rydberg polaritons in an ultracold atomic medium. We observe coherent revivals appearing in the storage and retrieval efficiency of stored photons that originate from simultaneous excitation of Rydberg atoms and Rydberg molecules in the system with subsequent interference between the possible storage paths. We show that over a large range of principal quantum numbers the observed results can be described by a two-state model including only the atomic Rydberg state and the Rydberg dimer molecule state. At higher principal quantum numbers the influence of polyatomic molecules becomes relevant and the dynamics of the system undergoes a transition from coherent evolution of a few-state system to an effective dephasing into a continuum of molecular states.

4.1 Introduction

Mapping the long-range interaction between Rydberg atoms [57] onto slowly traveling polaritons via electromagnetically induced transparency (EIT) [85] has emerged as a promising approach to realize effective photon-photon interaction in an optical medium [143, 144, 28, 27, 145]. Fast development over the last years in this novel field of Rydberg quantum optics [97] has enabled new tools for quantum information as well as for exploring dynamics of correlated quantum many-body systems [11], including efficient single-photon generation [29, 30], creation of entanglement between light and atomic excitations [31], realization of attractive forces between single photons [40], demonstration of single-photon all-optical switches [32] and transistors [33, 34, 35], single-photon absorbers [36] and interaction induced photon phase shifts [37, 38, 39]. Future prospects include the crystallization of photons [43, 42] and the observation of three-body interaction between photons [45, 46].

The critical figure of merit for most of the above work is the optical depth (OD) per blockade volume [27]. Improving this quantity requires increasing the atomic density of the medium, but this inevitably brings the system into the regime where formation of ultralong-range Rydberg molecules [52, 146] has

to be taken into account to describe the Rydberg-polariton dynamics. The experimental study of these exotic molecules has evolved into a highly active field in itself, with a variety of exciting phenomena having been explored so far, such as states bound by quantum reflection [147], coherent creation and breaking of the molecular bond [148], polyatomic Rydberg molecules [102], trilobite [149, 150] and butterfly [151] states, and controlled hybridization of the molecular bond [152]. Diatomic Rydberg molecules have been realized for S -states in Rb [146], Cs [153] and Sr [154], for D -states in Rb [155, 156] and for P -states in Rb [157] and Cs [158]. Furthermore, Rb_2 Rydberg molecules have been used as a probe of the quantum phase transition from the superfluid to the Mott-insulator phase [159] and the existence of Rydberg molecules bound by mixed singlet-triplet scattering [155] has been proven experimentally for Cs [158] and Rb [160, 161].

In the context of Rydberg quantum optics, formation of Rydberg molecules has been suggested as a limiting factor on the coherence of slow and stored Rydberg polaritons [102]. Experimentally, Baur *et al.* found the dephasing rate of photons stored in Rydberg states with large principal quantum number ($n = 100$) to increase linearly with atomic density, restricting the overall performance of an all-optical switch [32].

Therefore, the aim of the present work is to investigate the regime of higher atomic densities in a more detail and try to find out how the formation of Rydberg molecules affects the coherence of Rydberg polaritons. As well, we explore how strict the limitation of molecule formation for the performance of an all-optical switch and transistor, and if there are ways to boost their performance.

4.2 Experimental scheme

A schematic of our experiment is shown in Fig. 4.1. We prepare 9×10^4 ^{87}Rb atoms, pumped into the $|g\rangle = |5S_{1/2}, F = 2, m_F = 2\rangle$ state, trapped in a crossed optical dipole trap. The $1/e$ radial and axial radii of the cigar shaped cloud at the temperature of $4 \mu\text{K}$ are $\sigma_R = 13 \mu\text{m}$ and $\sigma_L = 42 \mu\text{m}$. A weak 780 nm probe field, which couples $|g\rangle$ to the intermediate state $|e\rangle = |5P_{3/2}, F = 3, m_F = 3\rangle$, is focused into the center of the cloud ($w_{0,\text{probe}} = 6.4 \mu\text{m}$). We measure OD = 24 on the $|g\rangle \rightarrow |e\rangle$ transition over the full cloud length. For coupling the probe photons to a Rydberg state $|r\rangle = |nS_{1/2}, m_J = 1/2\rangle$ we add a strong 480 nm counterpropagating control field ($w_{0,\text{control}} = 14 \mu\text{m}$). Because of selection rules, our scheme addresses only the $F = 2$ hyperfine level of the Rydberg state [162]. All experiments are performed in the presence of a magnetic field of $B = 1 \text{ G}$ along the probe beam direction. To measure Rydberg excitation spectra we detune both probe and control fields by $\Delta = 2\pi \times 100 \text{ MHz}$ from the intermediate state and then scan the two-photon detuning over the $|g\rangle$ to $|r\rangle$ two-photon transition. After the excitation we field-ionize Rydberg atoms and collect ions on a microchannel plate detector (MCP). To perform storage and retrieval experiments, we employ the sequence shown in Fig. 4.1(c). First, we send a Gaussian probe pulse containing on average $N_{\text{in}} = 0.24$ photons into the

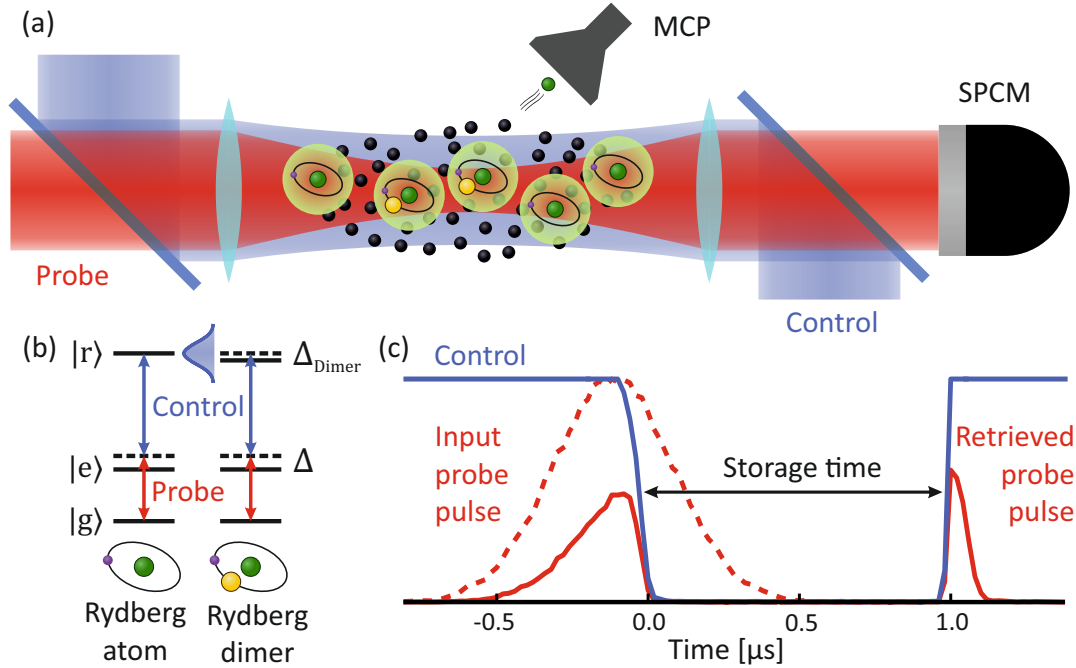


FIGURE 4.1: (a) Scheme of the experiment: a weak 780 nm probe field and a strong 480 nm control field are focused onto a cloud of ^{87}Rb , coupling the ground state $|g\rangle$ to an atomic Rydberg state (green atoms) and the slightly shifted Rydberg molecule state (green - yellow atom pairs). (b) Effective two-species level structure for the Rydberg state and the Rydberg dimer with binding energy of $-\hbar\Delta_{\text{Dimer}}$. If Δ_{Dimer} is smaller than the EIT linewidth both states are coupled simultaneously to the probe photons. (c) Pulse sequence for storage and retrieval of Rydberg polaritons showing control light (blue curve), input probe pulse (red dashed curve), and initially transmitted (solid red pulse on the left) and retrieved (solid red pulse on the right) probe photons.

cloud under resonant conditions ($\Delta = 0$) and ramp the intensity of the control field down to zero on a timescale of 120 ns while the probe pulse propagates through the cloud. As a result, part of the probe pulse is stored as a stopped Rydberg polariton in the cloud, which we read out after variable storage time t_s by turning on the control field again. The output pulse with N_{retr} photons is collected on a single-photon counting module (SPCM). We obtain the overall storage and retrieval efficiency of the process as $\eta = N_{\text{retr}}/N_{\text{in}}$.

4.3 Observation of coherent revival in storage and retrieval efficiency

We start our studies by investigating photon storage and Rydberg molecule formation over a range of principal quantum numbers between $n = 45 \dots 68$. Fig. 4.2 shows the observed storage and retrieval efficiency plotted versus storage time t_s for four different Rydberg states. We observe oscillations in the storage and retrieval efficiency for $61S$, $64S$ and $68S$ with frequencies of 511(3) kHz, 369(2) kHz and 241(2) kHz. To relate these oscillations to Rydberg dimers, we

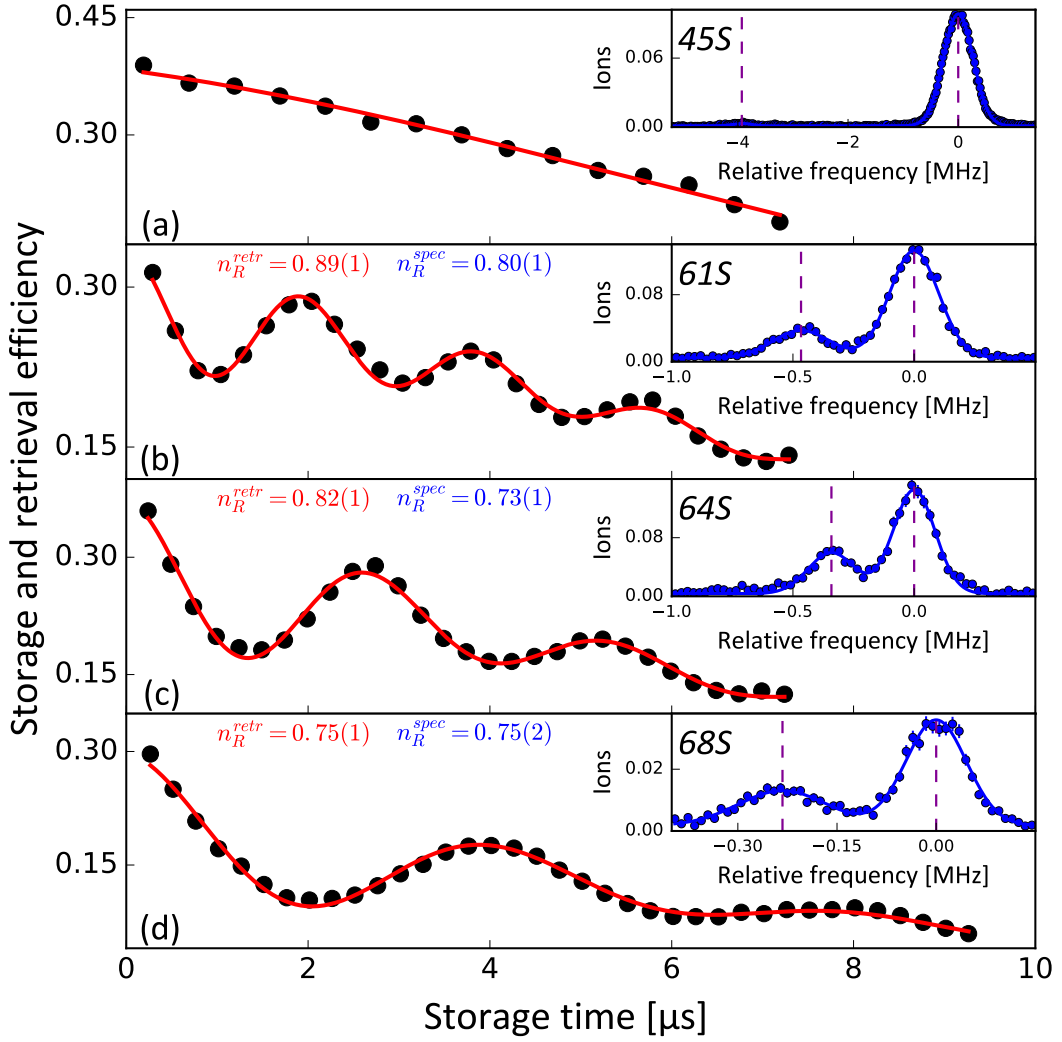


FIGURE 4.2: Storage and retrieval efficiency of stored photons versus storage time measured for different quantum numbers: (a) $45S$, (b) $61S$, (c) $64S$, (d) $68S$ (black dots). Corresponding Rydberg excitation spectra are shown as insets (blue dots). We fit the excitation spectra with a sum of two Gaussian lineshapes (blue solid line) and independently the retrieval curves with the model discussed in the text (red solid line). From both fits, we obtain the ratio of Rydberg atoms and dimers in the cloud, n_R^{retr} from the fit of retrieval curves and n_R^{spec} from the fit of molecular spectra. The purple vertical lines in the insets indicate the position of an atomic line and a dimer line, extracted from the fit. The errorbars for most data points are smaller than the shown markers.

show the excitation spectra in the corresponding insets in Fig. 4.2. Each spectrum consists of an atomic peak corresponding to excitation of Rydberg atoms, situated at the origin, and a clearly distinguishable dimer line red-detuned from the atomic line. The underlying mechanism for Rydberg molecule formation is the scattering of the slow Rydberg electron from a ground state atom [52]. In our case, the observed Rydberg dimers are well-described by pure s-wave

scattering [146], resulting in a molecular binding potential

$$V(\mathbf{R}) = \frac{2\pi\hbar^2 a}{m_e} |\Psi(\mathbf{R})|^2, \quad (4.1)$$

where $|\Psi(\mathbf{R})|^2$ is the local electron density and $a = -15.7a_0$ is the s-wave triplet scattering length for the electron - Rb atom collision [160]. Singlet-triplet mixing in the molecule formation does not occur in our case because of the spin-polarization of the atoms and selection rules [155, 163, 160]. The vibrational ground state wavefunction of the dimer is mainly localized in the outermost lobe of the Rydberg electron wavefunction, resulting in scaling of the dimer binding energy with principal quantum number $E_b \sim n^{-6}$ [146, 102]. The Rydberg electron can also capture multiple ground state atoms, forming polyatomic molecules with binding energy of a molecule with N ground state atoms $(N - 1)$ times larger than the binding energy of the dimer [102]. In our experiment the mean atomic density over the full cloud is $1.4 \times 10^{12} \text{ cm}^{-3}$, which is sufficient to form a significant fraction of Rydberg dimers, but only a negligible fraction of polyatomic Rydberg molecules for $n \leq 70$. We extract the Rydberg dimer binding energy $E_b = -\hbar \cdot \Delta_{\text{Dimer}}$ (in the following we will refer to Δ_{Dimer} as a binding energy in frequency units) by fitting a sum of two Gaussian lineshapes to the spectra, finding 470(35) kHz, 341(35) kHz and 240(15) kHz for 61S, 64S and 68S correspondingly, which are in good agreement with the measured retrieval oscillation frequencies. For $n = 45$, the dimer fraction is very small while the dimer binding energy $\Delta_{\text{Dimer}} = 3.93(4)$ MHz is larger than the Rydberg EIT linewidth, which we set to $\nu_{\text{EIT}} = 2\pi \times 2.5$ MHz FWHM for all datasets. As expected, in this case no oscillations in storage and retrieval efficiency are observed (Fig. 4.2(a)).

4.4 The model of two species EIT

To quantitatively reproduce the measured retrieval curves we employ a simple two-species model for the stored Rydberg polaritons. We consider our atomic cloud to consist of N_R Rydberg atoms, positioned such that they cannot form a Rydberg molecule, and N_D pairs of atoms, positioned such that they can form a Rydberg dimer. For Rydberg states where the dimer binding energy is smaller than the EIT linewidth ν_{EIT} , each photon is stored in a superposition of collective Rydberg atom and dimer excitations. The wave function of the stored polariton then evolves in time as

$$|\Psi(t)\rangle = \frac{1}{\sqrt{N_{\text{exc}}}} \left(\sum_{j=1}^{N_R} |R_j\rangle + \sum_{j=1}^{N_D} e^{-i2\pi\Delta_{\text{Dimer}}t} |D_j\rangle \right). \quad (4.2)$$

Here, $N_{\text{exc}} = N_R + N_D$, $|R_j\rangle = |g_1, \dots, r_j, \dots, g_N\rangle$ is a collective state with atom j in Rydberg state $|r\rangle$ and all others in ground state $|g\rangle$, $|D_j\rangle = 1/\sqrt{2} (|g_1, \dots, (g_j, r_j), \dots, g_N\rangle + |g_1, \dots, (r_j, g_j), \dots, g_N\rangle)$ is the symmetrized dimer state with atom pair j forming a Rydberg molecule. After a storage time t_s the storage and retrieval efficiency is then proportional to the overlap of this wave

function with the original one at $t = 0$

$$\eta(t_s) = |\langle \Psi(0) | \Psi(t_s) \rangle|^2. \quad (4.3)$$

In addition to the coherent evolution, we take into account several dephasing mechanisms. First, the thermal atomic motion introduces an overall Gaussian decay of the storage and retrieval efficiency with time constant $\tau_T = (\Delta k v_s)^{-1}$, where Δk is the sum of the wavevectors of the EIT light fields and $v_s = \sqrt{kT/m}$ is the thermal speed of atoms (see Appendix A). Additionally, we take into account decoherence of both Rydberg atoms and Rydberg dimers with coherence times τ_R and τ_D respectively. Including these effects in Eq. 4.3, we write the time dependence of the storage and retrieval efficiency of a stored polariton as

$$\eta(t) = \eta_0 e^{-t^2/\tau_T^2} |n_R e^{-t/\tau_R} + n_D e^{-t/\tau_D} e^{-i2\pi\Delta_{\text{Dimer}}t}|^2, \quad (4.4)$$

where η_0 is the initial storage and retrieval efficiency which is determined experimentally; n_R and n_D are the fractions of Rydberg atoms and Rydberg dimers, normalized such that $n_R + n_D = 1$. The oscillations in the storage and retrieval efficiency emerge from Eq. 4.4 because of the interference between the polariton component stored in the atomic fraction with the one stored in the dimer fraction. We note that because we send on average $N_{\text{in}} = 0.24$ photons per experimental realization, we rarely store more than one photon and thus can neglect any interaction between stored polaritons [75, 29, 164].

4.5 Discussion

We use Eq. 4.4 to fit the experimental data in Fig. 4.2. We assume τ_R to be given by the Rydberg atom lifetime and therefore fix it to the calculated values 49 μs (45S), 104 μs (61S), 118 μs (64S) and 136 μs (68S). First, for the 45S state (Fig. 4.2(a)), we set $n_R = 1$, which leaves only the thermal dephasing as a free parameter for which we obtain $\tau_T = 11.8(3) \mu\text{s}$. The time dependence of the storage and retrieval efficiency, when we do not couple to molecular states, is thus well described by decay due to random thermal motion of atoms and Rydberg population decay.

Next, for the data shown in Fig. 4.2(b)-(d), we keep τ_T , τ_D , n_R and Δ_{Dimer} as free parameters. The resulting values for Δ_{Dimer} are in very good agreement with the values we get from the excitation spectra (see above). Lifetimes τ_T of thermal atomic motion extracted from the fits 10.0(2) μs (61S), 9.6(2) μs (64S) and 9.9(2) μs (68S), all of which are in very good agreement with the dephasing time inferred from the cloud temperature $T = 4 \mu\text{K}$ measured by absorption imaging, which suggests $\tau_T = 10 \mu\text{s}$. The parameters defining the contrast of the observed oscillations, are the fraction of Rydberg atoms n_R and the fraction of Rydberg dimers $n_D = 1 - n_R$. For our set of data, the fit yields a Rydberg fraction of 0.89(1) (61S), 0.82(1) (64S) and 0.75(1) (68S). When we compare these values to the ones obtained from the amplitudes of the Gaussian fits to atomic and molecular lines in the excitation spectra, 0.80(1) (61S), 0.73(1) (64S), 0.75(2) (68S), we observe discrepancies for the 61S and 64S states, exceeding

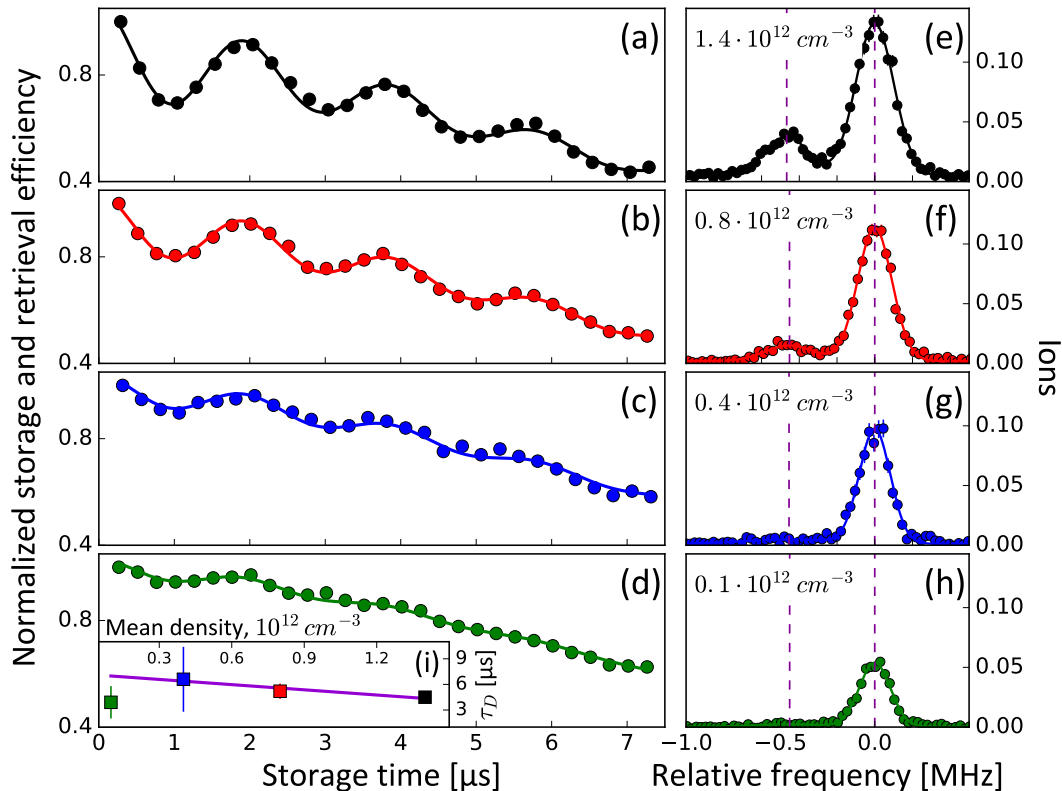


FIGURE 4.3: (a)-(d) Storage and retrieval efficiency of stored photons versus storage time measured for different densities (high to low) for the $61S$ state (dots). Solid lines are fits to the data using Eq. 4.4. (e)-(h) Corresponding excitation spectra from which the indicated mean atomic density for each data set is extracted. The contrast of the storage and retrieval efficiency oscillation decreases as expected when the amplitude of the dimer line becomes smaller. (i) Rydberg dimer coherence times for the different atomic densities extracted from the fits to the curves in (a)-(d).

one standard deviation. It is important to note that the result of the fit is very sensitive to the value of n_r and it is not possible to compensate an offset from the optimum value of n_r by adjusting other fit parameters. Instead, the observed disagreement in the parameters is explained by systematic drifts of the total atom number, which over the time required for the two measurements is on the order of 10% in our setup. For the shown datasets we can confirm these drifts by evaluating control measurements of optical depth taken throughout the full measurement sequence, which confirm the change in atom number between the spectra and retrieval data sets. Finally, we extract the Rydberg dimer coherence times $4.5(6) \mu\text{s}$ ($61S$), $4.3(4) \mu\text{s}$ ($64S$) and $4.7(3) \mu\text{s}$ ($68S$). These values are slightly larger than Rydberg dimer coherence times previously measured via Ramsey interferometry [165].

4.6 Density dependence of the observed coherent revival

We next turn to investigating the time dependence of the storage and retrieval efficiency for different atomic densities, which allows us to alter the Rydberg dimer fraction n_D . Fig. 4.3 shows the measured storage and retrieval efficiency curves at four atomic densities for the 61S state as well as the corresponding Rydberg excitation spectra. The measurements of the spectra were done at the same Rabi frequency and nothing except the atomic density in the atomic cloud was changed. The measurements of the retrieval curves were done in the way such that the delay time of the pulse passing through the atomic cloud stays constant for each measurement. The slight change in the EIT linewidth in this case does not affect the measurement because it is only important to keep the EIT linewidth higher than the dimer binding energy, which is true in our experiments for 61S state all the time. We extract the mean atomic density for each dataset from the position of the center of gravity of the excitation spectrum [102], obtaining $1.4 \times 10^{12} \text{ cm}^{-3}$, $0.8 \times 10^{12} \text{ cm}^{-3}$, $0.4 \times 10^{12} \text{ cm}^{-3}$ and $0.1 \times 10^{12} \text{ cm}^{-3}$ (Fig. 4.3(e)-(h)). Correspondingly, the Rydberg dimer fraction n_D shrinks with the density down to $n_D = 0.02$ for the lowest density. Therefore, as expected from Eq. 4.4, we observe a decreasing contrast in the storage and retrieval efficiency oscillations when lowering the density (Fig. 4.3(a)-(d)). More quantitatively, by fitting the data with the model, we extract the Rydberg atom fractions $n_R = 0.89(1), 0.94(1), 0.97(1), 0.98(1)$ for the four datasets, which are again in agreement with the ratios extracted from the excitation spectra within our experiment stability. In Fig. 4.3(i) we show the Rydberg dimer coherence times extracted from the fits for the different atomic densities. Omitting the result for the lowest density, where the dimer fraction is very small and the oscillations are barely visible, the remaining data points suggest a linear decrease of the coherence time as was found previously by Baur *et al.* [32]. Since our method does not differentiate between decay time T_1 and dephasing time T_2 , we cannot infer the dimer lifetime [165, 148]. The absence of scaling with principle quantum number and the linear scaling with density suggest that the dimer coherence time is limited by other factors, for example collisions between the atoms forming the dimer and other ground state atoms [166]. This mechanism would not scale with n , unlike e.g. scattering from the Rydberg electron, which should scale because the Rydberg orbit size increases with n .

4.7 Transition from coherent dynamics to an effective dephasing

Next, we investigate photon storage in a Rydberg state with larger principal quantum number, specifically 81S, to highlight the transition from coherent dynamics to effective dephasing observed previously at $n = 100$ [32]. For the 81S state the dimer lineshift is already smaller than the dimer linewidth, resulting in an asymmetric Rydberg line in the excitation spectrum with a non-resolvable shoulder on the red-detuned side (Fig. 4.4(b)). From the spectrum, we can

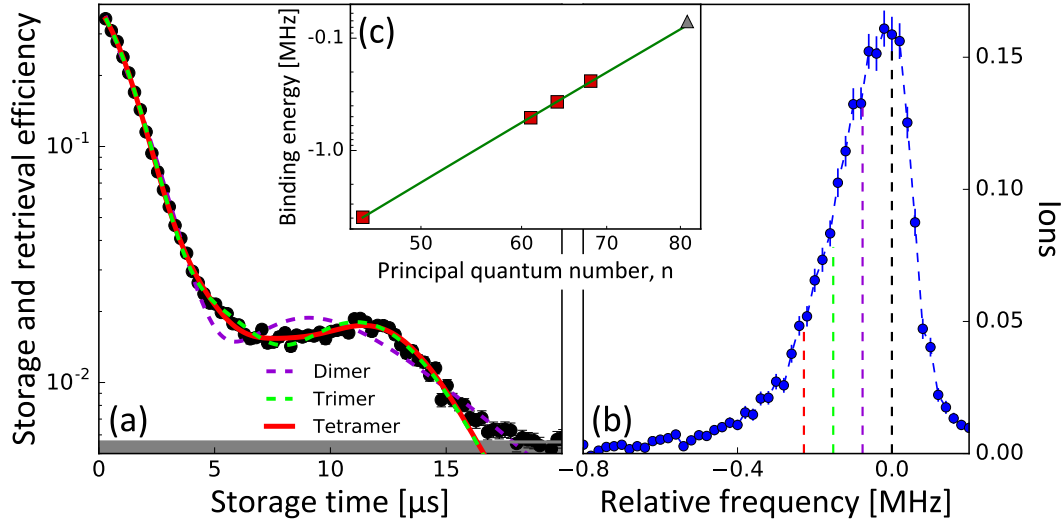


FIGURE 4.4: (a) Storage and retrieval efficiency vs storage time for $81S$ (in semilog scale). The lines are fits to the experimental data (black dots) including polyatomic molecule states up to the size indicated in the figure. (b) Corresponding excitation spectrum for $81S$. Dashed lines mark the expected centers of atomic, dimer, trimer and tetramer lines (from the right to the left), based on the dimer binding energy extrapolated from the data at lower n . (c) Measured binding energies versus principal quantum number. Red squares are the results for $n = 45, 61, 64, 68$ used for the fit (green solid line). Grey triangle is the binding energy extracted from the fit to the storage and retrieval efficiency in (a) including molecule states up to tetramer.

thus no longer directly determine the dimer binding energy. This can only be done indirectly by determining the scaling of the binding energy with effective quantum number n^* from the data at lower n (Fig. 4.4(c)). Fitting a power law $\Delta_{\text{Dimer}} \sim (n^*)^\alpha$ to the binding energies extracted for $45S$, $61S$, $64S$ and $68S$, we obtain $\alpha = -6.35(4)$, which is in very good agreement with the value $-6.26(12)$ found by Gaj *et al.* [102]. Using the binding energy $\Delta_{\text{Dimer}} = 76$ kHz predicted from this scaling, we mark the line centers of the atomic, dimer, trimer and tetramer contributions in the spectrum shown in Fig. 4.4(b). From these line positions it becomes clear that for $81S$ and our atomic density $1 \times 10^{12} \text{ cm}^{-3}$, there should already be a sizable contribution from Rydberg trimers and even tetramers in the photon storage process. Consequently, our two-species model fails to adequately describe the observed revival in the storage and retrieval efficiency in this case (dashed violet line in Fig. 4.4(a)). We can significantly improve our model by adding terms corresponding to Rydberg trimers (dashed green line) and tetramers (red line) with binding energies multiples of the dimer binding energy to Eq. 4.4. The fit with a total of four species (atoms, dimers, trimers, tetramers) reproduces the single revival feature very well, adding further polymer states does not improve the fit. Importantly, from this fit we obtain the dimer binding energy as $\Delta_{\text{Dimer}} = 71(1)$ kHz (grey triangle in Fig. 4.4(c)), in very good agreement with the value predicted by the scaling law. This shows that the photon storage and retrieval is a useful method to measure Rydberg molecule binding energies even if the molecular lines are not resolvable in the excitation spectrum.

4.8 Conclusion

In conclusion, we have shown that the coherent oscillations in the storage and retrieval efficiency of photons stored as Rydberg polaritons are caused by simultaneous excitation of Rydberg atoms and Rydberg molecules with subsequent interference between the possible storage paths. Our observations are well reproduced by a simple model including only the Rydberg dimer state over a range of principal quantum numbers $n \approx 50 \dots 70$. For higher principal quantum numbers, more molecular states become relevant. We show that our model still works well for $81S$ if the trimer and tetramer vibrational ground states are included. At even higher principal quantum number, the density of molecular states increases resulting in a continuum of molecular lines, which in turn allows the retrieval evolution to be well described by a single decay term [32]. A more sophisticated model would require including larger polyatomic molecules as well as vibrational excited states of the Rydberg molecules [167].

Rydberg molecules provide a very nice opportunity to observe the transition from “few-body” where our microscopic picture taking into account the actual distribution of individual atoms is applicable, to “many-body” where a mean-field picture becomes more appropriate. This transition was discussed previously by Gaj et al. [102] in the context of the Rydberg line shapes. Our experiments show the same transition in the context of Rydberg EIT: At low principal quantum numbers n (< 50), the molecules play no role at all, because the dimer binding energy is larger than the EIT linewidth. At intermediate n ($60 \dots 80$), where few (down to 1) molecular states are relevant, it is straightforward to fully take these states into account, which then nicely reproduces the dephasing dynamics. As we show for $n = 81$, the number of relevant molecule states which have to be included increases with n as the molecule binding energy decreases. Finally, at large n (~ 100), the number of states which needs to be included becomes very large, while at the same time the difference in binding energy for individual molecular states becomes so small that the molecule spectrum becomes practically continuous. In this regime, the mean-field treatment of the Rydberg line shift is appropriate, which no longer looks at explicit states but treats the effect of the molecules as a continuous shift proportional to (local) density. As a side remark, the microscopic treatment, including a very large number of molecule states, is of course still valid in this regime. An example in the context of Rydberg excitation lineshapes would be the work by Schmidt, Sadeghpour, and Demler [167], where indeed a large number of molecule states is taken into account to reproduce the Rydberg lineshape in a BEC. The mean-field picture greatly simplifies this complicated many-body problem and is in particular applicable in the case of Rydberg EIT, where an effective dephasing rate describes the full dynamics of the system very well.

From the perspective of Rydberg quantum optics, our observed coherence times for photon storage in Rb Rydberg dimers with principal quantum numbers close to the two-state Förster resonance exploited for efficient all-optical switch and transistor operation [34, 35, 168] suggests that coherent photonic gates based on Rydberg-mediated photon-photon interaction could be operated at

higher densities where the Rydberg dimer fraction is already significant, boosting their fidelity compared to current realizations [53, 54]. For this the involved states should be correctly chosen and the storage time should be matched to the rephasing time of the different molecule components. We believe that this changes the current established opinion which assumes that already the dimer fraction should be small for coherent operation, which restricts the atomic density to $< 10^{12} \text{ cm}^{-3}$. Based on the numbers we find, we estimate that an increase in blockaded optical depth by a factor 5...10 should be possible.

Chapter 5

Photon propagation and pollution in a dissipative Rydberg medium at large input rates

In this work we investigate quantum many-body dynamics of photons propagating through a dissipative Rydberg-EIT medium in the particular case of large input photon rates. We discuss effects of polariton propagation and an effect of “Rydberg pollution” consisting in a drastically increased rate of production of stationary Rydberg excitations inside of the medium. Obtained results reveal the importance to go beyond the existing models describing polariton physics and can indicate a new limiting factor on all experiments in the field of Rydberg quantum optics.

5.1 Introduction

In the previous chapters we discussed the recent fast development in the field of Rydberg quantum optics. In this chapter we would like to bring the attention on the many-body physics involved with strongly interacting photons.

Many-body physics is a broad field that covers many areas of modern physics, including solid state [169] and atomic physics [170]. One particular direction focuses in achieving controlled interaction of photons which can be used to generate highly correlated states of light. There are different approaches to this problem, one of which is a step by step approach that employs the interaction between individual pairs of photons as sequential building blocks. Another approach would be to find such a system where the complex state emerges from the simultaneous interaction of many photons in a highly nonlinear optical medium [11]. As many other many-body systems, the photonic systems could be used to perform quantum simulations of a Hamiltonian of interest. However, they possess some unique properties when compared with condensed matter systems: they are intrinsically driven and open — light must be injected and can leak out — and they are generally not coupled to a thermal bath [11, 171, 172]. Therefore, it is necessary to gain an understanding of quantum dynamics of strongly interacting photonic systems both by developing a theoretical framework and by studying them experimentally.

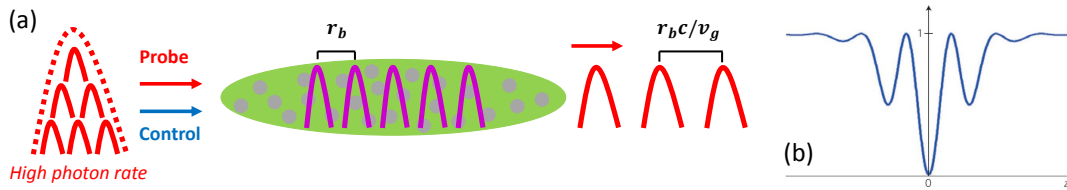


FIGURE 5.1: (a) The principle scheme of formation of a photon crystal. Input light pulse with a high photon rate (red figure on the left) creates a lot of polaritons propagating through the cloud (purple figures in the cloud). Due to the Rydberg blockade effect polaritons are separated by minimal possible distance of r_b . At sufficiently high photon rate the medium is completely filled with polaritons which are tightly packed to the minimum distance between each other. It results into the train of single photons on the output of the medium (red figures on the right) separated by $r_b c/v_g$ after the decompression, where v_g is a group velocity of propagating polaritons. (b) An example of a second order correlation function of a photon crystal taken from [11].

The propagation of light through a nonlinear Rydberg medium is one of the candidates to realize the many-interacting-photons approach to generate highly correlated states of light. In this case photon-photon interaction is induced by strong interaction of Rydberg atoms (see Chapter 2). It was shown that this approach can be used to generate a photonic state exhibiting crystal correlations: by using strong effective repulsion between photons and an effective photonic mass in EIT-based systems [41, 42] and by direct propagation of light through the dissipative Rydberg medium at high input photon rates [43, 44].

The aim of our work is to investigate the physics of dissipative Rydberg-EIT media at high intensity of input photons. As an expected effect, we try to realize a photon crystal based on the EIT light propagation through the dissipative Rydberg medium. This would allow us to generate pulse trains of single photons from a CW coherent input field (see Fig. 5.1(a)). The essence of the effect originates from the Rydberg blockade: at high input photon rates we fill the medium completely with polaritons, which will tightly pack them in space, such that they reach the minimal possible distance of r_b in between each other. This results into equally spaced single photons on the output of the medium. To observe the formation of the photon crystal, one has to look in the second order correlation function, which, in addition to the main anti-bunching feature originating from the two photon interaction and indicating the absence of overlapping photons [74] (see Chapter 2.2.5), would exhibit a long-range correlation - periodically appearing anti-bunching features, shown in Fig. 5.1(b) (in analogy with the true solid state long-range crystalline order, where such oscillations would not be damped with time for many periods). At the same time, in collaboration with the authors of original theory work [44], we can test with experimental data the proposed model for the many-body dynamics of one-dimensional dissipative Rydberg-EIT media.

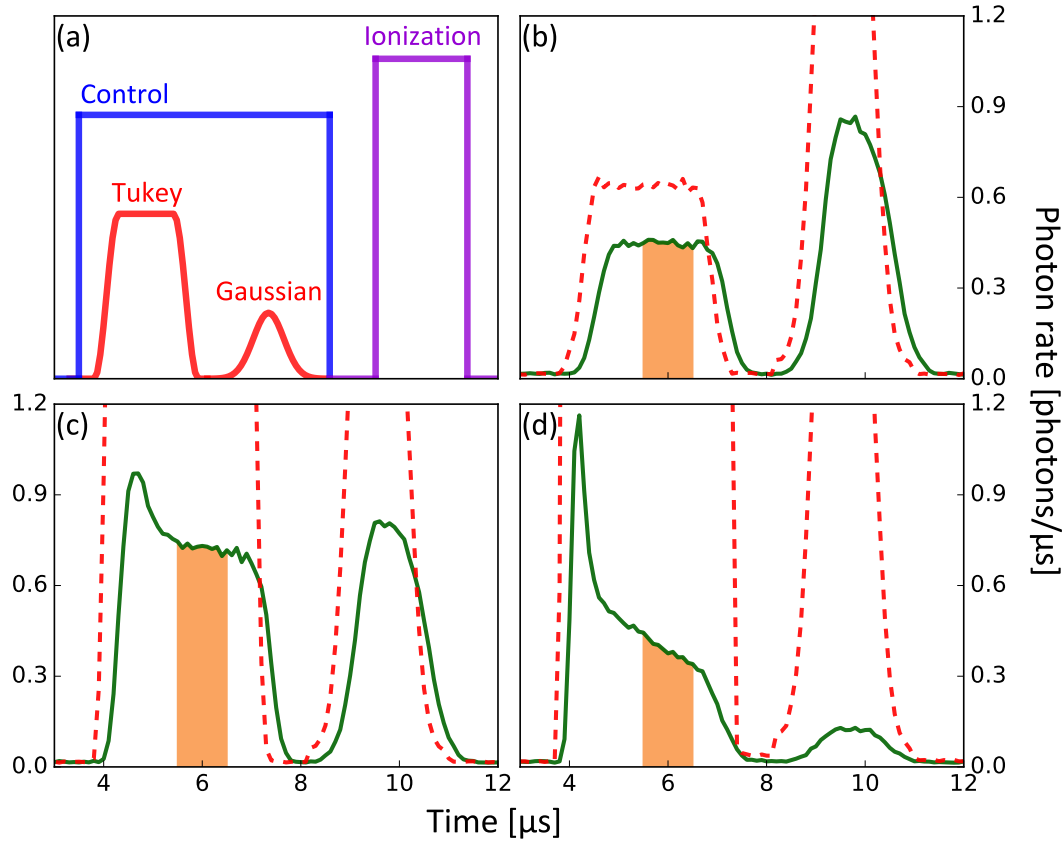


FIGURE 5.2: (a) The pulse scheme of conducted experiments: the probe pulse pattern (red) consists of two separated pulses, one of which is a Tukey shaped pulse with varying amplitude and another one is a Gaussian pulse with constant amplitude to probe the medium. Control light (blue) is on during the whole duration of the probe pulse. After control light is off, we perform field ionization of the cloud (purple). (b)-(d) Transmitted probe pulses (green solid lines) at different input photon rates: 0.6 photons/μs, 4.2 photons/μs, and 72 photons/μs, correspondingly. Red dashed lines represent input probe pulses. The shaded area indicates the steady-state region used for the photon rates evaluations.

5.2 Experimental realization

We start our experiment by preparing 8×10^4 atoms of ^{87}Rb trapped into an optical dipole trap producing a cigar shaped atomic cloud at $4\ \mu\text{K}$ with $1/e$ radial and longitudinal radii of $\sigma_R = 9\ \mu\text{m}$ and $\sigma_L = 34\ \mu\text{m}$, correspondingly. All the atoms are optically pumped into the initial ground state $|g\rangle = |5S_{1/2}, F = 2, m_F = 2\rangle$. We focus a weak 780 nm probe laser beam (Gaussian beam waist $w_{0,\text{probe}} = 6.4\ \mu\text{m}$) into the cloud, coupling the ground state $|g\rangle$ and the intermediate state $|e\rangle = |5P_{3/2}, F = 3, m_F = 3\rangle$. Scanning the probe beam frequency over $|g\rangle \rightarrow |e\rangle$ transition, we measure an optical depth of $\text{OD} = 65$ over the full cloud length. To establish EIT in the system we add a strong 480 nm control laser beam (Gaussian beam waist $w_{0,\text{control}} = 14\ \mu\text{m}$) coupling the intermediate state $|e\rangle$ and the Rydberg state $|r\rangle = |111S_{1/2}, m_J = 1/2\rangle$.

The control Rabi frequency is measured to be $\Omega_c = 2\pi \times 10$ MHz and the Rydberg EIT linewidth is $\nu_{\text{EIT}} = 2\pi \times 1.7$ MHz. The Rydberg blockade radius is calculated to be $r_b = 21$ μm . The choice of such a high Rydberg state is driven by the desire to satisfy the condition of one dimensional propagation of Rydberg polaritons, which is possible when the blockade radius is sufficiently large to fully block the cloud in the transverse direction.

A typical time sequence of a single experiment run is depicted in Fig. 5.2(a). We send a probe pulse into the medium that consists of a Tukey shaped part with a maximum amplitude which we can vary (2 μs uptime and 0.8 μs rise and fall times) and a Gaussian shaped part with a constant amplitude ($\sigma_\tau = 0.5$ μs and peak amplitude of 2.4 photons per μs). The control light is kept on during the complete duration of the probe pulse to maintain the EIT condition for both pulse components. The transmitted probe light is collected on a combination of four single photon counting modules (SPCM). Shortly after the end of the probe pulse we switch off the control light field and immediately field-ionize Rydberg atoms and collect ions on a microchannel plate detector (MCP). We use a Tukey shaped pulse with varying amplitude to investigate an effect of pulse propagation at high photon rates and a Gaussian pulse with a constant amplitude to probe the medium after the Tukey pulse left the medium.

5.3 Results and discussion

We start our investigation with the analysis of the probe pulses transmitted through the cloud. The output pulses are shown in Figs. 5.2(b)-(d) as green solid lines for different amplitudes of the input Tukey pulse. At the low input photon rate of 0.6 photons/ μs (Fig. 5.2(b)) we observe the typical behavior of the light propagation on EIT: the output pulse has a Tukey shape similar to the incoming pulse, and its amplitude is reduced due to a finite transmission of around 70% on the EIT resonance (see Chapter 2.2.1); as well, we see a delay between the input and output pulses of around 300 ns coming from the slowed propagation of light in the medium (see Chapter 2.2.2). Absolutely the same is applied to the Gaussian pulse, apart from the fact that its transmission is reduced to 50% which is connected to the blockade effect caused by excitations left behind by the Tukey pulse. Increasing the photon rate to 4.2 photons/ μs reveals an unexpected behavior in the transmitted pulse shapes (Fig. 5.2(c)): in the front of the transmitted pulse one can observe a hump - a rapid increase in the pulse amplitude, that decays on the order of a μs , and followed by a steady state region, which seems to be a back part of the Tukey shaped pulse. Going up to higher photon rate of 72 photons/ μs results in narrowing of the observed hump and, also, the flat steady state part changes to monotonic decay over time. At the same time amplitude of the Gaussian pulse decreases.

We continue our investigation of the system by calculating the output photon rate and plotting it versus the input photon rate, that is depicted in Fig. 5.3. We evaluate the output photon rate in a steady state region, which is marked in Fig. 5.2. In the case of a standard pulse propagation on EIT, one would expect to observe a nonlinear curve that, first, grows with an input photon rate and then starts to saturate due to the blockade effect on EIT, which allows only

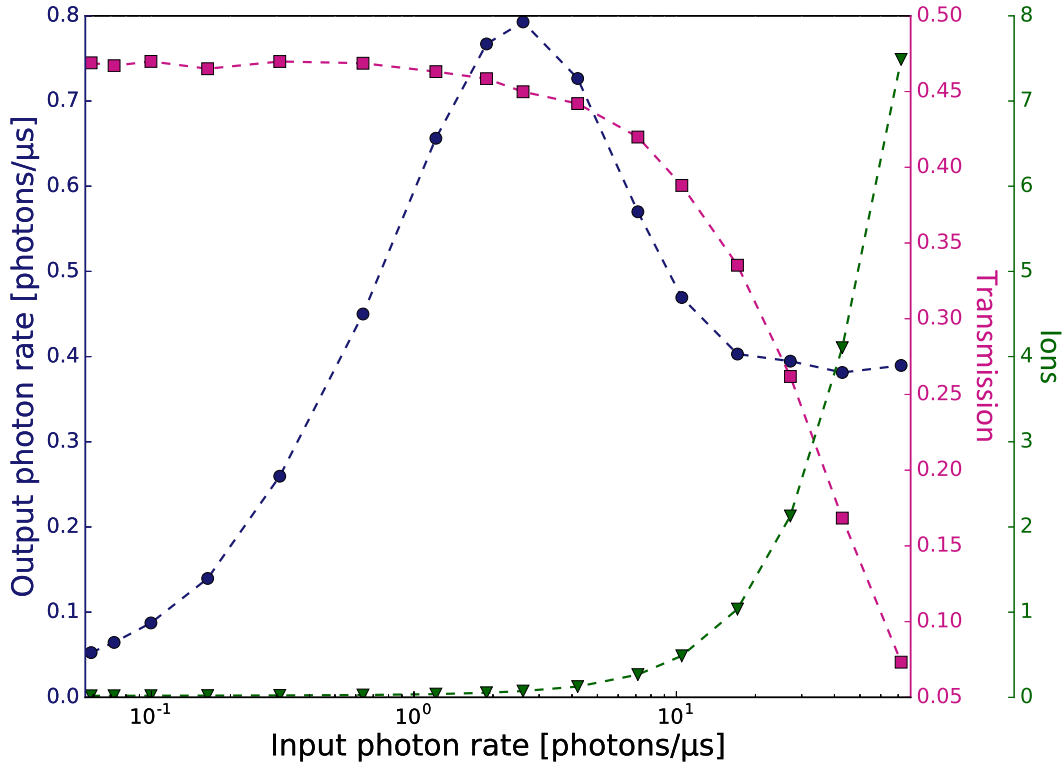


FIGURE 5.3: The plot in a semilogarithmic scale of the output photon rate (evaluated in the steady state marked in the Fig. 5.2) vs input photon rate (dark blue dots); transmission of the Gaussian pulse vs input photon rate (red squares); and the ion signal vs input photon rate (green triangles). All three lines have individual y-axes highlighted in the same color as a line itself. Dashed lines are for guiding an eye. The errorbars for most data points are smaller than the shown markers.

a single Rydberg atom to exist within a blockade volume (see Chapter 2.2.5). Therefore, at some photon rate we would fill the medium with the maximum possible amount of Rydberg excitations and further photons would not be able to couple to a Rydberg state and would be just scattered in the medium of two-level atoms ($|g\rangle \rightarrow |e\rangle$) (this is the effect that lays in the heart of a single-photon transistor [105]). However, in our experiment we observe that the initial growth of the output photon rate and its saturation (note that x-axis in Fig. 5.3 is in logarithmic scale) is directly followed by the decrease in the output photon rate reaching a plateau. The same behavior is predicted in the work by Zeuthen et al. [44], where the authors develop a theory for polariton propagation at high input photon rates in a dissipative Rydberg-EIT media. This theory work considers polariton propagation through one-dimensional Rydberg-EIT media in the limit of large optical depth per blockade radius, and it predicts the following two features of the output photon rate curve: Firstly, existence of a finite asymptote for the limit of a very high intensity, $R_{in} \rightarrow \infty$. And, secondly, existence of a local maximum in the output photon rate curve. These are exactly what we observe in our experiment and therefore our findings might be related to the deep polariton physics described in the paper [44] (see the comparison of theory and experiment in the next section).

Next, we analyze the transmission of the second pulse (the Gaussian pulse) and the ion signal detected after field ionization of the cloud. We see that transmission of the Gaussian pulse stays almost constant for the photon rates below few photons per μs and then it starts to decrease with increasing photon rate. At the same time, the ion signal starts to grow nonlinearly, reaching the point of almost 8 detected ions at 72 photons/ μs . First of all, such an amount of ions is really huge: taking into account the dimensions of our cloud and the blockade radius of 21 μm it should not be possible to fit 8 Rydberg atoms at $111S$ state in our cloud. It suggests that these additional atoms registered in the experiment, that we will call Rydberg pollutants, do not blockade each other and, thus, can be present in the cloud at the same time. Secondly, we found that the ion signal can be described by parabolic function of the form $I_{\text{out}} = I_0 + aR_{\text{in}} + bR_{\text{in}}^2$, which is really an anomalous behavior and indicates presence of a process that is not considered in the current theories on Rydberg polaritons propagation. In addition, we see that the drop in Gaussian pulse transmission happens simultaneously with the increase of the ion signal. The only simple explanation of the drop of transmission is that Rydberg atoms in $111S$ are blocked by the pollutant atoms. At third, both decay of the Gaussian pulse transmission and growth of the ion signal coincide with the point when the output photon rate start to decay. Such a coincidence could mean that the local maximum and a finite asymptote of the output photon rate could originate from the presence of Rydberg pollutant atoms in the system, and, therefore, be a consequence of a very complicated process.

As a next step, we measure second order correlation functions for different photon rates, as it was our initial motivation to observe a crystalline order of photons. Due to the technical limitations imposed by the single photon counters, it is not possible to measure correlation functions for really high photon rates (unless one has many counters). Thus, we address only the range of reasonably low photon rates. The correlation functions are presented in Fig. 5.4. First of all, we see an anti-bunching dip in the $g^{(2)}$, originating from the blockade effect [74] (see Chapter 2.2.5). There are two interesting features in the observed $g^{(2)}$ function. The first one is that the width of the anti-bunching dip decreases with an increase of the photon rate, which could indicate that the output photons are getting closer to each other in space. The second feature is the overshoot of the correlation function that appears with increasing the input photon rate. On one hand, this might be a first indication for the appearance of the crystalline order in the train of transmitted photons (the appearance of oscillating bunching features is also predicted by the theory [44]). On the other hand, we cannot observe any full oscillation in the $g^{(2)}$ functions, which would be a much stronger evidence for crystalline order formation. In the light of the found presence of pollutant atoms in the cloud, one has to be very careful in order to reveal the correct nature of the observed features in the correlation functions.

In attempt to figure out what is the nature of the observed features in the pulse shapes, correlation functions and nonlinearity curve, we are continuing with post-processing of the data. We perform filtering of our data by applying different conditions during the evaluation. The first condition is selecting

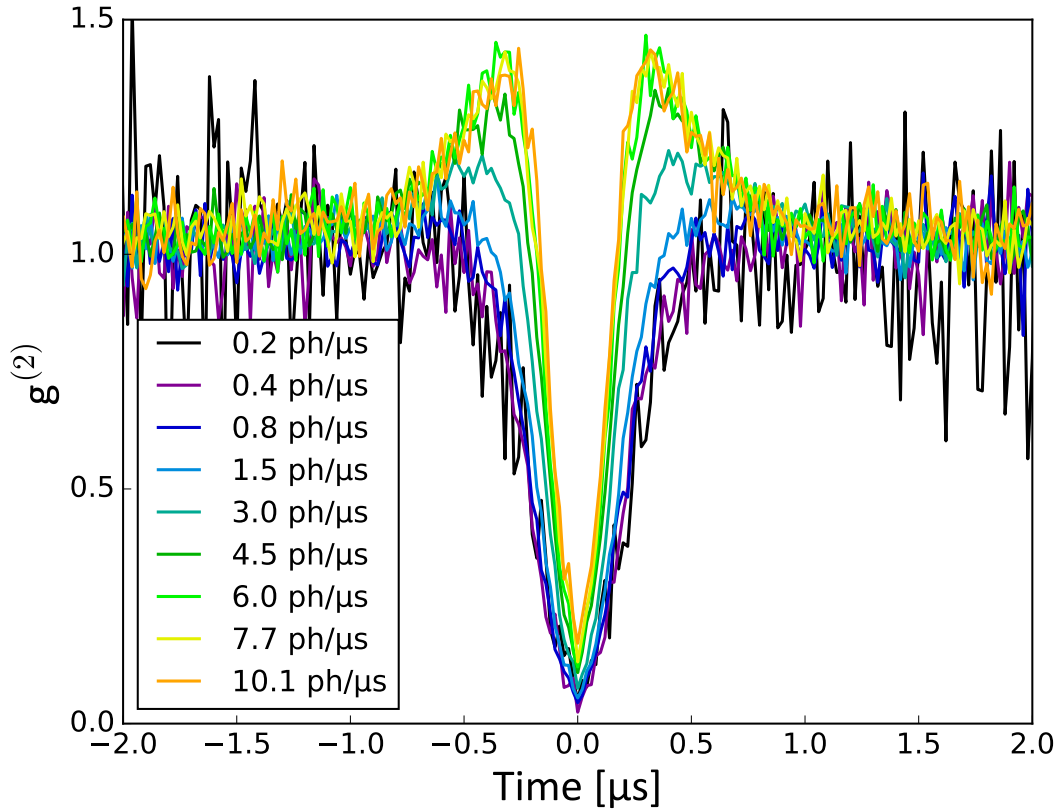


FIGURE 5.4: Second order correlation function for different input probe photon rates.

only those experimental runs which would not contain a registered ion and would contain a registered photon in the Gaussian pulse. This filter can help to reduce the impact of the pollutant atoms on the system, but, of course, we cannot guarantee the absence of pollutants in the cloud even if we register no ions due to imperfect fidelity of the process of field ionization and detection in general. Requiring the presence of a photon in the Gaussian pulse with the filtering conditions brings additional insight on what affects the transmission of the Gaussian pulse through the cloud. The second condition is selecting experimental runs which contain a registered ion, and, as a third condition, two registered ions. This allows to get understanding what happens if we always have pollutant atoms in the cloud, which is not 100% strict condition as well, because a registered ion can originate from $111S$ state or can be a dark count (though this is negligible). The output photon rates after filtering are shown in Fig. 5.5(a) and transmission of the Gaussian pulse in Fig. 5.5(b). It is seen that applying the first filtering condition of no ions and a photon in the Gaussian pulse leaves the local maximum in the output photon rate intact (red dots). The finite asymptote is replaced by a growing behavior, whose origin is not clear. The transmission of the Gaussian pulse experiences only a slight decay at highest photon rates which could mean that in this case just at high photon rates pollutant atoms (not detected in the experiment) affect the system. Taking all these into account supports the assumption that the observed features originate from the polariton physics. The filtering on 1 ion (green triangles)

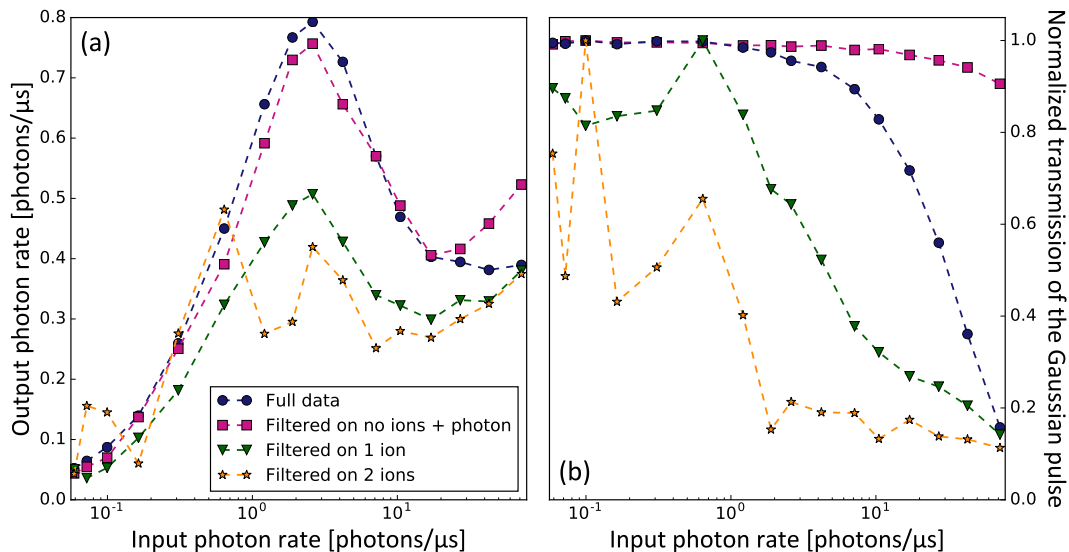


FIGURE 5.5: (a) Output photon rate and (b) normalized transmission of the Gaussian pulse vs input photon rate evaluated with different filtering conditions applied (see in the text).

and 2 ions (orange stars) in the experimental runs show that the transmission of the Gaussian pulse in these cases is very much suppressed compared to the original curve. This observation supports the assumption that suppression of transmission is coming from the blockade caused by the pollutants. The output photon rate curves under this filtering condition reveal the same behavior as for original data but with lower absolute values of the output photon rates, suggesting that pollutants might just blockade atoms in $111S$ state, what leads to an overall decrease in the amplitude of the curve. After all, the hump in the output photon rate curve seem to be stable over different filtering conditions, what, again, supports the assumption that all the observed features originate from the polariton physics [44] and pollutants just add a blockade effect on top of it. On the other hand, these evaluation is not strong enough to absolutely confirm the nature of the new features in our data. So, the presence of the local maximum in the curve conditioned on 1 ion still leaves the chance that it originates from the pollutant atoms in the system. As well, changing behavior in the steady state region is really not understood and thus adds some complications. Finally, obtained results cannot provide a confident conclusion on real nature of observed effects.

5.4 Comparison with the theory

We collaborate with the group of Alexey Gorshkov from JQI in Maryland, which developed the original theory [44], to simulate the results that we obtain in the experiment. The essence of the theory is the following: when the first photon from the pulse enters the medium it produces a Rydberg polariton propagating through it. The Rydberg-Rydberg interaction between polaritons leads to one

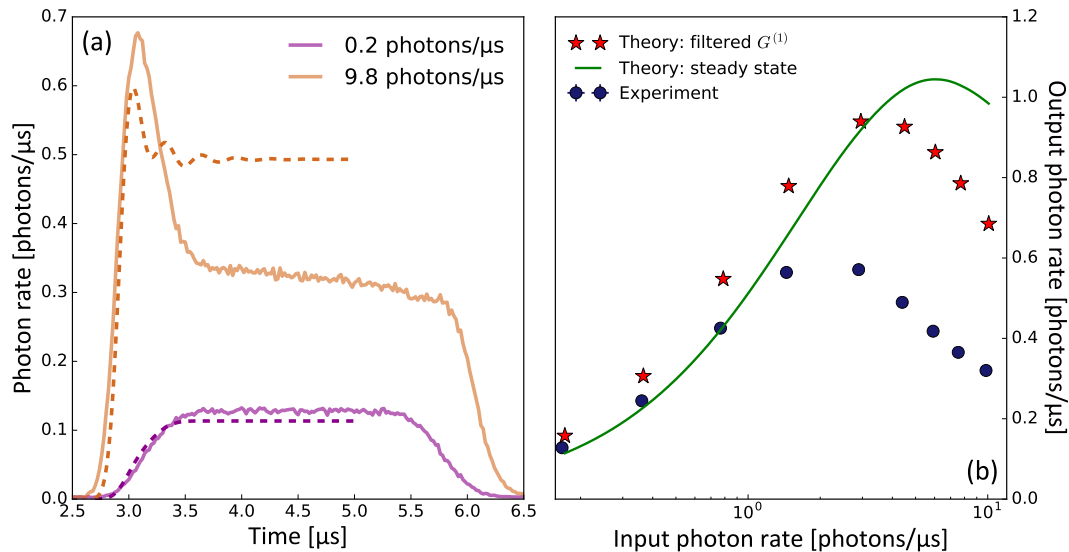


FIGURE 5.6: Comparison between theory and experiment. (a) Pulses transmitted through the cloud at 0.2 photons/μs (magenta) and 9.8 photons/μs (brown). Solid lines represent the experiment and dashed lines represent the theory derived from $G^{(1)}(\tau, \tau)$ function. (b) Output photon rate as a function of an input photon rate: experiment is dark blue dots, theory curve derived from the filtering of $G^{(1)}$ function is red stars and theory curve from steady state analysis is green solid line.

polariton destroying the lossless EIT-propagation for other polaritons. Therefore, while a polariton stays within the blockade radius r_b at the entrance of the medium, all the arriving photons are scattered out of the forward propagating mode. A direct consequence is that polaritons in the medium will be separated by their blockade radius r_b , what results in a train of single photons on the output of the medium spaced by decompressed blockade radius $r_b c/v_g$. Secondly, as a result of photon scattering at the entrance of the medium, the environment effectively projects the wave function of the polariton to be localized within the arrival time interval. Due to the finite EIT window this projection results in polariton losses and the anti-bunching feature in the correlation function will have an extent which significantly exceeds the blockade time $\tau_b \equiv r_b/v_g$. This can be attributed to the spectral features of width $\sim 1/\tau_b$, but they are washed out during propagation due to EIT filtering and dispersion. By building a model that includes these single-polariton EIT effects, the authors could find analytical expressions for the steady state output. In general they use a hard sphere model of the blockade and consider one dimensional polariton propagation with imperfect EIT. For the particular details of the theory we refer to the original paper [44].

The theoretical calculations were done using the experimental parameters. There are two approaches to find the discussed theoretical curves: the first approach comes from the analytic solution for the steady state output photon rate but it cannot predict pulse shapes. The pulse shapes can be calculated using a second approach based on the same-time first-order correlation function $G^{(1)}(\tau, \tau)$ which includes two parameters, blockade time τ_b and filtering time τ_{EIT} that are used in the Gaussian filtering. Of course, the latter approach also

allows getting the output photon rate curve independently, which has to be consistent with the steady state result.

We present the comparison of the theory and experiment in Fig. 5.6. The theory calculations use the parameters of the experiment without any free parameters. The outgoing pulse shape can be well described by the theory at the photon rates $R_{\text{in}} < 1$ photons/ μs (Fig. 5.6(a), magenta line). However, at the high photon rates (brown line), the predicted behavior deviates from what is observed in the experiment. First of all, the predicted value for the steady state in the pulse is higher than what we observe in the experiment. Secondly, the hump in the beginning of the theory pulse has smaller amplitude than the one in the experiment, and it is followed by some oscillations that are never present in our measurements. These deviations cannot be explained also just by adding the increased absorption due to pollutant atoms into the calculations. As well, deviations between theory and experiment are observed in the output photon rate (Fig. 5.6(b)). The green theory line, obtained from the steady state analytic solution taking into account the finite transmission and also additional damping due to pollutants, has much higher amplitude than the experimental curve (blue dots). The theory obtained from the filtering of the $G^{(1)}(\tau, \tau)$ function (red stars) has a higher amplitude as well, though the general trend in this theoretical curve is very similar to the one we observe in the experiment. In the end, one can say, that on some level there is a qualitative agreement between the theory and the experiment. But there are some deviations which cannot be easily explained by the theory and require deeper understanding of the involved processes. The existence of these deviations does not allow us to attribute the observed effect with confidence to the polariton propagation physics.

There are some additional factors that were investigated during this work, such as the shape of the input probe pulse, the control Rabi frequency, or the OD per blockade. For example, the theory predicts washing out of the oscillations in the output pulses if the rising time of the pulse becomes too long. The measurements with varying rising times from 0.08 μs to 1 μs were insensitive to this parameter, which again contradicts the theory. Measurements with the different cloud length, namely, a short cloud with $\sigma_{\text{R}} = 10 \mu\text{m}$ and $\sigma_{\text{L}} = 6 \mu\text{m}$, exhibit qualitatively the same behavior differing only in the amplitude of the observed effects.

The joint work with the group of Alexey Gorshkov is still going on. In addition, we collaborate with the group of Darrick Chang from ICFO in Barcelona, who uses a direct numerical method to solve this problem. Both theoretical approaches seem to be consistent with each other which confirms the validity of the theory developed by Zeuthen et al. [44]. One reason why the observations differ from the theory prediction can originate from the fact, that the experimental system is not truly a one dimensional system, while the theory works exclusively for the one dimensional case. We will discuss later the related ideas and the prospects of the collaboration in the outlook of this chapter.

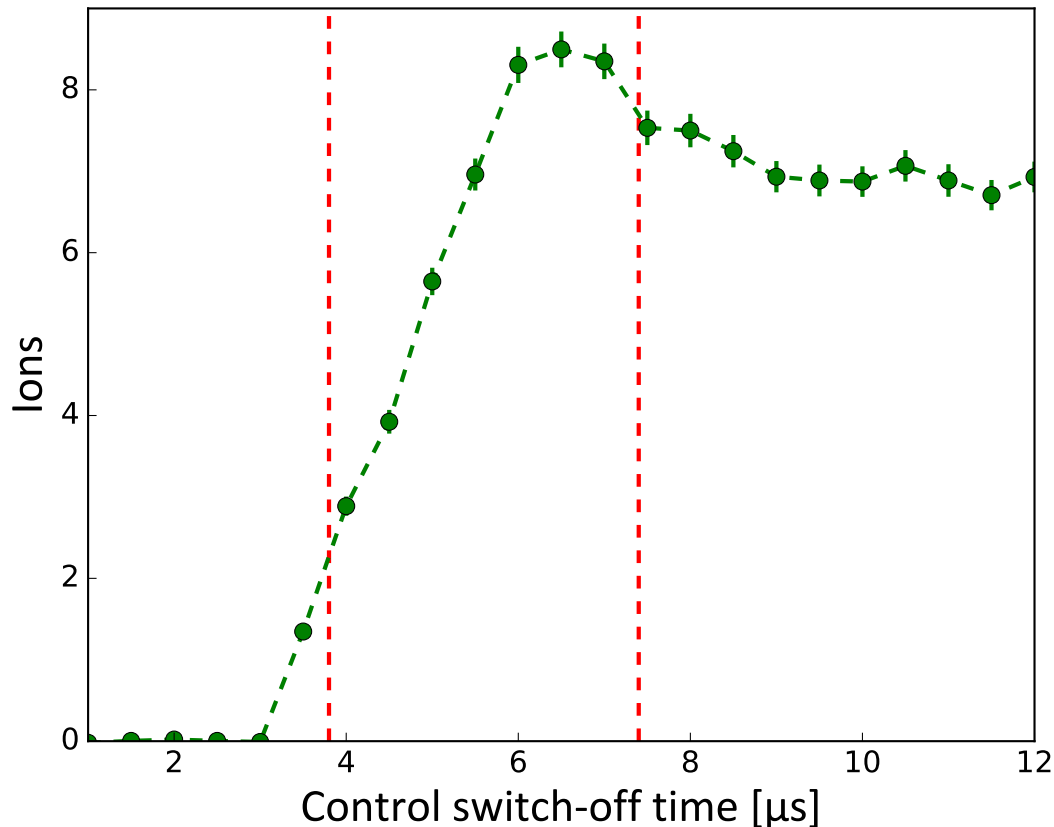


FIGURE 5.7: Scan of the control switch off time: green dots represent the ion signal measured on MCP at the input probe photon rate of 72 photons/ μs . Green dashed line is shown for guiding an eye. Red dashed lines mark the position of a probe pulse.

5.5 State selective ionization

We have found in our experiment that the ion signal grows nonlinearly with an input photon rate and it reaches high values that are contradicting our expectations. This anomalous behavior we would like to understand better. We start our investigation with the following measurement. We perform the same measurements described in Section 5.2 with the difference that we move the point in time when we switch off the control field (Gaussian pulse is off in these measurements). This time interval covers the full length of the probe pulse and goes beyond it. Right after the control light turns off we perform field ionization and count ions. The results of this measurement for $111S$ state, performed at the input probe photon rate of 72 photons/ μs , can be observed in Fig. 5.7, where we see the ion signal plotted versus the time when we switch the control light off. Looking at Fig. 5.7 it is seen that, first of all, signal grows, as expected, because we store more excitations (but of course the magnitude of the signal is anomalous as it was discussed). After the point where control light stays on longer than the length of the probe pulse, the decay of the ion signal starts. In the normal situation all the atoms in $111S$ state should undergo spontaneous Raman decay driven by the control light field, which is in resonance with $|e\rangle \rightarrow |r\rangle$ transition, with the rate $\gamma_{\text{Raman}} = \Gamma_e/2$, which in our case results

in the $1/e$ decay time of ~ 330 ns. However, we do not observe such a decay rate in our measurement: the signal decays slightly and then stays almost constant at the level of 6.7 ions for as long as 4 μ s. Due to the technical restrictions, we could not measure this curve for a sufficient period of time to extract the decay time. This observation means that the atoms, from which ions were produced, are not coupled to the control light field and, therefore, must be in a different Rydberg state.

To gain more understanding of the origin of the pollutant atoms appearing in the experiment we perform a scan of ionization voltage and, thus, the electric field in the system. This method is also known as a state selective ionization, and one expects to see a step-like growing when plotting the number of registered atoms as a function of applied electric field with a sharp beginning, that would originate from a single Rydberg state in such a measurement. The sharp feature is positioned around the ionization threshold of the excited state. Consequently, if there are few different states excited in the system, one expects to observe few steps at corresponding threshold electric fields.

As we work with high Rydberg states the threshold values of electric fields are quite low and, more importantly, very close to each other. However, we usually apply a high ionization voltage because it is convenient and does not require adjusting, if we change the state we work with. This results in difficulties in controlling the electric field precisely at low values with our usual high voltage source. To overcome this limitation, we use multi-channel USB analog high-drive voltage source with high stability from Measurement Computing. It can drive voltages between 0 V and ± 10 V, and we attach the positive voltage to electrodes 2 and 6 and negative voltage to electrodes 4 and 8 of our electric field control (see Chapter 3.1.5). This allows us to cover the necessary electric field region with a good precision. In the same time, when we scan the electric field, we have to change the voltage applied on the electrode 9 for steering electrons towards the MCP. In the case when we apply positive and negative voltages on the opposite electrodes, the usual guiding electric field outside of the volume surrounded by electrodes 1-8 get canceled. So, one has to take it into account and find a correct steering voltage.

In Fig. 5.8 the ion signal measurement vs applied electric field working with $111S$ state is shown. The threshold electric field for $111S$ state is 2.37 V/cm and, therefore, we would expect to see a step around this value if there are only atoms at $111S$ state. We perform this measurement for two cases, the first one is when we turn off the control field at 6.5 μ s, right "in the middle" of the the probe pulse (see Fig. 5.7), which should result in higher amount of atoms in $111S$ state. We ionize the cloud right after control field is off and the measurement is shown in Fig. 5.8 by blue triangles. The second measurement is done when we turn the control field off at 12 μ s after a delay of around 4 μ s from the end of the probe pulse (see Fig. 5.7), which has to lead to some decay of the atoms in $111S$ state due to spontaneous Raman decay mentioned above. We again ionize right after we switch off the control field and the data is presented by green circles in Fig. 5.8. First of all, we should note that the sharp edge at around 0.2 V/cm is coming from the technical side of the measurement and has no real physical meaning: at these low ionization fields it takes quite some time

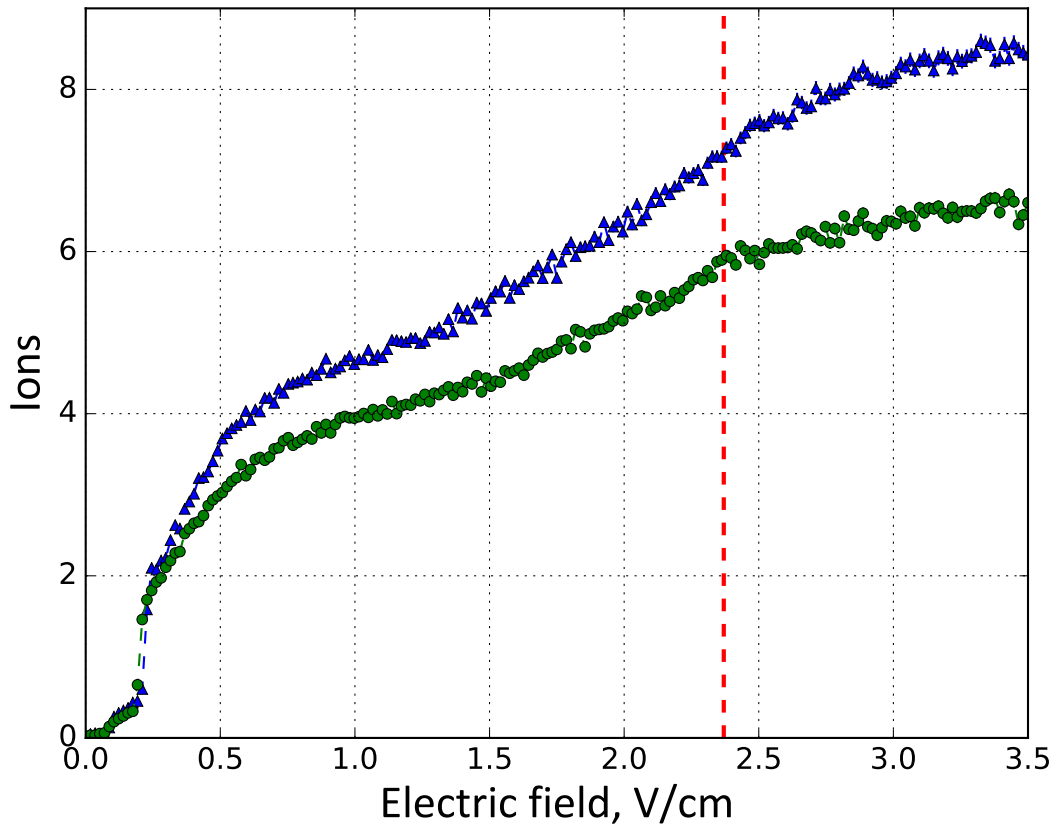


FIGURE 5.8: Ion signal measured vs ionization electric field. Blue triangles represent the case when control light is switched off at $6.5 \mu\text{s}$, "in the middle" of the probe pulse; green circles represent the case when control light is switched off at $12 \mu\text{s}$, with a delay after the back of the probe pulse (see for reference Fig. 5.7). Red line marks the point at 2.37 V/cm - the ionization threshold electric field for $111S$. The errorbars for most data points are smaller than the shown markers.

for ions to arrive to the detector. Therefore, one has to wait a sufficient time to collect the signal. In this measurement waiting time was not set sufficiently long to collect the signal for the covered electric field range. Thus, we observe this sharp edge, which expected to be just a smooth decay to zero as a continuation of the curve from high electric fields. At second, we mark the threshold electric field for $111S$ state with red line in Fig. 5.8 and it is clear that there is no typical step around this value. We rather observe a smooth growth of the ion signal with applied electric field. This suggests that pollutant atoms do not populate the initial $111S$ state and even more they do not populate a single state but rather distributed among the various states. We can say for sure that this state range covers the states with $n > 111$ because we clearly observe the strong signal below the ionization threshold of $111S$ state. A comparison of the signals from the center of the probe pulse and the end of the probe pulse suggests that some of the pollutant atoms populate the states with $n < 111$.

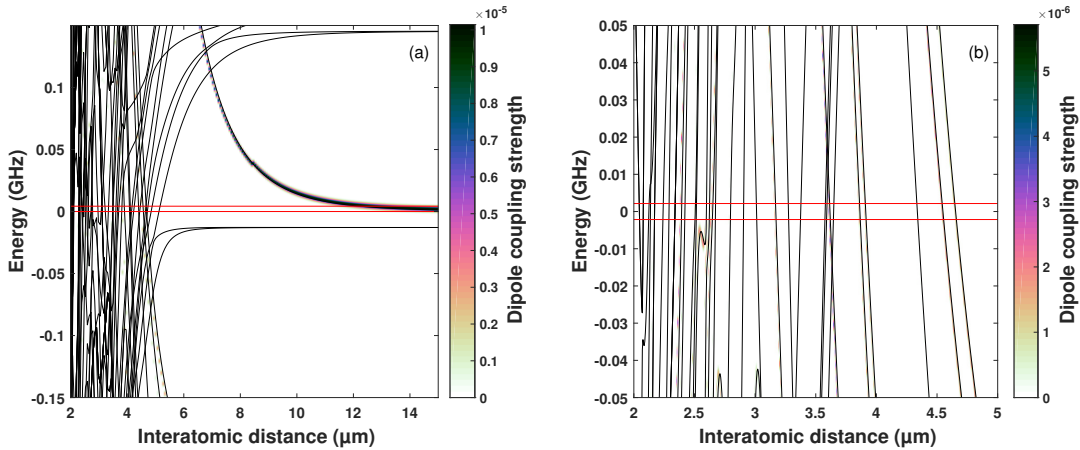


FIGURE 5.9: Potential landscape around $|89S, 89S\rangle$ pair-state. The color map represents the dipole coupling strength to the ground state. (a) The full range potential, the brightest line is $|89S, 89S\rangle$ pair-state. (b) Zoom into the range from 2 μm to 5 μm shows the bunch of potential lines that cross zero and have dipole coupling to the ground state. Red lines mark the EIT linewidth in the system.

5.6 A hypothesis on Rydberg pollution

As it was shown above, we found that ion signal grows not linearly with increasing input photon rate but has a form of a sum of quadratic dependence and linear dependence. As well we have seen that there must be a state change during the process of pollutant atoms production. This unusual behavior suggests that there might be some other process involved in the propagation of polaritons on EIT resonance, leading to such a behavior in ion signal. In this section we try to come up with a model that could potentially explain the observed behavior. During our discussion in this chapter we will use $89S$ state as initial state excited with the lasers, but the results would not differ from $111S$ state.

First, we started with an estimation of the rate of black body radiation (BBR) induced transitions for our system. The calculated BBR lifetime for $89S$ state is 389 μs which results in the transition rate of 2.6×10^{-3} atoms/ μs . As well, the BBR induced pollutant production has a linear behavior with input photon rate and it probably just serves as a tiny addition to the main mechanism.

Our next step will be considering the potential landscape of interacting Rydberg atoms, that was explained in the Chapter 2.1.4. For this we calculate the potential landscape for $|89S_{1/2}, 89S_{1/2}\rangle$, that is shown in Fig. 5.9(a). Now our task is to find such potential lines that cross zero energy at some particular distance and can be excited by the laser light. This becomes possible due to the interaction of Rydberg atoms, and to do this, we calculate a dipole coupling strength to the ground state for each potential line, which is shown in Fig. 5.9 by the color. At every particular distance a wavefunction represents a linear combination of different pair states, therefore the coupling can originate from any combination of two states $|\text{state1}, \text{state2}\rangle$. However, in our system we always excite initially $89S$ state, therefore we consider only the interaction with this particular state, and choose such pair-states, where one state is always $89S$

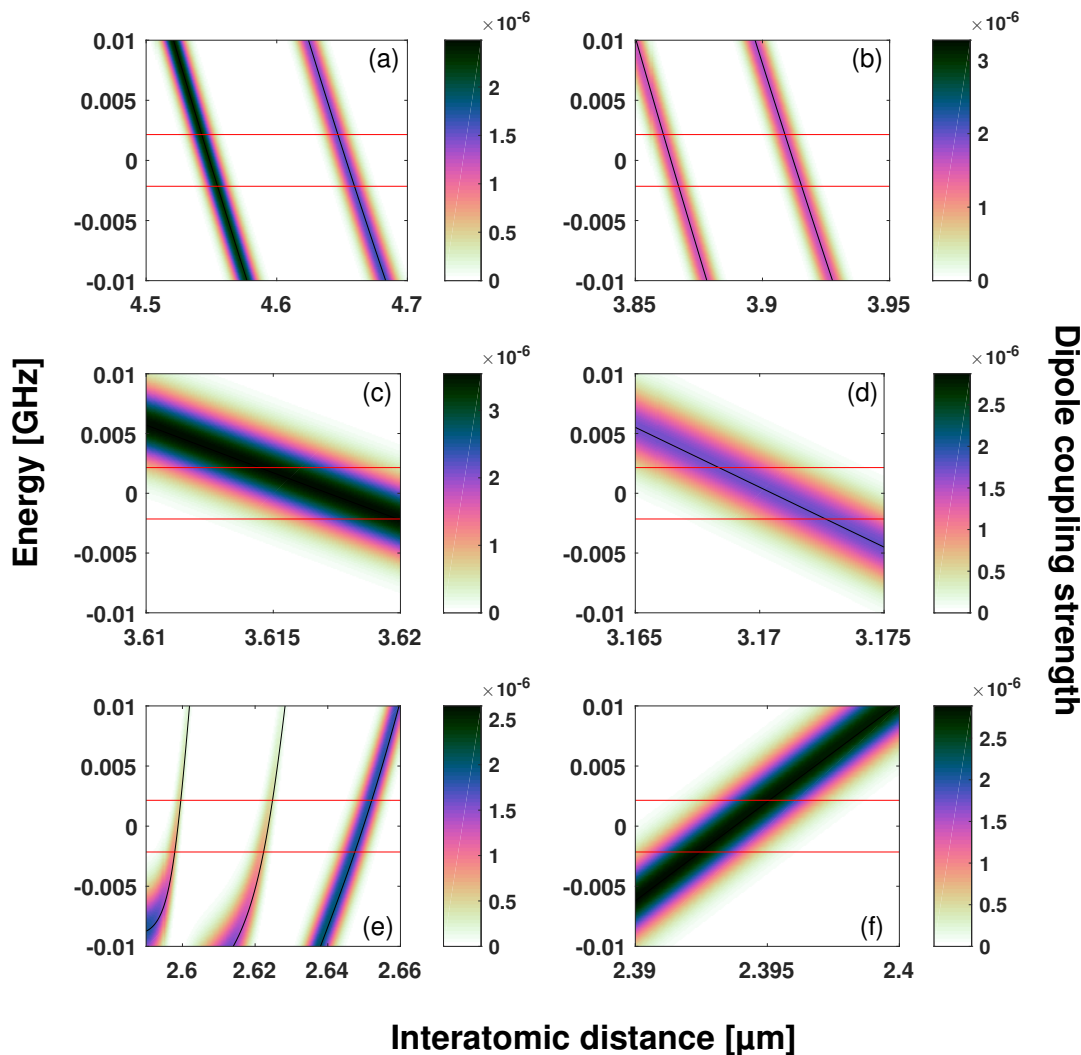


FIGURE 5.10: Potential landscapes around particular interatomic distances. The color map represents the dipole coupling strength to the ground state. Red lines mark the EIT linewidth in the system.

- $|89S, \text{state2}\rangle$ or $|\text{state1}, 89S\rangle$). Indeed, one can see on Fig. 5.9 that there are bunch of lines in the region from $2\mu\text{m}$ to $5\mu\text{m}$ that have a nonzero coupling strength and cross zero energy. It means that if we create $89S$ Rydberg excitation in the cloud, then at some particular distance r_0 from this excitation, even if this distance is inside of blockade region $r_0 < r_b$, we can excite another Rydberg atom in another state. Such a mechanism could lead to the production of Rydberg atoms in the states different to $89S$.

The idea on how this mechanism could be applicable to the real system is the following: when a photon enters the medium it propagates through it in the form of Rydberg polariton coupled to $89S$ state. For some time the entrance of the medium is blocked by the polariton. When this polariton passes the distance $r_0 < r_b$, there is a probability that another photon would enter the medium at exactly this time. If this situation happens, it becomes possible to excite a corresponding pair-state consisting of $89S$ state and some different Rydberg state. Of course, as discussed above, excitation of an atom in such situation is

only possible when there is a corresponding potential line crossing zero energy at the distance r_0 (the process is energetically allowed) and transition must have non-zero dipole coupling strength to the ground state. But this would happen even though the new photon is inside of the blockaded region. It is logical to assume that at higher photon rates such a mechanism should become more relevant. In practice, the period of time when the state different to $89S$ can be excited is not instant but defined by EIT linewidth in the system: the process is energetically allowed in some space region $[r_0 - d/2; r_0 + d/2]$ where light is still coupled to the pair state due to the finite EIT linewidth (see red lines in Fig. 5.9 and Fig. 5.10 that cross potential line at different distances). The time that takes polariton to propagate through the distance d is given by

$$\Delta\tau = \tau_{\text{delay}} \frac{d}{L}, \quad (5.1)$$

where L is a cloud length. The probability p that another photon arrives during this time would be given by Poisson statistics:

$$p = P(1) = \frac{\mu e^{-\mu}}{1!} = R_{\text{in}} \Delta\tau e^{-R_{\text{in}} \Delta\tau} \xrightarrow{R_{\text{in}} \Delta\tau \ll 1} R_{\text{in}} \Delta\tau. \quad (5.2)$$

where R_{in} is an input photon rate. Then the amount of produced pollutant atoms for a single polariton in the medium would be a product of probability to get a photon during the propagation time p , the probability to couple to the pair state (derived from the coupling strength) η and the amount of input photons N_{in} . To get the full amount of pollutants produced one has to multiply the result by amount of polaritons transmitted through the cloud:

$$N_{\text{pollutant}} = \eta p N_{\text{in}} N_{\text{polaritons}} = \eta \tau_{\text{delay}} R_{\text{in}} N_{\text{in}} N_{\text{polaritons}} \frac{d}{L}. \quad (5.3)$$

If we have a bunch of such resonances at different distances, we can extend the obtained result to

$$N_{\text{pollutant}} = \tau_{\text{delay}} R_{\text{in}} N_{\text{in}} N_{\text{polaritons}} \frac{\sum d_i \eta_i}{L}. \quad (5.4)$$

From such an argumentation one can conclude that the amount of ions would grow nonlinearly with the input photon rate.

To find all the relevant resonances we calculated the potential landscapes around the particular distances, which can be found in Fig. 5.10. From this data we extract distance d , coupling strength of a particular resonance, and also a pure pair state from which the biggest coupling originates, which are presented in the Table 5.1. Note that the coupling strength to the $|89S_{1/2}, 89S_{1/2}\rangle$ pair-state is 10×10^{-6} that we obtain at long distance and which we use as a normalization factor to obtain a probability to couple to a pair state for each particular line. Also for every presented pair state $|\text{state1}, \text{state2}\rangle$ there is always the opposite pair state $|\text{state2}, \text{state1}\rangle$, that makes the same contribution, but we do not mention it for simplicity. To obtain the results we used EIT FWHM $\nu_{\text{EIT}} = 4.3 \text{ MHz}$ derived from the experiment. From the obtained data

Figure	Distance [nm]	Strength	Pair-state
(a)	14	2.3×10^{-6}	$ 89S_{1/2}, 89S_{1/2}\rangle$
(a)	13	1.5×10^{-6}	$ 89S_{1/2}, 89S_{1/2}\rangle$
(b)	6	1.6×10^{-6}	$ 89S_{1/2}, 87D_{3/2}\rangle$
(b)	6	1.6×10^{-6}	$ 89S_{1/2}, 87D_{3/2}\rangle$
(c)	6	3.5×10^{-6}	$ 89S_{1/2}, 87D_{5/2}\rangle$
(d)	5	1.7×10^{-6}	$ 89S_{1/2}, 87D_{5/2}\rangle$
(e)	5	1.8×10^{-6}	$ 89S_{1/2}, 87D_{3/2}\rangle$
(e)	3	0.5×10^{-6}	$ 89S_{1/2}, 87D_{3/2}\rangle$
(e)	1	0.5×10^{-6}	$ 89S_{1/2}, 87D_{3/2}\rangle$
(f)	3	2.8×10^{-6}	$ 89S_{1/2}, 89S_{1/2}\rangle$

TABLE 5.1: Parameters of the resonances from the Fig. 5.10. The coupling strength to the $|89S_{1/2}, 89S_{1/2}\rangle$ pair-state is 10×10^{-6} . EIT FWHM $\nu_{\text{EIT}} = 4.3$ MHz. For every presented pair state $|\text{state1}, \text{state2}\rangle$ there is always the opposite pair state $|\text{state2}, \text{state1}\rangle$, that makes the same contribution, but we do not mention it for simplicity.

we can observe that the distance in space d that polariton passes, which gives a chance to couple to another pair-state, is really tiny. Therefore we cannot expect the rate of producing new excitations to be very high.

It is not possible to calculate the potential landscape precisely below around $2 \mu\text{m}$. In this region the amount of states is too high, therefore, results become incorrect. Thus, as an extension to the above model, one could add the whole deep spaghetti region into the consideration: basically if the distance between traveling polariton and newly coming photon is below $2 \mu\text{m}$ (which is chosen empirically), then there is a probability that a new photon would produce a Rydberg atom. Such an assumption could be justified by the fact that the density of potential lines in deep spaghetti region is very high, but it is unknown what really happens there.

To test the whole idea we perform a Monte-Carlo like simulations of the proposed model. We simulate an input Tukey light pulse as a set of time bins with Tukey envelope, filled with photons according to Poisson statistics, completing the pulse length time, and a medium as a set of space bins with the total length L . We assume that the first photon of the pulse becomes a polariton and propagates through the cloud. Then we check if this polariton leaves the blockaded part at the entrance of the medium before the second photon arrives to the entrance of the cloud. If yes, then no pollutants are produced. If no, we treat this photon as flying through the cloud of two-level atoms with a speed that is intrinsically much higher than the speed of polariton propagation, and therefore we treat a polariton as stopped excitation. In this case we have two opportunities to create a pollutant atom: either it happens when the distance between two of them is below $2 \mu\text{m}$ with a probability of p_{ds} , or the distance is bigger than $2 \mu\text{m}$. In the later case a pollutant can be formed by probing the resonances which can be interpreted as a single effective resonance with probability p_{res} derived from Eq. 5.4 and data from the Table 5.1. Thus, we just

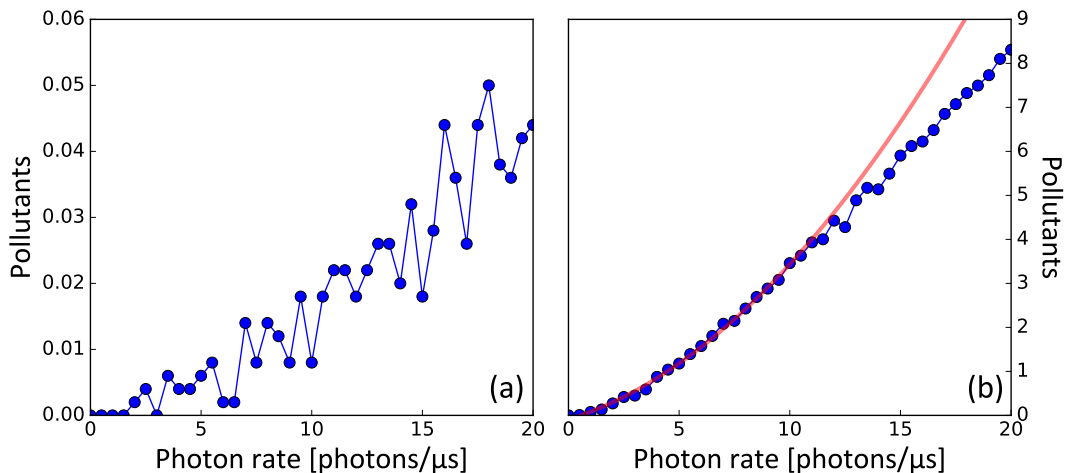


FIGURE 5.11: Simulation of the pollutant atoms production by (a) single resonances in the spaghetti region and (b) deep spaghetti region. We set the probability to produce a pollutant in the deep spaghetti region to $p_{\text{ds}} = 1$. The red curve in (b) indicates the parabolic fit to the simulated data.

throw a dice twice to test if we get a pollutant atom or not. As well we include the scattering probability for photons flying through the two-level medium, the probability that polariton decays during it's propagation and the probability to create a pollutant by BBR induced transition. The whole procedure is repeated with all the photons that fit in the time interval of a polariton traveling through blockaded region at the entrance of the medium. When this polariton is gone, we take the next photon, turn it into a polariton and repeat the whole thing again. Following this procedure we can find how the amount of pollutant atoms depends on the input photon rate.

The result of such a simulation is shown in Fig. 5.11. We set the cloud length to $30 \mu\text{m}$, delay time to 400 ns , blockade radius to $12 \mu\text{m}$, OD per cloud length to 70, BBR lifetime to $389 \mu\text{s}$, the size of deep spaghetti region to $2 \mu\text{m}$; the length of the time pulse is $3.6 \mu\text{s}$. We extract the amount of produced ions from both sources: on Fig. 5.11(a) one can see pollutant ions originating from the resonances that are described in Fig. 5.10 and Table 5.1; and in Fig. 5.11(b) pollutants originating from the deep spaghetti region are depicted. Note that in this calculation we have used the probability to create a pollutant atom in deep spaghetti region $p_{\text{ds}} = 1$. The clear message of this simulation is that the amount of pollutant atoms that are coming from the single resonances is extremely low and definitely is not able to describe anomalously high amount of pollutant atoms that we observe in the experiment. This happens just because these resonances, translated to the distance in space, are very narrow (Table 5.1) and, therefore, the probability to excite them is low. On the other hand, the amount of pollutant atoms coming from deep spaghetti seems to be quite high and match the experiment on the order of magnitude. Fitting the simulation data in Fig. 5.11(b) with a parabola we find that at low photon rates the ion curve can be approximated with a sum of quadratic line and a linear line, while for the higher photon rates there is a deviation from such behavior.

Next, we try to simulate the real experiment data with this model to see if

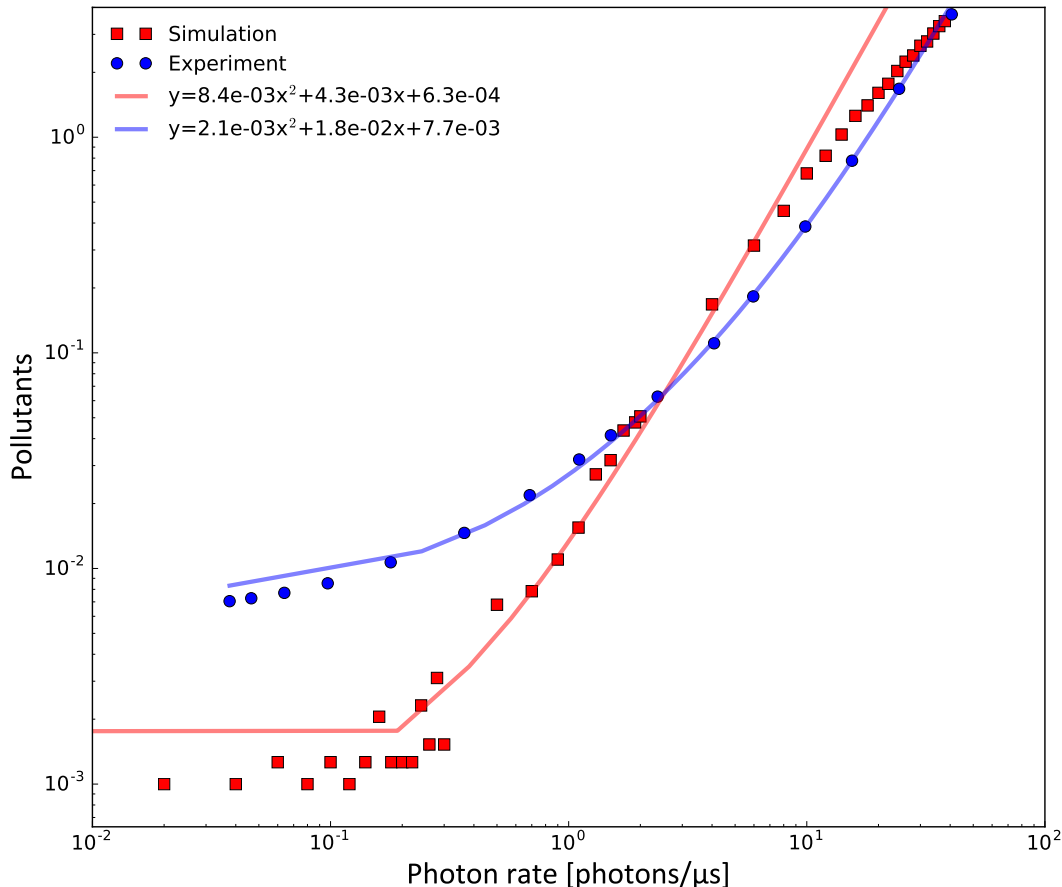


FIGURE 5.12: Comparison between experiment data (blue dots) and simulation (red squares). Solid lines indicate parabolic fit to the data.

we can approach the experimental behavior with it. We have seen that single resonances do not produce enough pollutant atoms to explain the experiment data. Therefore, we just sum up pollutant contributions from both sources and do not distinguish between them anymore. To match the experiment data we adjust the probability to create a pollutant atom in the deep spaghetti region p_{ds} . The result can be seen in Fig. 5.12, where we use $p_{ds} = 0.25$. We also add pollutant atoms produced by BBR and MCP noise to the full amount of pollutants in Fig. 5.12. We see that there are serious deviations between simulations and experiment. Even at small photon rate, where BBR should be one of the main contributor, the expected pollutant number is smaller than it is measured in the experiment. As well, for higher photon rates we see that the simulated behavior differs from the measured one, though it is also nonlinear. In addition, we have observed in the experiments with a shorter cloud the deviation of the ion signal from quadratic with increasing input photon rate. We tried to vary the length of the cloud to see how it affects the simulation results. But it is not possible to achieve a better match between the experiment and simulation.

Finally, from the whole discussion above, first of all, we can see that the initially proposed mechanism of pollutants formation through exciting single resonances in spaghetti region is not realistic due to very low probability to excite them. The second source of generation of pollutant atoms - the deep

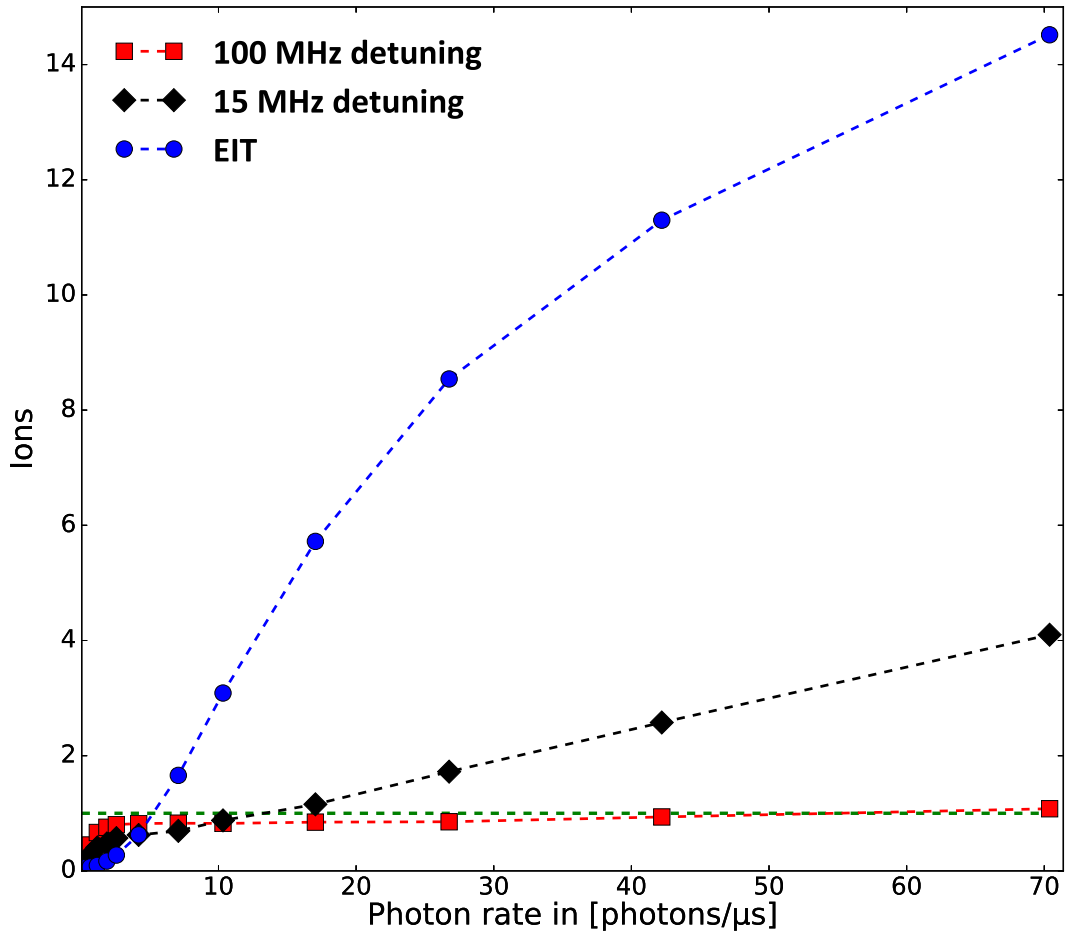


FIGURE 5.13: Measurement of an ion signal as a function of an input photon rate in the small cloud for the case of EIT (blue dots), dispersive case of 15 MHz detuning from the intermediate state (black diamonds), and off-resonant case with 100 MHz intermediate state detuning (red squares) (we are always on-resonance with Rydberg state). Dashed lines are shown for guiding an eye. Green line marks the level of one ion. The errorbars for most data points are smaller than the shown markers.

spaghetti region - could produce a result that somehow quantitatively agrees with the values we obtain in the experiment. But such an approach has really no solid physical background, because the parameters we can use to describe this region are empirical and we cannot really state why a pollutant atom is excited. In addition, using the proposed mechanism does not allow us to get reasonable qualitative agreement with experiment data. All these arguments influence our opinion to be against the proposed hypothesis. In the following chapter we will perform an experimental check of the hypothesis and confirm that this process cannot be a source of pollutant atoms.

5.7 An experimental test of the hypothesis on Rydberg pollutants formation

To test the hypothesis discussed in the previous chapter we use the following idea. If the production of pollutants would be an effect of entrance of the medium and exciting resonances in spaghetti region, it would happen both in the case of EIT and in the case of off-resonant two-photon Raman excitation. Therefore, by exploring on-resonance and off-resonance cases in the experiment we can conclude whether the proposed mechanism is wrong or not. To set a reference point in the amount of registered ions, we decrease the size of the cloud below a blockade radius such that $\sigma_R = 10 \mu\text{m}$ and $\sigma_L = 6 \mu\text{m}$ while $r_b = 21 \mu\text{m}$ at $111S$. To do this we use an additional dipole trap beam called dimple to tighten the trap (see for details [106]). In this case only a single Rydberg excitation at $111S$ state must fit in the cloud because of the blockade effect.

The results of the measurement are shown in Fig. 5.13. Firstly, we can see that for the off-resonant case with 100 MHz detuning from the intermediate state and two-photon detuning from the Rydberg state equal to zero, the amount of registered ions is saturating at around 1 with increasing input photon rate. It, actually, says that we excite only $111S$ state that completely blockades the cloud and there is no pollutant formation. Next, we shift the laser intermediate state detuning into the dispersive regime at 15 MHz and park out laser at the minimum of transmission at the dispersive feature. We observe that in this case the registered amount of ions is not saturating at 1 like in the case of 100 MHz detuning, but rather growing with input photon rate. Finally, in the on-resonant case we observe the same behavior as before: the amount of registered ions is growing parabolic in the beginning and then it starts to bend like it is going to saturate at some point. We again reach 14 ions at 70 photons/ μs , which is, of course, much higher than what can fit in the cloud at $111S$ state, indicating that pollutants do not blockade each other. Basically, this observation clearly shows that the discussed hypothesis is inconsistent in describing the experimental observations.

In general, this measurement indicates that the process of pollutants formation happens when we excite EIT and, probably, is coming from polariton propagation through the cloud.

5.8 Outlook and conclusion

In this work we have studied the propagation of Rydberg polaritons through the atomic cloud at high input probe photon rates. The initial intention was to find out whether we can observe the formation of the crystallization of single photons, described in [43, 44] and to study the high-intensity sector of physics of dissipative Rydberg-EIT media. Our work has shown, that on one side, we observe the effects that qualitatively agree with the theoretical predictions, what could indicate the beginning of ordering of single photons transmitted through the cloud. On the other hand, we have discovered the nonlinear growth of

the ion signal registered in the experiment with the input probe photon rate, revealing anomalously high values for high photon rates. Our studies show that this behavior originates from the presence of pollutant Rydberg atoms in the cloud, that are in different states from the initial Rydberg excitation at $111S$, and which do not blockade each other, but blockade Rydberg atoms in $111S$. The proposed possible mechanism of pollutants formation was disproved in the experiment, which left us without real understanding of physics behind Rydberg pollution. However, the fact that this effect is observed only in the case when we excite EIT in the medium, and not in the case of two-photon Raman excitation of Rydberg atoms, suggests that formation of Rydberg pollutants originates from the propagation of polaritons through the medium.

The importance of the understanding the effect of Rydberg pollutants is dictated by the fact that it could put a restriction on all the future experiments in the field of Rydberg quantum optics. The presence of undesired Rydberg atoms in the different states would affect the fidelities of all quantum operations in the system. We collaborate with the theory groups of Alexey Gorshkov and Darrick Chang to find out what is going on in our experiment. Apart from adjusting of the existent theory we try to find new ideas to explain the pollutants. One essential point is the dimensionality of the system. So, analytic theory was developed only for the case of one dimensional polariton propagation and only valid in this case. In our system the blockade radius at $111S$ Rydberg state $r_b = 21 \mu\text{m}$ is more than twice bigger than the transversal $1/e$ radius of the cloud $\sigma_R = 9 \mu\text{m}$ which should be enough to establish a one dimensional condition for polariton propagation. But, of course, this condition is not fully strict.

The preliminary finding from the Darrick Chang group is that adding a pollution state where the Rydberg atom can decay into and decay out of into the ground state, with the same blockade but not participating in EIT, can result in the prediction for pulse shapes similar to what is observed in the experiment. The real explanation for adding such level is unclear, but it again might be connected with three dimensional physics of polaritons. In our system the transverse OD for the photons scattered in the middle of the cloud is bigger than 1, what would result, for example, in events when scattered photons become Rydberg polaritons in transverse directions and, then, Rydberg atoms [173]. This in itself would not explain our data, but such radiation-trapping-like process could be considered as a starting point that helps to get the actual pollution process, which involves creating Rydberg atoms in different states decoupled from the control light, started. Just the presence of many Rydberg atoms in the cloud with all possible angles between pairs of them increases the chance of state-changing Rydberg-Rydberg collisions or resonant excitation of other pair states at certain distances from Rydberg seeds. The radiative trapping would set the creation rate of the pollutant atoms and this would define also the decay rate into the non-interacting Rydberg states. The preliminary and very simplified simulations of the radiation trapping process show that the rates with which radiation trapping happens are similar to the decay rate that was used to match the pulse shapes in the simulation with 4-level system.

This is a good indication in general, but one has to think about few difficult

points, such as parabolic behavior of the ion signal, which would imply that state-changing collisions or excitation of anti-blockade resonances depend on the number of already present pollutants. Another point would be comparison between on-resonant and off-resonant cases, and understanding why we observe this effect only in the case of EIT.

Alternatively, it is even possible to think about the three-body mechanism of excitation of new Rydberg atoms in the case when two Rydberg excitations would sit quite close to each other, though this idea is speculative.

All these show the importance of doing simulations in three dimensional cloud. The approach of Darrick Chang's group has a potential to be extended into 3D and this would be a next step in the work. Finally, we believe that this is an important topic and we will keep working on further investigation of the Rydberg pollution effect.

Chapter 6

The final notes

Outlook for the discussed work

The results obtained during the work on this dissertation bring up various directions for further research.

First, the shown possibility to spatially image a beam photon by photon opens broad opportunities for further studies of many-body physics with strongly-interacting photons. Integration of this method into the new version of the experiment is almost straightforward, and will just require appropriate treatment of stray lights. Thus, designing general isolation from stray lights, finding a proper set of filters and accurately characterizing their impact on a beam mode should become next steps for work in this direction.

In this context, spatial imaging of single photons transmitted through the cold atomic cloud under EIT condition opens opportunities to study nonlinear wave phenomena, such as spatial solitons and modulation instability of photon density mediated by Rydberg-Rydberg interaction [50]. As well, investigating anisotropy of Rydberg-Rydberg interaction [81, 47] is both of high fundamental and applied interest, because it can become another tuning knob in the engineering of polariton interactions [174] and experiments on Rydberg dressing [175, 48].

The work on EIT with ultralong-range Rydberg molecules changes the current established opinion which assumes that already the dimer fraction should be small for coherent operation, which restricts the atomic density to $< 10^{12} \text{ cm}^{-3}$. We estimate that an increase in blockaded optical depth by a factor 5...10 should be possible, which would significantly boost the overall fidelity of the single-photon switches and transistors [53, 54]. From fundamental point of view it would be interesting to employ microscopic molecular potentials calculated from Rydberg wave function and try to numerically calculate the time evolution of the system [167].

Experiments on propagation of Rydberg polaritons through dissipative Rydberg-EIT medium at large photon rates revealed the presence of new obscure effect of Rydberg pollution. The main effort has to be devoted towards full understanding of this effect. The work with our theoretician collaborators is going on, and the next step for now is to simulate the polariton propagation with additional decay level from Rydberg state to find out if we can achieve good agreement with the experiment data. A more long-term step is simulation of polariton propagation through three dimensional atomic cloud, that can really help in understanding of the underlying process. Based on the outcome of

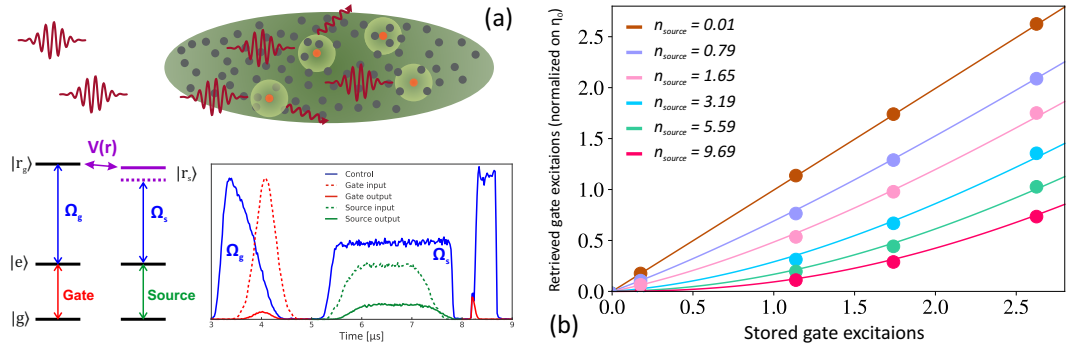


FIGURE 6.1: (a) The schematic of a single photon transistor realization. We ramp the gate control field Ω_g (solid blue line on the right) down to zero during the gate probe pulse propagating through the medium (dashed red line). It allows to store multiple gate excitations in the cloud while some part of the gate pulse is still transmitted (solid red line on the left). Next, we send source photons to the cloud (dashed green line) under EIT condition with control field Ω_s (solid blue line in the middle). From the transmitted source pulse (solid green line in the center) we can calculate the amount of scattered source photons. Finally, we turn the gate control field Ω_g back on (solid blue line on the right) and retrieve gate photons out of the cloud (solid red line on the right). (b) Retrieved gate photons normalized on storage and retrieval efficiency measured as a function of stored gate excitations. It shows proof-of-principle of a single photon subtractor. The errorbars are smaller than the shown markers.

such simulations, one should think on further experiments that could prove or disprove the simulation results.

Observation of a photon crystal should become easier once the effect of Rydberg pollution is understood and one can design an experiment to eliminate it. Still, a fundamental challenge here is to reach the highest OD per blockade possible, to be able to observe few oscillations in a correlation function [44].

Photon subtraction via induced many-body decoherence

In the course of the work on this PhD thesis the set of experiments investigating a single photon transistor with multiple gate excitations were performed. The driving force for these studies was a recent paper from the group of Thomas Pohl that discussed the process of decoherence of a stored gate excitation inside of an atomic cloud which is caused by multi-photon scattering of source photons [54]. This decoherence mechanism inhibits the retrieval of a gate photon and, thus, restricts the coherent operation of a single photon transistor. Following this work, the group of Thomas Pohl proposed to use multiple gate excitations in transistor operation, which could initiate a form of decoherence protection and improve a coherent operation of a transistor.

We start the discussion with an explanation of a single-photon transistor with gate photon read-out (see for details [33, 35]). The idea is that we would like to control transmission of source photons by a single or several gate photons. For this, we store multiple gate photons in the form of a collective spin wave in

the Rydberg state $|r_g\rangle$ (see Fig. 6.1(a)). Next, we send source photons under EIT condition with a different state $|r_s\rangle$ to propagate through the cloud. Due to the Rydberg-Rydberg interaction between $|r_g\rangle$ and $|r_s\rangle$, the EIT condition for source photons is destroyed and they get scattered onto a dissipative two-level medium in blockade volumes around gate excitations. Finally, we retrieve gate photons out of the cloud.

The intrinsic decoherence mechanism in such a scheme arises from the following: when we store a single gate photon in the cloud, scattering of source photons on it results into projective measurement of a spin wave state, in other words, it spatially localizes the stored excitation. This destroys the spatial coherences of the stored excitation and, thus, prevents its retrieval. In the case when there are several spatially distinct gate excitations stored in the cloud it is possible to turn this situation around and achieve many-body decoherence protection between multiple gate excitations. If OD per blockade is high and a single Rydberg excitation can completely blockade the cloud in transverse directions, the first stored gate excitation in the cloud scatters near all the source photons. All subsequent stored gate excitations do not participate in the scattering process and their spatial coherences are unaffected. Even though, one gate excitation cannot be retrieved from the cloud, the overall retrieval efficiency can be enhanced because of the induced protection for other gate excitations. Looking at this process from the other side reveals a robust mechanism for a single photon subtraction, because the first gate excitation gets stuck in the cloud and upon retrieval a single photon is missing in the gate field.

Callum Murray and Thomas Pohl could solve this quantum many-body problem and achieve rigorous understanding of the underlying dissipative many-body dynamics. Obtained many-body density matrix solution allows to build an intuitive model describing the process of gate photon retrieval (for the detailed theoretical analysis we refer to the joint publication [176]). To test this model we perform an experiment of the described scheme.

We start by trapping 9×10^4 ^{87}Rb atoms into an optical dipole trap resulting in a cigar shaped cloud at 4 μK with $1/e$ radial and axial radii of $\sigma_R = 13 \mu\text{m}$ and $\sigma_L = 42 \mu\text{m}$, respectively. All the atoms are first optically pumped into the $|g\rangle = |5S_{1/2}, F = 2, m_F = 2\rangle$ state. Gate photons are coupled to the Rydberg state $|r_g\rangle = |68S_{1/2}, m_J = 1/2\rangle$ via EIT by applying a weak 780 nm probe field which drives the transition between the ground state $|g\rangle$ and intermediate state $|e\rangle = |5P_{3/2}, F = 3, m_F = 3\rangle$, and a strong counterpropagating 480 nm control field Ω_g which drives the transition between $|e\rangle$ and $|r_g\rangle$. To store gate photons into the cloud we ramp down the gate control field Ω_g to zero while the gate probe pulse is propagating through the cloud (see the pulse scheme in Fig. 6.1(a)). This leaves a system of n_{gate} photons on average, which can be determined ionizing the cloud and measuring the number of produced ions. Then we probe the stored gate excitations by monitoring the transmission of the source photons coupled via EIT to the Rydberg state $|r_s\rangle = |66S_{1/2}, m_J = 1/2\rangle$ in the same manner as the gate photons. The total storage time of the gate photons is 4 μs after which we read them out of the cloud by turning Ω_g back on.

The realization of a proof-of-principle of a single photon subtraction is shown in Fig. 6.1(b) where we plot the amount of retrieved gate photons normalized

on the storage and retrieval efficiency as a function of amount of stored gate excitations for different number of sent source photons n_{source} . We indeed can observe the process of photon subtraction. Although, it is seen that for higher source intensities the number of subtracted photons exceeds one, which happens due to imperfect scattering conditions. The theoretical prediction (solid lines) reveals the scattering probability per gate excitation $p = 0.68$ (where $p = 1$ is an ideal case of a strong scattering limit). It means that the first gate excitation does not scatter all the passing source photons and some of them penetrate deeper into the medium and destroy the spatial coherences of other gate excitations. In the situation with $p < 1$ one could think about finding an optimum source field intensity for subtracting exactly one gate excitation. Thus, a source field becomes an additional controlling knob for a photon subtraction. In addition, an access to much larger absorption probabilities makes this scheme more advantageous compared to other single photon subtractor realizations [177, 36].

The detailed explanation of the developed theory and analysis of a single photon transistor and a single photon subtraction performances will be given in upcoming joint publication prepared by Murray et al. [176].

Appendix A

Dephasing of a spin wave induced by atomic random motion

In the Chapter 4 we introduced a dephasing of a stored spin wave induced by a thermal atomic motion in the cloud. We will give a short explanation of such a dephasing here [178, 179, 180].

Let's consider a spin wave created by an excitation of a Rydberg atom in the cold atomic cloud at the time t_0 :

$$\Psi = \frac{1}{\sqrt{N}} \sum_j e^{i\Delta\mathbf{k}\mathbf{x}_j(t_0)} |g_1, \dots, r_j, \dots, g_N\rangle \quad (\text{A.1})$$

where N is a full amount of atoms in the cloud, $\Delta\mathbf{k} = \mathbf{k}_c + \mathbf{k}_p$ is a sum of the wave vectors of EIT light fields, \mathbf{x}_j is a position of an atom j . During some time interval δt atoms in the cloud are moving which leads to a perturbation on the phase of the spin wave. Assume the j th atom moves during δt to the new position $\mathbf{x}_j(t_0 + \delta t) = \mathbf{x}_j(t_0) + \mathbf{v}_j\delta t$. Therefore, the spin wave evolves into

$$\Psi_E = \frac{1}{\sqrt{N}} \sum_j e^{i\Delta\mathbf{k}\mathbf{x}_j(t_0+\delta t)} |g_1, \dots, r_j, \dots, g_N\rangle \quad (\text{A.2})$$

The retrieval efficiency of the spin wave after a time δt is proportional to the overlap between the original spin wave and dephased one

$$\eta(\delta t) \sim |\langle\Psi|\Psi_E\rangle| = \left| \frac{1}{\sqrt{N}} \sum_j e^{i\Delta\mathbf{k}\mathbf{v}_j\delta t} \right|^2 = \left| \int f(v) e^{i\Delta\mathbf{k}\mathbf{v}_j\delta t} dv \right|^2, \quad (\text{A.3})$$

where $f(v)$ is the velocity distribution. Basically we see, that with increase in the time interval δt , the projection of the perturbed spin wave on the original one decreases, because the phase of the spin wave undergoes random fluctuations originating from the random motion of atoms. Choosing a Boltzmann distribution at the temperature T - $f(v) \sim \exp(-mv^2/2k_B T)$, we can perform integration over all the possible velocities which results in

$$\eta(\delta t) \sim \exp(-\delta t^2/\tau_T^2) \quad (\text{A.4})$$

with the lifetime $\tau_T = (\Delta k v_s)^{-1}$, $v_s = \sqrt{k_B T/m}$ the one-dimensional average speed, and k_B is the Boltzmann constant.

Bibliography

- [1] R. Boyd. *Nonlinear Optics*. New York: Academic Press, 1992.
- [2] M. A. Nielsen and I. L. Chuang. *Quantum Computation and Quantum Information*. Cambridge: CUP, 2005.
- [3] Alain Aspect, Philippe Grangier, and Gérard Roger. “Experimental Tests of Realistic Local Theories via Bell’s Theorem”. In: *Phys. Rev. Lett.* 47 (7 1981), pp. 460–463.
- [4] Alain Aspect, Jean Dalibard, and Gérard Roger. “Experimental Test of Bell’s Inequalities Using Time-Varying Analyzers”. In: *Phys. Rev. Lett.* 49 (25 1982), pp. 1804–1807.
- [5] D. P. DiVincenzo, D. Bacon, J. Kempe, G. Burkard, and K. B. Whaley. “Universal quantum computation with the exchange interaction”. In: *Nature* 408.6810 (2000), pp. 339–342.
- [6] P. Michler, A. Kiraz, C. Becher, W. V. Schoenfeld, P. M. Petroff, Lidong Zhang, E. Hu, and A. Imamoglu. “A Quantum Dot Single-Photon Turnstile Device”. In: *Science* 290.5500 (2000), pp. 2282–2285.
- [7] C. W. Chou, S. V. Polyakov, A. Kuzmich, and H. J. Kimble. “Single-Photon Generation from Stored Excitation in an Atomic Ensemble”. In: *Phys. Rev. Lett.* 92 (21 2004), p. 213601.
- [8] J. McKeever, A. Boca, A. D. Boozer, R. Miller, J. R. Buck, A. Kuzmich, and H. J. Kimble. “Deterministic Generation of Single Photons from One Atom Trapped in a Cavity”. In: *Science* 303.5666 (2004), pp. 1992–1994.
- [9] A. Imamoglu, H. Schmidt, G. Woods, and M. Deutsch. “Strongly Interacting Photons in a Nonlinear Cavity”. In: *Phys. Rev. Lett.* 79 (8 1997), pp. 1467–1470.
- [10] S. E. Harris and Lene Vestergaard Hau. “Nonlinear Optics at Low Light Levels”. In: *Phys. Rev. Lett.* 82 (23 1999), pp. 4611–4614.
- [11] Darrick E. Chang, Vladan Vuletic, and Mikhail D. Lukin. “Quantum nonlinear optics - photon by photon”. In: *Nature Photonics* 8.9 (2014), pp. 685–694.
- [12] K. M. Birnbaum, A. Boca, R. Miller, A. D. Boozer, T. E. Northup, and H. J. Kimble. “Photon blockade in an optical cavity with one trapped atom”. In: *Nature* 436 (2005), p. 87.
- [13] T. Wilk, S. C. Webster, A. Kuhn, and G. Rempe. “Single-Atom Single-Photon Quantum Interface”. In: *Science* 317 (2007), pp. 488–490.

- [14] I. Schuster, A. Kubanek, A. Fuhrmanek, T. Puppe, P. W. H. Pinkse, K. Murr, and G. Rempe. “Nonlinear spectroscopy of photons bound to one atom”. In: *Nature Physics* 4.5 (2008), pp. 382–385.
- [15] Barak Dayan, A. S. Parkins, Takao Aoki, E. P. Ostby, K. J. Vahala, and H. J. Kimble. “A Photon Turnstile Dynamically Regulated by One Atom”. In: *Science* 319.5866 (2008), pp. 1062–1065.
- [16] Ilya Fushman, Dirk Englund, Andrei Faraon, Nick Stoltz, Pierre Petroff, and Jelena Vučković. “Controlled Phase Shifts with a Single Quantum Dot”. In: *Science* 320.5877 (2008), pp. 769–772.
- [17] Matthew Pelton, Charles Santori, Jelena Vučković, Bingyang Zhang, Glenn S. Solomon, Jocelyn Plant, and Yoshihisa Yamamoto. “Efficient Source of Single Photons: A Single Quantum Dot in a Micropost Microcavity”. In: *Phys. Rev. Lett.* 89 (23 2002), p. 233602.
- [18] Andrei Faraon, Paul E. Barclay, Charles Santori, Kai-Mei C. Fu, and Raymond G. Beausoleil. “Resonant enhancement of the zero-phonon emission from a colour centre in a diamond cavity”. In: *Nat Photon* 5.5 (2011), pp. 301–305.
- [19] Birgit J. M. Hausmann, Brendan Shields, Qimin Quan, Patrick Maletinsky, Murray McCutcheon, Jennifer T. Choy, Tom M. Babinec, Alexander Kubanek, Amir Yacoby, Mikhail D. Lukin, and Marko Loncar. “Integrated Diamond Networks for Quantum Nanophotonics”. In: *Nano Letters* 12.3 (2012). PMID: 22339606, pp. 1578–1582.
- [20] Andreas Reiserer, Stephan Ritter, and Gerhard Rempe. “Nondestructive Detection of an Optical Photon”. In: *Science* 342.6164 (2013), pp. 1349–1351.
- [21] T. G. Tiecke, J. D. Thompson, N. P. de Leon, L. R. Liu, V. Vuletic, and M. D. Lukin. “Nanophotonic quantum phase switch with a single atom”. In: *Nature* 508.7495 (2014). Letter, pp. 241–244.
- [22] Andreas Reiserer, Norbert Kalb, Gerhard Rempe, and Stephan Ritter. “A quantum gate between a flying optical photon and a single trapped atom”. In: *Nature* 508.7495 (2014), pp. 237–240.
- [23] Bastian Hacker, Stephan Welte, Gerhard Rempe, and Stephan Ritter. “A photon–photon quantum gate based on a single atom in an optical resonator”. In: *Nature* 536.7615 (2016), pp. 193–196.
- [24] D. F. Phillips, A. Fleischhauer, A. Mair, R. L. Walsworth, and M. D. Lukin. “Storage of Light in Atomic Vapor”. In: *Phys. Rev. Lett.* 86 (5 2001), pp. 783–786.
- [25] Chien Liu, Zachary Dutton, Cyrus H. Behroozi, and Lene Vestergaard Hau. “Observation of coherent optical information storage in an atomic medium using halted light pulses”. In: *Nature* 409.6819 (2001), pp. 490–493.

- [26] Wenlan Chen, Kristin M. Beck, Robert Bücke, Michael Gullans, Mikhail D. Lukin, Haruka Tanji-Suzuki, and Vladan Vuletić. “All-Optical Switch and Transistor Gated by One Stored Photon”. In: *Science* 341.6147 (2013), pp. 768–770.
- [27] A. V. Gorshkov, J. Otterbach, M. Fleischhauer, T. Pohl, and M. D. Lukin. “Photon-Photon Interactions via Rydberg Blockade”. In: *Phys. Rev. Lett.* 107 (2011), p. 133602.
- [28] J. D. Pritchard, D. Maxwell, A. Gauguet, K. J. Weatherill, M. P. A. Jones, and C. S. Adams. “Cooperative Atom-Light Interaction in a Blockaded Rydberg Ensemble”. In: *Phys. Rev. Lett.* 105 (19 2010), p. 193603.
- [29] Y. O. Dudin and A. Kuzmich. “Strongly Interacting Rydberg Excitations of a Cold Atomic Gas”. In: *Science* 336 (2012), pp. 887–889.
- [30] D. Maxwell, D. J. Szwer, D. Paredes-Barato, H. Busche, J. D. Pritchard, A. Gauguet, K. J. Weatherill, M. P. A. Jones, and C. S. Adams. “Storage and Control of Optical Photons Using Rydberg Polaritons”. In: *Phys. Rev. Lett.* 110 (2013), p. 103001.
- [31] L. Li, Y. O. Dudin, and A. Kuzmich. “Entanglement between light and an optical atomic excitation”. In: *Nature* 498 (2013), pp. 466–469.
- [32] Simon Baur, Daniel Tiarks, Gerhard Rempe, and Stephan Dürr. “Single-Photon Switch Based on Rydberg Blockade”. In: *Phys. Rev. Lett.* 112 (2014), p. 073901.
- [33] H. Gorniaczyk, C. Tresp, J. Schmidt, H. Fedder, and S. Hofferberth. “Single-Photon Transistor Mediated by Interstate Rydberg Interactions”. In: *Phys. Rev. Lett.* 113 (2014), p. 053601.
- [34] Daniel Tiarks, Simon Baur, Katharina Schneider, Stephan Dürr, and Gerhard Rempe. “Single-Photon Transistor Using a Förster Resonance”. In: *Phys. Rev. Lett.* 113 (2014), p. 053602.
- [35] H. Gorniaczyk, C. Tresp, P. Bienias, A. Paris-Mandoki, W. Li, I. Mirgorodskiy, H. P. Büchler, I. Lesanovsky, and S. Hofferberth. “Enhancement of Rydberg-mediated single-photon nonlinearities by electrically tuned Förster resonances”. In: *Nature Communications* 7 (2016), p. 12480.
- [36] C. Tresp, C. Zimmer, I. Mirgorodskiy, H. Gorniaczyk, A. Paris-Mandoki, and S. Hofferberth. “Single-Photon Absorber Based on Strongly Interacting Rydberg Atoms”. In: *Phys. Rev. Lett.* 117 (2016), p. 223001.
- [37] Valentina Parigi, Erwan Bimbard, Jovica Stanojevic, Andrew J. Hilliard, Florence Nogrette, Rosa Tualle-Brouri, Alexei Ourjoumtsev, and Philippe Grangier. “Observation and Measurement of Interaction-Induced Dispersive Optical Nonlinearities in an Ensemble of Cold Rydberg Atoms”. In: *Phys. Rev. Lett.* 109 (2012), p. 233602.
- [38] Daniel Tiarks, Steffen Schmidt, Gerhard Rempe, and Stephan Dürr. “Optical π phase shift created with a single-photon pulse”. In: *Science Advances* 2 (2016), e1600036.

- [39] Jeff D. Thompson, Travis L. Nicholson, Qi-Yu Liang, Sergio H. Cantu, Aditya V. Venkatramani, Soonwon Choi, Ilya A. Fedorov, Daniel Viscor, Thomas Pohl, Mikhail D. Lukin, and Vladan Vuletić. “Symmetry-protected collisions between strongly interacting photons”. In: *Nature* 542 (2017), pp. 206–209.
- [40] O. Firstenberg, T. Peyronel, Q. Liang, A. V. Gorshkov, M. D. Lukin, and V. Vuletić. “Attractive photons in a quantum nonlinear medium”. In: *Nature* 502 (2013), pp. 71–75.
- [41] D. E. Chang, V. Gritsev, G. Morigi, V. Vuletic, M. D. Lukin, and E. A. Demler. “Crystallization of strongly interacting photons in a nonlinear optical fibre”. In: *Nature Physics* 4.11 (2008), pp. 884–889.
- [42] Johannes Otterbach, Matthias Moos, Dominik Muth, and Michael Fleischhauer. “Wigner Crystallization of Single Photons in Cold Rydberg Ensembles”. In: *Phys. Rev. Lett.* 111 (11 2013), p. 113001.
- [43] Alexey V. Gorshkov, Rejish Nath, and Thomas Pohl. “Dissipative Many-Body Quantum Optics in Rydberg Media”. In: *Phys. Rev. Lett.* 110 (2013), p. 153601.
- [44] Emil Zeuthen, Michael J. Gullans, Mohammad F. Maghrebi, and Alexey V. Gorshkov. “Correlated photon dynamics in dissipative Rydberg media”. In: *Phys. Rev. Lett.* (*in press*); *arXiv:1608.06068* (2017).
- [45] Krzysztof Jachymski, Przemysław Bienias, and Hans Peter Büchler. “Three-Body Interaction of Rydberg Slow-Light Polaritons”. In: *Phys. Rev. Lett.* 117 (2016), p. 053601.
- [46] M. J. Gullans, J. D. Thompson, Y. Wang, Q.-Y. Liang, M. D. Lukin, and A. V. Gorshkov. “Effective Field Theory for Rydberg Polaritons”. In: *Phys. Rev. Lett.* 117 (11 2016), p. 113601.
- [47] C. Tresp, P. Bienias, S. Weber, H. Gorniaczyk, I. Mirgorodskiy, H. P. Büchler, and S. Hofferberth. “Dipolar Dephasing of Rydberg *D*-State Polaritons”. In: *Phys. Rev. Lett.* 115 (8 2015), p. 083602.
- [48] R. M. W. van Bijnen and T. Pohl. “Quantum Magnetism and Topological Ordering via Rydberg Dressing near Förster Resonances”. In: *Phys. Rev. Lett.* 114 (24 2015), p. 243002.
- [49] Henning Labuhn, Daniel Barredo, Sylvain Ravets, Sylvain de Léséleuc, Tommaso Macrì, Thierry Lahaye, and Antoine Browaeys. “Tunable two-dimensional arrays of single Rydberg atoms for realizing quantum Ising models”. In: *Nature* 534.7609 (2016). Letter, pp. 667–670.
- [50] S. Sevincli, N. Henkel, C. Ates, and T. Pohl. “Nonlocal Nonlinear Optics in Cold Rydberg Gases”. In: *Phys. Rev. Lett.* 107 (15 2011), p. 153001.
- [51] D. Jaksch, J. I. Cirac, P. Zoller, S. L. Rolston, R. Côté, and M. D. Lukin. “Fast quantum gates for neutral atoms”. In: *Physical Review Letters* 85.10 (2000), pp. 2208–2211.
- [52] Chris H. Greene, A. S. Dickinson, and H. R. Sadeghpour. “Creation of Polar and Nonpolar Ultra-Long-Range Rydberg Molecules”. In: *Phys. Rev. Lett.* 85 (12 2000), pp. 2458–2461.

- [53] Weibin Li and Igor Lesanovsky. “Coherence in a cold-atom photon switch”. In: *Phys. Rev. A* 92 (2015), p. 043828.
- [54] C. R. Murray, A. V. Gorshkov, and T. Pohl. “Many-body decoherence dynamics and optimized operation of a single-photon switch”. In: *New Journal of Physics* 18 (2016), p. 092001.
- [55] T. F. Gallagher. *Rydberg Atoms*. Cambridge U, 1994.
- [56] Robert Löw, Hendrik Weimer, Johannes Nipper, Jonathan B Balewski, Björn Butscher, Hans Peter Büchler, and Tilman Pfau. “An experimental and theoretical guide to strongly interacting Rydberg gases”. In: *Journal of Physics B: Atomic, Molecular and Optical Physics* 45.11 (2012), p. 113001.
- [57] M. Saffman, T. G. Walker, and K. Mølmer. “Quantum information with Rydberg atoms”. In: *Rev. Mod. Phys.* 82 (2010), p. 2313.
- [58] C-J. Lorenzen and K. Niemax. “Quantum Defects of the $n^2P_{1/2,3/2}$ level series in $^{39}\text{K I}$ and $^{85}\text{Rb I}$ ”. In: *Physica Scripta* 27.4 (1983), p. 300.
- [59] Wenhui Li, I. Mourachko, M. W. Noel, and T. F. Gallagher. “Millimeter-wave spectroscopy of cold Rb Rydberg atoms in a magneto-optical trap: Quantum defects of the ns, np, and nd series”. In: *Physical Review A* 67.5 (2003), p. 052502.
- [60] Jianing Han, Yasir Jamil, D. V. L. Norum, Paul J. Tanner, and T. F. Gallagher. “Rb nf quantum defects from millimeter-wave spectroscopy of cold ^{85}Rb Rydberg atoms”. In: *Physical Review A - Atomic, Molecular, and Optical Physics* 74.5 (2006), pp. 2–5.
- [61] K. Afrousheh, P. Bohlouli-Zanjani, J. A. Petrus, and J. D. D. Martin. “Determination of the ^{85}Rb ng -series quantum defect by electric-field-induced resonant energy transfer between cold Rydberg atoms”. In: *Physical Review A - Atomic, Molecular, and Optical Physics* 74.6 (2006), pp. 2–5.
- [62] Markus Mack, Florian Karlewski, Helge Hattermann, Simone Höckh, Florian Jessen, Daniel Cano, and József Fortágh. “Measurement of absolute transition frequencies of ^{87}Rb to nS and nD Rydberg states by means of electromagnetically induced transparency”. In: *Physical Review A - Atomic, Molecular, and Optical Physics* 83.5 (2011), pp. 1–8.
- [63] M. S. O’Sullivan and B. P. Stoicheff. “Scalar polarizabilities and avoided crossings of high Rydberg states in Rb”. In: *Physical Review A* 31.4 (1985), pp. 2718–2720.
- [64] Kilian Singer, Jovica Stanojevic, Matthias Weidemüller, and Robin Côté. “Long-range interactions between alkali Rydberg atom pairs correlated to the n s– n s, n p– n p and n d– n d asymptotes”. In: *Journal of Physics B: Atomic, Molecular and Optical Physics* 38.2 (2005), S295–S307.

- [65] I. I. Beterov, I. I. Ryabtsev, D. B. Tretyakov, and V. M. Entin. “Quasi-classical calculations of blackbody-radiation-induced depopulation rates and effective lifetimes of Rydberg nS , nP , and nD alkali-metal atoms with $n \leq 80$ ”. In: *Physical Review A - Atomic, Molecular, and Optical Physics* 79.5 (2009), pp. 1–11.
- [66] M. Marinescu, H. R. Sadeghpour, and A. Dalgarno. “Dispersion coefficients for alkali-metal dimers”. In: *Phys. Rev. A* 49 (2 1994), pp. 982–988.
- [67] Ali Sanayei, Nils Schopohl, Jens Grimm, Markus Mack, Florian Karlewski, and József Fortágh. “Quasiclassical quantum defect theory and the spectrum of highly excited rubidium atoms”. In: *Physical Review A - Atomic, Molecular, and Optical Physics* 91.3 (2015), pp. 1–5.
- [68] Myron L. Zimmerman, Michael G. Littman, Michael M. Kash, and Daniel Kleppner. “Stark structure of the Rydberg states of alkali-metal atoms”. In: *Phys. Rev. A* 20 (6 1979), pp. 2251–2275.
- [69] Chris H. Greene and Mireille Aymar. “Spin-orbit effects in the heavy alkaline-earth atoms”. In: *Phys. Rev. A* 44 (3 1991), pp. 1773–1790.
- [70] C. E. Theodosiou. “Lifetimes of alkali-metal - atom Rydberg states”. In: *Physical Review A* 30.6 (1984), p. 2881.
- [71] S. A. Bhatti, C. L. Cromer, and W. E. Cooke. “Analysis of the Rydberg character of the $5d7d^1D_2$ state of barium”. In: *Physical Review A* 24.1 (1981), pp. 161–165.
- [72] Robert W. Schmieder. “Matrix Elements of the Quadratic Stark Effect on Atoms with Hyperfine Structure”. In: *American Journal of Physics* 40.2 (1972), p. 297.
- [73] M. D. Lukin, M. Fleischhauer, R. Côté, L. M. Duan, D. Jaksch, J. I. Cirac, and P. Zoller. “Dipole blockade and quantum information processing in mesoscopic atomic ensembles.” In: *Physical review letters* 87.3 (2001), p. 037901.
- [74] Thibault Peyronel, Ofer Firstenberg, Qi-Yu Liang, Sebastian Hofferberth, Alexey V. Gorshkov, Thomas Pohl, Mikhail D. Lukin, and Vladan Vuletić. “Quantum nonlinear optics with single photons enabled by strongly interacting atoms.” In: *Nature* 488.7409 (2012), pp. 57–60.
- [75] Y. O. Dudin and A. Kuzmich. “Strongly Interacting Rydberg Excitations of a Cold Atomic Gas”. In: *Science* 336.6083 (2012), pp. 887–889.
- [76] A. Reinhard, T. Cubel Liebisch, B. Knuffman, and G. Raithel. “Level shifts of rubidium Rydberg states due to binary interactions”. In: *Physical Review A - Atomic, Molecular, and Optical Physics* 75.3 (2007), pp. 1–12.
- [77] Daniel Comparat and Pierre Pillet. “Dipole blockade in a cold Rydberg atomic sample”. In: *J. Opt. Soc. Am. B* 27.6 (2010), A208–A232.
- [78] M. R. Flannery, D. Vranceanu, and V. N. Ostrovsky. “Long-range interaction between polar Rydberg atoms”. In: *Journal of Physics B: Atomic, Molecular and Optical Physics* 38.2 (2005), S279–S293.

- [79] J. Stanojevic, R. Côté, D. Tong, S. M. Farooqi, E. E. Eyler, and P. L. Gould. “Long-range Rydberg-Rydberg interactions and molecular resonances”. In: *The European Physical Journal D - Atomic, Molecular, Optical and Plasma Physics* 40.1 (2006), pp. 3–12.
- [80] J. Stanojevic, R. Côté, D. Tong, E. E. Eyler, and P. L. Gould. “Long-range potentials and $(n - 1)d + ns$ molecular resonances in an ultracold Rydberg gas”. In: *Phys. Rev. A* 78 (5 2008), p. 052709.
- [81] Thad G. Walker and M. Saffman. “Consequences of Zeeman degeneracy for the van der Waals blockade between Rydberg atoms”. In: *Physical Review A - Atomic, Molecular, and Optical Physics* 77.3 (2008), pp. 1–18.
- [82] Sebastian Weber, Christoph Tresp, Henri Menke, Alban Urvoy, Ofer Firstenberg, Hans Peter Büchler, and Sebastian Hofferberth. “Tutorial: Calculation of Rydberg interaction potentials”. In: *arXiv:1612.08053* (2016).
- [83] A. Urvoy, F. Ripka, I. Lesanovsky, D. Booth, J. P. Shaffer, T. Pfau, and R. Löw. “Strongly Correlated Growth of Rydberg Aggregates in a Vapor Cell”. In: *Phys. Rev. Lett.* 114 (20 2015), p. 203002.
- [84] A. Derevianko, W. R. Johnson, M. S. Safronova, and J. F. Babb. “High-Precision Calculations of Dispersion Coefficients, Static Dipole Polarizabilities, and Atom-Wall Interaction Constants for Alkali-Metal Atoms”. In: *Phys. Rev. Lett.* 82 (18 1999), pp. 3589–3592.
- [85] Michael Fleischhauer, Atac Imamoglu, and Jonathan P. Marangos. “Electromagnetically induced transparency: Optics in coherent media”. In: *Rev Mod Phys* 77.2 (2005), pp. 633–673.
- [86] M. Fleischhauer and M. D. Lukin. “Dark-state polaritons in electromagnetically induced transparency”. In: *Phys. Rev. Lett.* 84.22 (2000), pp. 5094–5097.
- [87] C. Cohen-Tannoudji, G. Grynberg, and J. Dupont-Roc. *Atom-Photon Interactions: Basic Processes and Applications*. New York: Wiley, 1992.
- [88] Julio Gea-Banacloche, Yong-qing Li, Shao-zheng Jin, and Min Xiao. “Electromagnetically induced transparency in ladder-type inhomogeneously broadened media: Theory and experiment”. In: *Phys. Rev. A* 51 (1 1995), pp. 576–584.
- [89] Daniel Adam Steck. *Quantum and Atom Optics*. University of Oregon: lecture notes, published online.
- [90] L.V. Hau, S.E. Harris, Z. Dutton, and C.H. Behroozi. “Light speed reduction to 17 metres per second in an ultracold atomic gas”. In: *Nature* 397.6720 (1999), pp. 594–598.
- [91] M. M. Kash, V. A. Sautenkov, A. S. Zibrov, L. Hollberg, G. R. Welch, M. D. Lukin, Y. Rostovtsev, E. S. Fry, and M. O. Scully. “Ultraslow group velocity and enhanced nonlinear optical effects in a coherently driven hot atomic gas”. In: *Phys. Rev. Lett.* 82 (1999), pp. 5229–5232.

- [92] D. Budker, D. F. Kimball, S. M. Rochester, and V. V. Yashchuk. “Non-linear Magneto-optics and Reduced Group Velocity of Light in Atomic Vapor with Slow Ground State Relaxation”. In: *Phys. Rev. Lett.* 83 (9 1999), pp. 1767–1770.
- [93] I. E. Mazets and B. G. Matisov. “Adiabatic Raman polariton in a Bose condensate”. In: *Journal of Experimental and Theoretical Physics Letters* 64.7 (1996), pp. 515–519.
- [94] A. B. Matsko, Y. V. Rostovtsev, O. Kocharovskaya, A. S. Zibrov, and M. O. Scully. “Nonadiabatic approach to quantum optical information storage”. In: *Phys. Rev. A* 64 (4 2001), p. 043809.
- [95] M. Fleischhauer and M. D. Lukin. “Quantum memory for photons: Dark-state polaritons”. In: *Phys. Rev. A* 65 (2 2002), p. 022314.
- [96] R. H. Dicke. “Coherence in Spontaneous Radiation Processes”. In: *Phys. Rev.* 93 (1 1954), pp. 99–110.
- [97] O. Firstenberg, C. S. Adams, and S. Hofferberth. “Nonlinear quantum optics mediated by Rydberg interactions”. In: *Journal of Physics B: Atomic, Molecular and Optical Physics* 49 (2016), p. 152003.
- [98] Enrico Fermi. “Sopra lo spostamento per pressione delle righe elevate delle serie spettrali”. In: *Nuovo Cimento* 11 (1934), pp. 157–166.
- [99] Enrico Fermi. “Sul moto dei neutroni nelle sostanze idrogenate”. In: *Ric. Scientifica* 7 (1936), pp. 13–52.
- [100] T. F. O’Malley, L. Spruch, and L. Rosenberg. “Modification of Effective-Range Theory in the Presence of a Long-Range (r^{-4}) Potential”. In: *Journal of Mathematical Physics* 2 (July 1961), pp. 491–498.
- [101] Alain Omont. “On the theory of collisions of atoms in Rydberg states with neutral particles”. In: *J. Phys. France* 38 (1977), pp. 1343–1359.
- [102] A. Gaj, A. T. Krupp, J. B. Balewski, R. Loew, S. Hofferberth, and T. Pfau. “From molecular spectra to a density shift in dense Rydberg gases”. In: *Nature Communications* 5 (2014), p. 4546.
- [103] P. S. Julienne, F. H. Mies, E. Tiesinga, and C. J. Williams. “Collisional Stability of Double Bose Condensates”. In: *Phys. Rev. Lett.* 78 (10 1997), pp. 1880–1883.
- [104] J. Balewski, A. Krupp, A. Gaj, D. Peter, H.P. Buchler, R. Low, S. Hofferberth, and T. Pfau. “Coupling a single electron to a Bose-Einstein condensate”. In: *Nature* 502 (2013), pp. 664–667.
- [105] Hannes M. Gorniaczyk. “Single Photon Transistor mediated by electrically tunable Rydberg-Rydberg Interactions”. Dissertation. Stuttgart: Universität Stuttgart, 2016.
- [106] Christoph Tresp. “Rydberg polaritons and Rydberg superatoms - Novel tools for quantum nonlinear optics”. Dissertation. Stuttgart: Universität Stuttgart, 2017.

- [107] Johannes Schmidt. “Generation of non-classical light using ultra-cold Rydberg ensembles”. Master Thesis. Stuttgart: Universität Stuttgart, 2014.
- [108] H.J. Metcalf and P. Van der Straten. *Laser Cooling and Trapping*. Heidelberg: Springer, 1999.
- [109] C.J. Foot. *Atomic Physics*. Oxford: OUP Oxford, 2004.
- [110] R. Grimm, M. Weidemüller, and Y. B. Ovchinnikov. “Optical Dipole Traps for Neutral Atoms”. In: *Advances in Atomic Molecular and Optical Physics* 42 (2000), pp. 95–170.
- [111] S. J. M. Kuppens, K. L. Corwin, K. W. Miller, T. E. Chupp, and C. E. Wieman. “Loading an optical dipole trap”. In: *Phys. Rev. A* 62 (1 2000), p. 013406.
- [112] M. D. Barrett, J. A. Sauer, and M. S. Chapman. “All-Optical Formation of an Atomic Bose-Einstein Condensate”. In: *Phys. Rev. Lett.* 87 (1 2001), p. 010404.
- [113] S. R. Granade, M. E. Gehm, K. M. O’Hara, and J. E. Thomas. “All-Optical Production of a Degenerate Fermi Gas”. In: *Phys. Rev. Lett.* 88 (12 2002), p. 120405.
- [114] S. K. Dutta, J. R. Guest, D. Feldbaum, A. Walz-Flannigan, and G. Raithel. “Ponderomotive Optical Lattice for Rydberg Atoms”. In: *Phys. Rev. Lett.* 85 (26 2000), pp. 5551–5554.
- [115] M. R. Andrews, M.-O. Mewes, N. J. van Druten, D. S. Durfee, D. M. Kurn, and W. Ketterle. “Direct, Nondestructive Observation of a Bose Condensate”. In: *Science* 273.5271 (1996), pp. 84–87.
- [116] M. R. Andrews, C. G. Townsend, H.-J. Miesner, D. S. Durfee, D. M. Kurn, and W. Ketterle. “Observation of Interference Between Two Bose Condensates”. In: *Science* 275.5300 (1997), pp. 637–641.
- [117] Päivi Törmä and Klaus Sengstock. *Quantum Gas Experiments: Exploring Many-Body States*. Singapore: World Scientific, 2014.
- [118] S. E. Hamann, D. L. Haycock, G. Klose, P. H. Pax, I. H. Deutsch, and P. S. Jessen. “Resolved-Sideband Raman Cooling to the Ground State of an Optical Lattice”. In: *Phys. Rev. Lett.* 80 (19 1998), pp. 4149–4152.
- [119] H. Perrin, A. Kuhn, I. Bouchoule, and C. Salomon. “Sideband cooling of neutral atoms in a far-detuned optical lattice”. In: *EPL (Europhysics Letters)* 42.4 (1998), p. 395.
- [120] Andrew J. Kerman, Cheng Chin, and Steven Chu. “Beyond Optical Molasses: 3D Raman Sideband Cooling of Atomic Cesium to High Phase-Space Density”. In: *Phys. Rev. Lett.* 84 (3 2000), pp. 439–442.
- [121] Christoph Braun. “Implementation of a Raman Sideband Cooling for ^{87}Rb ”. Bachelor Thesis. Stuttgart: Universität Stuttgart, 2015.
- [122] Claude Cohen-Tannoudji and Alfred Kastler. *Optical Pumping*. USA: Elsevier, 1966.

- [123] William Happer. “Optical Pumping”. In: *Rev. Mod. Phys.* 44 (2 1972), pp. 169–249.
- [124] Thomas Dieterle. “Characterization Of A Single Ion Detector In A Rydberg Experiment”. Bachelor Thesis. Stuttgart: Universität Stuttgart, 2015.
- [125] R. W. P. Drever, J. L. Hall, F. V. Kowalski, J. Hough, G. M. Ford, A. J. Munley, and H. Ward. “Laser phase and frequency stabilization using an optical resonator”. In: *Applied Physics B* 31.2 (1983), pp. 97–105.
- [126] U. Schünemann, H. Engler, R. Grimm, M. Weidemüller, and M. Zielonkowski. “Simple scheme for tunable frequency offset locking of two lasers”. In: *Review of Scientific Instruments* 70.1 (1999), pp. 242–243.
- [127] Christoph Tresp. “A Setup for Highly Precise Excitation and Detection of Rydberg Atoms”. Master Thesis. Stuttgart: Universität Stuttgart, 2012.
- [128] Michael Schlagmüller. “A single Rydberg Atom interacting with a Dense and Ultracold Gas”. PhD Thesis. Stuttgart: Universität Stuttgart, 2016.
- [129] Marian Rockenhäuser. “A Setup for Heterodyne Single-Photon Phase Shift Detection”. Bachelor Thesis. Stuttgart: Universität Stuttgart, 2016.
- [130] Thad G. Walker and M. Saffman. “Consequences of Zeeman degeneracy for the van der Waals blockade between Rydberg atoms”. In: *Phys. Rev. A* 77 (3 2008), p. 032723.
- [131] K. V. Kheruntsyan and P. D. Drummond. “Three-dimensional quantum solitons with parametric coupling”. In: *Phys. Rev. A* 58 (3 1998), pp. 2488–2499.
- [132] I. E. Mazets and G. Kurizki. “How different are multiatom quantum solitons from mean-field solitons?” In: *EPL (Europhysics Letters)* 76.2 (2006), p. 196.
- [133] Jean-Luc Blanchet, Fabrice Devaux, Luca Furfaro, and Eric Lantz. “Measurement of Sub-Shot-Noise Correlations of Spatial Fluctuations in the Photon-Counting Regime”. In: *Phys. Rev. Lett.* 101 (23 2008), p. 233604.
- [134] K. B. W. Harpsøe, U. G. Jørgensen, M. I. Andersen, and F. Grundahl. “High frame rate imaging based photometry - Photometric reduction of data from electron-multiplying charge coupled devices (EMCCDs)”. In: *A&A* 542 (2012), A23.
- [135] *Andor iXon Ultra Hardware Guide*. English. Version 1.2. Andor. 94 pp. September 17, 2014.
- [136] *Andor iXon Ultra Software Guide - SOLIS*. English. Andor. 2012. 121 pp. 2012.
- [137] A. G. Basden, C. A. Haniff, and C. D. Mackay. “Photon counting strategies with low-light-level CCDs”. In: *Mon. Not. R. Astron. Soc.* 345 (2003), pp. 985–991.
- [138] E. Lantz, J.-L. Blanchet, L. Furfaro, and F. Devaux. “Multi-imaging and Bayesian estimation for photon counting with EMCCDs”. In: *Mon. Not. R. Astron. Soc.* 386 (2008), pp. 2262–2270.

- [139] A. G. Basden and C. A. Haniff. “Low light level CCDs and visibility parameter estimation”. In: *Mon. Not. R. Astron. Soc.* 347 (2004), pp. 1187–1197.
- [140] Daniel Gruber and Taras Plakhotnik. “Counting of obscure events: A Bayesian approach”. In: *Chemical Physics Letters* 474.4 (2009), pp. 371–374.
- [141] S. M. Tulloch and V. S. Dhillon. “On the use of electron-multiplying CCDs for astronomical spectroscopy”. In: *Monthly Notices of the Royal Astronomical Society* 411.1 (2011), p. 211.
- [142] K. B. W. Harpsøe, M. I. Andersen, and P. Kjægaard. “Bayesian photon counting with electron-multiplying charge coupled devices (EMCCDs)”. In: *A&A* 537 (2012), A50.
- [143] I. Friedler, D. Petrosyan, M. Fleischhauer, and G. Kurizki. “Long-range interactions and entanglement of slow single-photon pulses”. In: *Phys. Rev. A* 72 (2005), p. 043803.
- [144] E. Shahmoon, G. Kurizki, M. Fleischhauer, and D. Petrosyan. “Strongly interacting photons in hollow-core waveguides”. In: *Phys. Rev. A* 83 (2011), p. 033806.
- [145] T. Peyronel, O. Firstenberg, Q. Liang, S. Hofferberth, A.V. Gorshkov, T. Pohl, M.D. Lukin, and V. Vuletić. “Quantum nonlinear optics with single photons enabled by strongly interacting atoms”. In: *Nature* 488 (2012), pp. 57–60.
- [146] Vera Bendkowsky, Björn Butscher, Johannes Nipper, James P. Shaffer, Robert Löw, and Tilman Pfau. “Observation of ultralong-range Rydberg molecules.” In: *Nature* 458.7241 (2009), pp. 1005–1008.
- [147] V. Bendkowsky, B. Butscher, J. Nipper, J. B. Balewski, J. P. Shaffer, R. Löw, T. Pfau, W. Li, J. Stanojevic, T. Pohl, and J. M. Rost. “Rydberg Trimers and Excited Dimers Bound by Internal Quantum Reflection”. In: *Phys. Rev. Lett.* 105.16 (2010), p. 163201.
- [148] Bjoern Butscher, Vera Bendkowsky, Johannes Nipper, Jonathan B. Balewski, Ludmila Kukota, Robert Löw, Tilman Pfau, Weibin Li, Thomas Pohl, and Jan Michael Rost. “Lifetimes of ultralong-range Rydberg molecules in vibrational ground and excited states”. In: *Journal of Physics B: Atomic, Molecular and Optical Physics* 44.18 (2011), p. 184004.
- [149] W. Li, T. Pohl, J. M. Rost, S. T. Rittenhouse, H. R. Sadeghpour, J. Nipper, B. Butscher, J. B. Balewski, V. Bendkowsky, R. Löw, and T. Pfau. “A Homonuclear Molecule with a Permanent Electric Dipole Moment”. In: *Science* 334.6059 (2011), pp. 1110–1114.
- [150] D. Booth, S. T. Rittenhouse, J. Yang, H. R. Sadeghpour, and J. P. Shaffer. “Production of trilobite Rydberg molecule dimers with kilo-Debye permanent electric dipole moments”. In: *Science* 348 (2015), pp. 99–102.

- [151] Thomas Niederprüm, Oliver Thomas, Tanita Eichert, Carsten Lippe, Jesús Pérez-Ríos, Chris H. Greene, and Herwig Ott. “Observation of pendular butterfly Rydberg molecules”. In: *Nature Communications* 7 (2016), p. 12820.
- [152] A. Gaj, A. T. Krupp, P. Ilzhöfer, R. Löw, S. Hofferberth, and T. Pfau. “Hybridization of Rydberg Electron Orbitals by Molecule Formation”. In: *Phys. Rev. Lett.* 115 (2 2015), p. 023001.
- [153] J. Tallant, S. T. Rittenhouse, D. Booth, H. R. Sadeghpour, and J. P. Shaffer. “Observation of Blueshifted Ultralong-Range Cs₂ Rydberg Molecules”. In: *Phys. Rev. Lett.* 109 (17 2012), p. 173202.
- [154] B. J. DeSalvo, J. A. Aman, F. B. Dunning, T. C. Killian, H. R. Sadeghpour, S. Yoshida, and J. Burgdörfer. “Ultra-long-range Rydberg molecules in a divalent atomic system”. In: *Phys. Rev. A* 92 (3 2015), p. 031403.
- [155] D. A. Anderson, S. A. Miller, and G. Raithel. “Angular-momentum couplings in long-range Rb₂ Rydberg molecules”. In: *Phys. Rev. A* 90 (6 2014), p. 062518.
- [156] A. T. Krupp, A. Gaj, J. B. Balewski, P. Ilzhöfer, S. Hofferberth, R. Löw, T. Pfau, M. Kurz, and P. Schmelcher. “Alignment of *D*-State Rydberg Molecules”. In: *Phys. Rev. Lett.* 112 (14 2014), p. 143008.
- [157] M. A. Bellos, R. Carollo, J. Banerjee, E. E. Eyler, P. L. Gould, and W. C. Stwalley. “Excitation of Weakly Bound Molecules to Trilobitelike Rydberg States”. In: *Phys. Rev. Lett.* 111 (5 2013), p. 053001.
- [158] Heiner Saßmannshausen, Frédéric Merkt, and Johannes Deiglmayr. “Pulsed excitation of Rydberg-atom-pair states in an ultracold Cs gas”. In: *Phys. Rev. A* 92 (3 2015), p. 032505.
- [159] T. Manthey, T. Niederprüm, O. Thomas, and H. Ott. “Dynamically probing ultracold lattice gases via Rydberg molecules”. In: *New Journal of Physics* 17.10 (2015), p. 103024.
- [160] F. Böttcher, A. Gaj, K. M. Westphal, M. Schlagmüller, K. S. Kleinbach, R. Löw, T. Cubel Liebisch, T. Pfau, and S. Hofferberth. “Observation of mixed singlet-triplet Rb₂ Rydberg molecules”. In: *Phys. Rev. A* 93 (3 2016), p. 032512.
- [161] Thomas Niederprüm, Oliver Thomas, Tanita Eichert, and Herwig Ott. “Rydberg Molecule-Induced Remote Spin Flips”. In: *Phys. Rev. Lett.* 117 (12 2016), p. 123002.
- [162] E. Distante, A. Padrón-Brito, M. Cristiani, D. Paredes-Barato, and H. de Riedmatten. “Storage Enhanced Nonlinearities in a Cold Atomic Rydberg Ensemble”. In: *Phys. Rev. Lett.* 117 (2016), p. 113001.
- [163] Heiner Saßmannshausen, Frédéric Merkt, and Johannes Deiglmayr. “Experimental Characterization of Singlet Scattering Channels in Long-Range Rydberg Molecules”. In: *Phys. Rev. Lett.* 114 (13 2015), p. 133201.

- [164] Hannes Busche, Paul Huillery, Simon W. Ball, Teodora Ilieva, Matthew P. A. Jones, and Charles S. Adams. “Contactless nonlinear optics mediated by long-range Rydberg interactions”. In: *Nature Physics* 13 (2017), p. 655.
- [165] B. Butscher, J. Nipper, J. B. Balewski, L. Kukota, V. Bendkowsky, R. Löw, and T. Pfau. “Atom–molecule coherence for ultralong-range Rydberg dimers”. In: *Nature Physics* 6.12 (2010), p. 970.
- [166] Thomas Niederprüm, Oliver Thomas, Torsten Manthey, Tobias M. Weber, and Herwig Ott. “Giant Cross Section for Molecular Ion Formation in Ultracold Rydberg Gases”. In: *Phys. Rev. Lett.* 115 (1 2015), p. 013003.
- [167] Richard Schmidt, H. R. Sadeghpour, and E. Demler. “Mesoscopic Rydberg Impurity in an Atomic Quantum Gas”. In: *Phys. Rev. Lett.* 116 (10 2016), p. 105302.
- [168] Asaf Paris-Mandoki, Hannes Gorniaczyk, Christoph Tresp, Ivan Mirgorodskiy, and Sebastian Hofferberth. “Tailoring Rydberg interactions via Förster resonances: state combinations, hopping and angular dependence”. In: *Journal of Physics B: Atomic, Molecular and Optical Physics* 49.16 (2016), p. 164001.
- [169] Wolfgang Nolting. *Fundamentals of Many-body Physics*. Springer-Verlag Berlin Heidelberg, 2009, p. 602.
- [170] Immanuel Bloch, Jean Dalibard, and Wilhelm Zwerger. “Many-body physics with ultracold gases”. In: *Rev. Mod. Phys.* 80 (3 2008), pp. 885–964.
- [171] I. Carusotto, D. Gerace, H. E. Tureci, S. De Liberato, C. Ciuti, and A. Imamoglu. “Fermionized Photons in an Array of Driven Dissipative Nonlinear Cavities”. In: *Phys. Rev. Lett.* 103 (3 2009), p. 033601.
- [172] Martin Kiffner and Michael J. Hartmann. “Dissipation-induced correlations in one-dimensional bosonic systems”. In: *New Journal of Physics* 13.5 (2011), p. 053027.
- [173] D. P. Sadler, E. M. Bridge, D. Boddy, A. D. Bounds, N. C. Keegan, G. Lochead, M. P. A. Jones, and B. Olmos. “Radiation trapping in a dense cold Rydberg gas”. In: *Phys. Rev. A* 95 (1 2017), p. 013839.
- [174] Mohammad F. Maghrebi, Norman Y. Yao, Mohammad Hafezi, Thomas Pohl, Ofer Firstenberg, and Alexey V. Gorshkov. “Fractional quantum Hall states of Rydberg polaritons”. In: *Phys. Rev. A* 91 (3 2015), p. 033838.
- [175] Alexander W. Glaetzle, Marcello Dalmonte, Rejish Nath, Christian Gross, Immanuel Bloch, and Peter Zoller. “Designing Frustrated Quantum Magnets with Laser-Dressed Rydberg Atoms”. In: *Phys. Rev. Lett.* 114 (17 2015), p. 173002.
- [176] C.R. Murray, I. Mirgorodskiy, C. Tresp, A.V. Gorshkov, S. Hofferberth, and T. Pohl. “Photon subtraction via induced many-body decoherence”. In: *in progress* (2017).

-
- [177] Serge Rosenblum, Orel Bechler, Itay Shomroni, Yulia Lovsky, Gabriel Guendelman, and Barak Dayan. “Extraction of a single photon from an optical pulse”. In: *Nat Photon* 10.1 (2016). Letter, pp. 19–22.
- [178] Claudia Mewes and Michael Fleischhauer. “Decoherence in collective quantum memories for photons”. In: *Phys. Rev. A* 72 (2 2005), p. 022327.
- [179] Jonathan Simon, Haruka Tanji, James K. Thompson, and Vladan Vuletić. “Interfacing Collective Atomic Excitations and Single Photons”. In: *Phys. Rev. Lett.* 98 (18 2007), p. 183601.
- [180] Bo Zhao, Yu-Ao Chen, Xiao-Hui Bao, Thorsten Strassel, Chih-Sung Chuu, Xian-Min Jin, Jorg Schmiedmayer, Zhen-Sheng Yuan, Shuai Chen, and Jian-Wei Pan. “A millisecond quantum memory for scalable quantum networks”. In: *Nature Physics* 5.2 (2009), pp. 95–99.